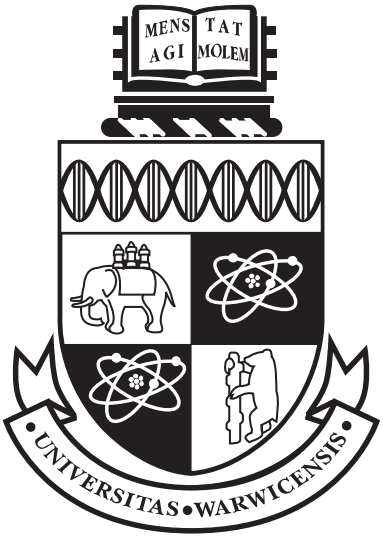

Solid State NMR Studies of Inorganic Pigment Materials and Catalysts

by

Thomas Frank Kemp

Thesis

Submitted to the University of Warwick

for the degree of

Doctor of Philosophy

Physics Department

THE UNIVERSITY OF
WARWICK

Contents

List of Tables

List of Figures

Acknowledgments

I would like to thank my supervisor Prof. M.E.Smith and the rest of the solid state NMR group at the University of Warwick for their support. I would also like to thank the EPSRC and Johnson Matthey for funding my PhD.

Prof. Steve Feller (Coe College, America) and Dr Klaus Eichele (University of Tübingen, Germany) were both very helpful in developing QuadFit.

The Ni-Al Hydroxycarbonates, CuInSSe doped ZnSe, Tin Tungstates, Enamels and Tin Niobates were produced in conjunction with Johnson Matthey in the group of Dr Peter Bishop with particular thanks go to Dr Nicholas Carthey and Dr Steven Bennett. The group of Prof. David Antonelli (University of Windsor, Canada) kindly provided the mesoporous oxides.

Declaration

The work in this thesis was conducted at the University of Warwick Physics department. The work is of my own independant research except where referenced.

Some of the work in Chapters 4 and 7 has been published:-

Boron-10 NMR: what extra information can it give about borate glasses? D.Holland, S.A.Feller, T.F.Kemp, M.E.Smith, D.Winslow, M.Kodama, Physics and Chemistry of Glasses: European Journal of Glasses Science and Technology, 2007, 40B(1),1-8.

A Solid-State ^{17}O NMR study of Local Order and Crystallinity in Amine-Templated Mesoporous Nb Oxide. B.O.Skadtchenko, Y.Rao, T.F.Kemp, P.Bhattacharya, P.A.Thomas and M.E.Smith. Angew. Chem. Int. Ed. 2007, 46, 2635-2638.

It is expected several other papers will be prepared from other work presented in this thesis.

Abstract

The research conducted can be split into three major regions; pigment material, a simulation program called QuadFit and mesoporous oxides. There has also been some extra work conducted on a catalyst for partial hydrogenation of vegetable oils. Various techniques have been used on the different systems including XPS, STEM and ^{77}Se, ^{17}O, ^{93}Nb, ^{15}N, ^{119}Sn, ^{27}Al, ^{115}In and ^{63,65}Cu static and MAS NMR.

The pigment materials consist of a series of materials which are grouped under the F-Colours project. The pigments consist of sulphur doped tin niobates, copper indium sulphur selenide doped zinc selenides, sulphur doped tin tungstates and colloidal gold and silver enamels. The sulphur doped tin niobate study shows a conversion from foordite to pyrochlore and also where the sulphur sits in the structure. The copper indium sulphur selenide doped zinc selenide study shows the indium and copper moving into the zinc selenide as copper indium pairs. However, how the pairs sit in the structure remains undetermined. The sulphur doped tin tungstate study shows that the sulphur acts as a promoter for the beta phase rather than the desired alpha phase. The enamels based on gold and silver show that the tin site does not determine the colour of the enamel and the silver-gold association is likely to be the dominant factor.

Mesoporous oxides show a link between the amount of mesoporous structure and their temperature stability. The nitrogen spectra of the template in the material shows that in the mesoporous silicate (which has the largest surface area) there is a breakdown of the amine into NH groups which does not appear in the other mesoporous materials. This could lead to a method of increasing the surface area of the other mesoporous oxides.

QuadFit has the ability to simulate quadrupolar and CSA interactions with distributions of interactions whilst static and the quadrupolar interaction with distributions under MAS. The program is written in Java so will run on most platforms and also has near perfect stability.

Chapter 1

Introduction

During my PhD I have been funded by Johnson Matthey under the CASE award system with a main emphasis on pigments through the F-Colours project. There have been some other areas of research in conjunction with Johnson Matthey such as the doped Ni-Al hydroxycarbonates which are used in the manufacture of margarine during the partial hydrogenation of the edible oils. In parallel with the Johnson Matthey projects other interests have been studied, such as some mesoporous oxides and the writing of a program for simulatation of NMR spectra known as QuadFit. The mesoporous oxide project has been a collaboration with Prof. D. Antonelli from the University of Windsor. Mesoporous oxides of transition metals are relatively new materials and as such have not been studied using solid state NMR before. A version of QuadFit was written during my MSc. As part of my PhD I felt that the program should be re-written to include cross-platform compatibility, near perfect stability and have new functionality to allow it to become a complete simulation tool for 1D NMR of amorphous inorganic materials.

1.1 Background to Materials Studied

1.1.1 F-Colours

Traditionally many pigments were based on heavy metals (e.g. Pb, Cd, etc.) which have been discovered can be toxic to humans. Over time many alternatives have become available. However, there are currently no really good substitute yellow, orange or red pigments which are as stable or as bright as the cadmium-based traditional pigments. The production of cadmium-based pigments is potentially damaging to the environment and as such they are difficult and expensive to produce in a safe manner. Currently the estimated use of cadmium-based pigments in the EC is 1000 tons per year and in recent years worldwide legislation is making the production of these pigments especially expensive and difficult. The F-Colours project is a confidential DTI project and is aimed at producing and categorising new pigment systems to replace these traditional toxic pigments. The project focuses on using mixed metal oxide chemistry with particular attention on the tin(II)-tin(IV) couple. The systems studied here are tin niobates, copper indium sulphur selenide doped zinc selenides and pink enamels.

Tin Niobates

Tin niobates are a viable possibility to replace the traditional orange and yellow pigments; they show high temperature stability, are easy to produce and are non-toxic. The production technique is also relatively simple and they are produced from materials which are relatively non-toxic. Tin niobates form one of two structures, foordite or pyrochlore, depending on the chemical composition. The original material is yellow in colour. When sulphur is added to the tin niobate structure

the colour shifts to a strong orange.

Much work has been done on mixed lead and tin niobates in the past, refining the structure using XRD. These materials have been studied due to their ferroelectric properties with the aim of removing the lead from the material[11]. One paper has been published by Cruz et al. with ^{119}Sn and ^{93}Nb MAS NMR results from both the foordite and pyrochlore phases of the tin niobates[5]. The paper contains relatively complete sets of results for the foordite and pyrochlore materials including structures for both the materials. Another paper by Cruz et al. was published at the same time with more complete XRD data for the two forms of tin niobate[12]. These papers give a good starting point for the study of sulphur-doped tin niobates for which there are no published data.

Copper Indium Sulphur Selenide doped Zinc Selenides

During the F-Colours project it was discovered that adding sulphur or selenium to a system tends to shift the band gap of the material to longer wave lengths[13]. A system was then chosen which was ideal to study this effect. The system must show the desired effect, have many nuclei which can be studied by NMR and have well known, well defined structures. Zinc selenide is yellow and when doped with copper indium sulphur selenide it turns a bright orange. Selenium, indium and copper can all be studied by current NMR techniques with zinc possible, but difficult. The structures of zinc selenide and copper indium selenide are well known. The structure of copper indium sulphur selenide has not been published.

Enamels

The traditional materials which are manufactured to produce the purples and reds in pigments are difficult to produce with any reproducibility of the colour[14]. Some new materials which rely on colloidal gold and silver with tin oxide are being developed and produce some pinks. These materials are stable and relatively easy to produce, but they do have a relatively limited colour range. Work is being carried out with Johnson Matthey towards understanding how the colour can be varied and controlled to allow a larger range of colours to be produced.

1.1.2 Mesoporous Oxides

Catalysts are used in a lot of industries from power generation through to food manufacture. Small increases in the selectivity and activity of a catalyst can mean huge increases in profit for companies, so any advances are significant. Microporous and mesoporous materials show large surface areas, narrow pore size distribution and highly controllable pore sizes. These properties lend themselves to highly active and selective catalysts. Molecular sieves also rely on having highly controllable pore sizes and narrow size distributions so that the sieve can selectively absorb molecules.

The microporous and mesoporous materials of interest have arrays of pores which tend to have narrow size distributions. Microporous materials have pores in the size range of $\leq$20 Å and mesoporous materials have pores in the size range of 20-500 Å[15]. The large arrays of pores lead to very large surface areas of up 1200 m^2 g^{-1}. Typical microporous materials are crystalline framework solids such as zeolites. The largest dimensions found so far are 10-12 Å for some metal-

lophosphates and approximately 14 Å for the mineral cacoxenite[16]. Many of the mesoporous materials produced up to 1992 were silicas or modified layered materials. These materials, despite showing some mesoporous structure, also tended to be amorphous or polycrystalline. In 1992 a paper reported the calcination of aluminosilicate gels in the presence of surfactants to produce a structure with regular arrays of uniform channels[16]. The sizes of the pores could be tailored from 16 to 100 Å through the choice of surfactants, auxiliary chemicals and reaction conditions. This material known as MCM41 approached 1400 m^2 g^{-1}. Over the next few years attempts were made using the same method to produce transition metal oxides with the same structure but failed to do so. In 1995 a paper by Antonelli reported the first production of a mesoporous transition metal oxide of TiO_2[17]. The material showed no amorphous or layered phases and still showed a narrow pore size distribution when heated in air for 4 hours at 350°C. The surface area was relatively low at 200 m^2 g^{-1} due to surfactant retention with a pore size of 100 nm. TEM showed that even after heating to 500°C in O_2 there was significant pore retention despite some collapse of the structure. Although this was not a perfect material it was a large step in the right direction. In 1996 Antonelli published another paper with improved manufacture techniques of mesoporous oxides which were stable to at least 400°C[18]. Antonelli reported having produced mesoporous Nb,Ti,Zr,Ta,Ce and Y oxides and reported that the mechanism for the structure being produced is the metal nitrogen bond in the precursor remaining intact through the first stages of the manufacture process.

1.1.3 Other Materials Studied

Tin Tungstates

Tin tungstates are relatively unstudied in NMR with the only reference being a conference paper at the Joint 29th AMPERE and 13th ISMAR International Conference titled "^{119}Sn MAS study of semiconducting $SnWO_4$ powders, Magnetic Resonance and Related Phenomena" in August 1998[19]. The study of tin tungstates really started in the 1970s when the alpha and beta forms of $SnWO_4$ were produced and characterised by XRD. The beta tin tungstate was the first form to be produced and characterised, with a paper to that effect being published in 1972 by W.Jeitschko and A.W.Sleight[10]. In 1974 the same pair published another paper[9] reporting the determination of the alpha phase of the tin tungstate using XRD. The two forms are known as the high and the low temperature tin tungstate phases. Alpha tin tungstate is produced if the material is produced below 940K and beta is produced if the tin tungstate is heated to above 940K then quench cooled.

Doped Ni-Al Hydroxycarbonates

Published studies of doped hydroxycarbonates are very rare as they are a commercial catalyst for partial hydrogenation of edible oils. The material is reduced nickel held on an alumina or silica backbone. To stop the nickel reacting with any water in the atmosphere the catalyst is held in a wax.

Hydrogenation of edible oils is used to change the properties of the oil[20]. With varying levels of hydrogenation the melting point can be changed, making handling easier as it is a solid at room temperature and life time of the oil can

be increased. When partial hydrogenation of oils occurs two forms of fatty acid are produced, the cis and the trans. The difference between the cis and trans isomers is the relative position of the substituents about the double bond. The difference in the effect of the health in a human when incorporated in a diet is quite marked. A European study[21] by the EFSA on the effect of trans fatty acids (TFA) on human health reports that there is a link between high TFA levels and increased risk of cardio-vascular disease. Other reports similar to this one have led to the USA introducing legislation forcing levels of TFAs to be stated on the label with less than 5 g per serving needing no declaration. Similar legislation is being adopted throughout the world so the pressure on the companies which produce partially hydrogenised edible oils to reduce their TFA levels is increasing. To reduce the levels of TFAs in the final product a series of different approaches are being used. These can be split into two different types, short and long term. The short term approaches modify the process conditions such as temperature, pressure, catalyst dosage and hydrogen concentration. The long term approaches modify the catalyst itself by changing the support, active metal and by doping the catalyst. The latter approach is what is being studied here. It is hoped that by adding cerium and zirconium doping into the catalyst the levels of TFAs can be changed and the effect of the doping on the catalyst can be studied resulting in a better understanding of how the system works and how to reduce the levels of TFAs.

1.2 Background to Nuclei Studied

1.2.1 ^{77}Se

Selenium is one of the lesser studied nuclei in solid state NMR due to its unfavourable properties. Although selenium is spin $\frac{1}{2}$ and as such does not suffer from broadening due to the quadrupolar interaction, it does however tend to suffer from extremely long relaxation times of 5 minutes or more. With a natural abundance of only 7.58%, which results in an absolute sensitivity of 5.25×10^{-4} (where ^{1}H=1), and the long relaxation times the nucleus is difficult to study. Selenium does have a relatively high gyromagnetic ratio of 5.1253857×10^{7} s^{-1} T^{-1} which makes it easier to study, and has a large shift range which can make it useful when studying materials due to its sensitivity to changes in chemical environment. Most studies have been performed in the liquid state with reported shifts in the range of -230 ppm to 1560 ppm for inorganics and -670 ppm to 1340 ppm for organics[22]. Most solid state studies of selenium in the past have used cross polarisation (CP)[23] to increase the signal and circumvent the long relaxation times[24, 25]. To this end the amount of studies of selenium in inorganic compounds is very limited with around half of them involving CP from phosphorus to selenium [26, 27]. The selenium studies which have not used cross polarisation are relatively old with a study of $TiSe_2$ in 1977[28] and a review article which covered a large range of materials mainly in solution state[29]. The referencing was conduced using ZnSe at -1622ppm[30] relative to $(CH_3)_2Se$.

1.2.2 ^{17}O

Oxygen is the most abundant anion in the Earth (30 wt$\%$)[31], and as such is very important in many materials which are of interest in Earth Sciences. Oxygen plays a central role in many materials, from organic compounds through to catalysts. There were a few early attempts at high resolution MAS NMR of oxygen with the first one published in 1983[32]. Oxygen NMR wasn't particularly successful to start with due to its relatively low gyromagnetic ratio resulting in only broad resonances being observed. Once magnetic fields, MAS technology and more advanced techniques had improved sufficiently oxygen NMR started to become more popular. The only NMR active isotope of oxygen (^{17}O) is 0.037$\%$ naturally abundant, therefore isotopic enrichment has to be conducted to allow the signal to be obtained. Despite the difficulties in obtaining a signal the popularity of solid state oxygen NMR has increased over the years. Oxygen has a large chemical shift range (for example -277 ppm for Ag_2O to 878 ppm for CeO_2[33]) making it sensitive to chemical environment and its quadrupole moment makes it sensitive to electric field gradients[34]. The quadrupole moment of a metal oxygen bond also has a linear approximation to the first order for the ionicity (I) of a bond $C_Q(MHz) = -203I(\%) + 14.78$[34]. The shift ranges of silicon oxygen bonds (30 to 100 ppm[34]) overlaps the region for the aluminium oxygen bonds (30 to 150 ppm[1]). The similarities in the shift ranges and the quadrupole interaction often cause spectral overlaps. The overlaps can be removed using techniques such as multiple quantum and double rotation (as described in section 2.1.11) to remove the broadening. Some of the earlier work published catalogues various simple oxides[33, 35]. The oxygen work has moved into many areas since the late 80s. Some of the more interesting areas which relate to this thesis have been

the study of microporous zeolites[36], organic and inorganic nanocomposites with transition metal oxides[37] and zirconium tungstate[38]. A recent review article by Ashbrook and Smith[34] gives a good introduction into the area of inorganic solid state ^{17}O NMR and a book by Mackenzie and Smith[1] has an extensive review of the shifts and quadrupole parameters of various systems. The referencing was conducted using H_2O at 0ppm[1].

1.2.3 ^{93}Nb

Niobium NMR was largely ignored up until a few years ago with only the occasional paper being released. Over the last few years more papers have been published, most notably a review article on the chemical shift range in niobia systems by Lapina et al.[39], and more specifically for this thesis a paper on the synthesis and characterisation of tin niobates which uses ^{93}Nb NMR[5]. Niobium has a large shift range (-600 ppm to -2000 ppm[39]) and together with the large quadrupole moment (-320 mb[40]) results in a nucleus which is very sensitive to its chemical environment. The large niobium shift range results in large regions for various niobium oxygen co-ordinations. For four-coordinated Nb the shift range is -650 to -950 ppm, five-coordinated Nb -900 to -980 ppm, six-coordinated Nb -900 to -1360 ppm, seven-coordinated Nb -1200 to -1600 ppm and eight-coordinated Nb shift more negative than -1400 ppm[39]. Although the regions are not distinct, with a little care they can be used to assign peaks in a spectrum. The quadrupole coupling constant of sites can also be used to give information about the electric field gradient with C_Q values ranging from hundreds of kHz to hundreds of MHz depending on the symmetry of the site[39].

Niobium only has one naturally occurring isotope which is ^{93}Nb. This has a spin of $\frac{9}{2}$ and a gyromagnetic ratio of 6.5674x10^{7} rad T^{-1} s^{-1}. The high gyromagnetic ratio, and 100$\%$ natural abundance lead to a very sensitive nucleus (0.48 of ^{1}H). Although the high spin helps to counteract the large quadrupole moment it makes acquiring spectra challenging, as currently available spinning speeds are often not sufficient to narrow the ^{93}Nb lines completely. To remove the second-order quadrupolar broadening which can make obtaining spectra difficult, various techniques can be used such as MQMAS[41, 42]. Often the information in the wide line is desired so static spectra are acquired. Due to the bandwidth limitations of the probe it is often necessary to take multiple slices of a line shape to get the whole spectrum. Pulse excitation profiles also have to be considered to get a true representation of the line shape. Another common problem of niobium is referencing the spectra. The primary reference is $NbCl_5$ dissolved in dry acetonitrile. Dry acetonitrile is extremely hygroscopic and the shift of the ^{93}Nb line changes depending on the level of water in the system. A relatively stable version of this can be produced using aqueous acetonitrile. The shift of the alternative reference is not particularly accurate and can change significantly over extended periods of time, but is much more stable over short periods of time. The materials have been referenced using a combination of $NbCl_5$ in dry acetonitrile sealed in an ampoule and $NbCl_5$ in wet acetonitrile checked against the dry version and the shift corrected. Due to niobium's high spin it is an ideal candidate for multiple population transfers producing up to a theoretical 9 times gain in signal[3]. Techniques which increase the signal of the nucleus allow niobium to be probed at very low levels so even Nb doped systems become viable .

1.2.4 ^{14,15}N

Nitrogen has two naturally occurring isotopes which are ^{14}N and ^{15}N. They are both NMR-active, with ^{14}N 99.63% naturally abundant and ^{15}N only 0.37%. The substantial difference between the natural abundances would suggest that ^{14}N would be the preferred nucleus, however ^{14}N is spin-1 which results in very wide lines due to there not being a dominant central transition (see section 2.1.7 for a full explanation). This reduces the resolution of the spectra despite the moderate quadrupole moment of 160 mb. ^{15}N on the other hand is a spin-$\frac{1}{2}$ nucleus with a higher gyromagnetic ratio (-2.71261804x10^7 rad T^{-1} s^{-1} as opposed to 1.9337792x10^7 rad T^{-1} s^{-1} for ^{14}N) and is relatively cheap to enrich. Despite a shift range of approximately 600 ppm[1], nitrogen does not have a shift range to allow resolution for the large line widths of ^{14}N, so ^{15}N tends to be the preferred nucleus. Due to the sensitivity and large T_1s (up to 3000 s for Si_3N_4[1]) of nitrogen, cross-polarisation is often used from hydrogen and due to the dipolar coupling between nitrogen and hydrogen, decoupling often has to be used to narrow the signal. The major problem with cross-polarisation is that it selectively enhances the nitrogen depending on their proximity to hydrogen. This can lead to a incorrect picture of the levels of nitrogen in a system. However cross-polarisation is often the only way to acquire a signal in time periods less than a few days. In the area of interest there have been a lot of publications of ^{15}N NMR of amines in various materials, one of which is a 2004 paper by Clawson et al.[43]. The referencing was conducted using ^{15}N enriched Glycene at -347.4ppm relative to neat CH_3NO_2[44].

1.2.5 ^{115,117,119}Sn

Tin is a relatively little used nucleus in solid state NMR due to its low sensitivity and line widths which are dominated by chemical shift anisotropy and dispersion. The nucleus is fairly commonly studied in solution-state organics where the motional averaging removes chemical shift anisotropy. Tin has three NMR-active nuclei ^{115}Sn, ^{117}Sn and ^{119}Sn. ^{117}Sn and ^{119}Sn have similar properties with both being spin-$\frac{1}{2}$ nuclei, ^{117}Sn having a natural abundance of 7.61% and ^{119}Sn a natural abundance of 8.58%. ^{115}Sn on the other hand has a much lower natural abundance of 0.34% which makes it much less viable compared with the other isotopes. ^{119}Sn also has a slightly higher gyromagnetic ratio than ^{117}Sn with -10.0317x10^7 rad T^{-1} s^{-1} as opposed to -9.58879x10^7 rad T^{-1} s^{-1}. This leads to ^{119}Sn being the preferred isotope to use. The similar gyromagnetic ratios of ^{117}Sn and ^{119}Sn often lead to tin-tin J-Coupling being observed in spectra[1]. Tin has a relatively large chemical shift range (-850 to 100 ppm[1]). This leads to a nucleus which is relatively sensitive to chemical environment. As ^{119}Sn is a spin-$\frac{1}{2}$ nucleus it is lacking one of the major relaxation mechanisms (quadrupolar interaction) and as such does not have short relaxation times, although they are usually less than 1 minute. During the late 80s and early 90s a lot of background information was obtained with the shifts and interaction parameters of many tin, oxygen, metal tertiary systems [45, 1] and tin oxides [46]. It was not until the late 90s that non-oxide systems were studied using ^{119}Sn solid-state NMR, with sulphides reported in 1996[47, 48] and the Foordite and Pyrochlore phases of tin niobates reported in 2001[5]. The referencing was conducted using tetramethyl tin at 0ppm.

1.2.6 ^{27}Al

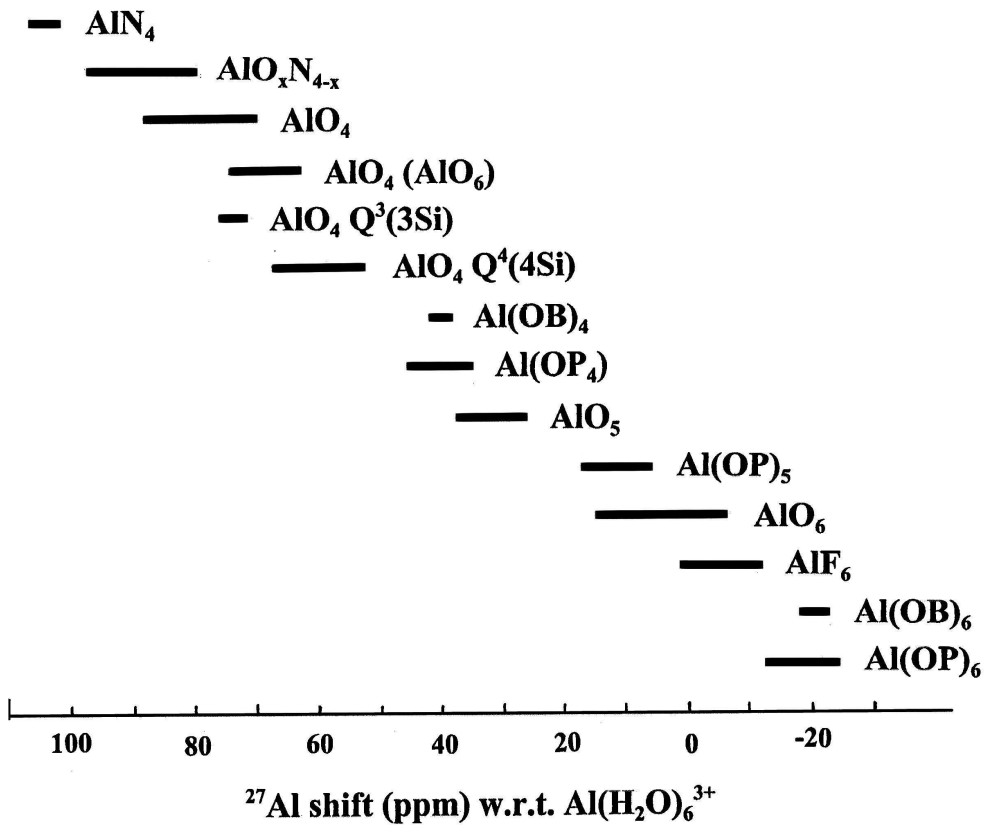

Figure 1.1: ^{27}Al isotropic chemical shift range[1].

Aluminium is one of the most studied quadrupolar nuclei, due to its high relative sensitivity and moderate quadrupole moment. Aluminium is often found in ceramics and other naturally occurring inorganic compounds as aluminium is one of the most abundant elements in the Earth's crust. Aluminium has one NMR active isotope (^{27}Al) which is 100% naturally abundant. ^{27}Al has a gyromagnetic ratio of 6.9762715×10^{7} rad s^{-1} T^{-1} which is relatively high, has a spin of $\frac{5}{2}$ and has a quadrupole moment of 146.6 mb. Due to its high natural abundance and relatively high gyromagnetic ratio aluminium has a very high absolute sensitivity of 21% of that of protons. Due to aluminium also being quadrupolar it tends to have

relatively short relaxation times in the range of a few seconds. The short relaxation times and large sensitivity result in a nucleus of which a spectrum can be obtained in a relatively short period of time. The quadrupolar moment of aluminium is not particularly large. However, up to approximately 10 years ago the size of the quadrupole moment and moderate shift range (-30 to 120 ppm[1]) meant that information was difficult to obtain due to overlapping lines. As the magnetic fields have increased the information obtainable from aluminium spectra has been increased as similar sites could be deconvoluted and programs have been developed to allow better extraction of information. Aluminium has been of specific use in glasses, where the shape of the line could be used to determine the level of order in the materials along with how many distinct sites there are. During the past 10 years over 10,000 papers have been published on solid state ^{27}Al MAS NMR in various areas allowing a list of shift ranges for specific sites to be determined as shown in figure 1.1[1]. The referencing was conducted using YAG at 0.7ppm relative to the hydrated aluminium ion $Al(H_2O)_6^{3+}$[1].

1.2.7 ^{113,115}In

Indium is a relatively unstudied nucleus mainly due to its large quadrupole moment which means in anything but the most crystalline and symmetric cases the resulting spectrum is a broad featureless line. One of the earliest examples of solid state MAS NMR of ^{115}In is a paper by Han et al. of group III-V semiconductors[49]. A much more recent paper (2007) by Yung et al. is about indium nitride[50]. From these two examples and other papers published indium solid state NMR is still only useful on relatively simple systems. As fields and spinning rates increase indium NMR on more complex systems is becoming possible. Indium has a large

shift range (-650 to 500 ppm[22]) so it is sensitive to structural changes and due to the large quadrupole moment it is very sensitive to changes in the symmetry of sites. Indium has two NMR active isotopes, ^{113}In and ^{115}In, which are 4.28% and 95.72% abundant respectively. As ^{115}In is 19 times more abundant ^{115}In is the preferred nucleus although ^{113}In NMR is still possible and potentially useful as it has a slightly lower quadrupole moment of 799 mb rather than 810 mb. The gyromagnetic ratio of ^{115}In is relatively high at 21.912525$\times 10^7$rad s^{-1} T^{-1} and it has a spin of $\frac{9}{2}$. The high natural abundance and high gyromagnetic ratio of ^{115}In results in a high absolute sensitivity of 33% of protons. As indium has a very high spin and tends to interact strongly with its environment the relaxation times are often very short in the range of 0.1 seconds. The very high sensitivity and very short relaxation times result in a nucleus which gives a very strong signal quickly. The lines obtained in ^{115}In NMR are often very wide and despite the large signal spectra can be difficult to obtain. The strong signal does mean indium NMR can be conducted when only traces of the element are present. The referencing was conducted using $InCl_3$ at 430ppm, this shift was extrapolated from data from the paper by Fratuello et al.[51] and could be as much as 50ppm out.

1.2.8 ^{63,65}Cu

Copper has two NMR-active nuclei ^{63}Cu and ^{65}Cu. The appropriate choice between the two is relatively difficult to determine. ^{63}Cu has gyromagnetic ratio 7.1117890$\times 10^7$ rad s^{-1} T^{-1} and natural abundance of 69.09% leading to a relative sensitivity of 6.5% of protons. ^{65}Cu has a gyromagnetic ratio of 7.60435$\times 10^7$ rad s^{-1} T^{-1} and a natural abundance of 30.91% leading to a relative sensitivity of 3.5% of protons. From the two relative sensitivities the obvious choice would

be to use ^{63}Cu. However, both nuclei have a spin of $\frac{3}{2}$ and ^{63}Cu has a quadrupole moment of -220 mb and ^{65}Cu of -204 mb. The reduced quadrupole moment from ^{65}Cu results in the lines being narrower. ^{63}Cu tends to be the preferred nucleus of the two. However, if the lines are slightly too wide ^{65}Cu can be used to determine the information. The fact that the element has two NMR-active nuclei which are both viable means that one field can be used to obtain two sets of data if multiple field data is required to determine the interactions. As the nucleus is quadrupolar and the spin is $\frac{3}{2}$ the lines can be relatively wide, resulting in MAS being unable to narrow the lines. Static solid state NMR is often performed instead of MAS. In static spectra CSA is often a major contribution to the line shape resulting in complicated lines which require multiple fields to fit. Although the line shapes are often complicated this results in a lot of information being available from the spectra. Copper is a relatively little studied nucleus. There have been few papers on solid state copper over the years, with papers only starting to appear from the late 80s. One of the early examples of copper NMR is a paper by Hayashi et al. in 1989[52] and more recently a paper on copper chlorides, bromides and iodides using both MAS and static copper NMR by Haarmann in 2007[53]. With such a relatively small number of papers on the subject the chemical shift range is difficult to define. The referencing was conducted using CuCl at 0ppm.

Chapter 2

NMR Backgound

2.1 NMR Background

2.1.1 Interactions

Nuclei with a magnetic moment ($\underline{\mu} = \gamma\hbar\underline{I}$, where γ is the gyromagnetic ratio and $\underline{I}$ is the net nuclear spin vector) will interact with any magnetic field ($\underline{B_0}$) via the Zeeman interaction to produce a splitting of energy levels (E) as shown in figure 2.1.

$$E = -\underline{\mu} \cdot \underline{B_0} = -\gamma\hbar\underline{I} \cdot \underline{B_0} = -\gamma\hbar m B_0 \tag{2.1}$$

The equation which defines the Zeeman splitting is equation 2.1, where m is the component of the spin parallel to the z axis and can take a range of integer values from $-I \leq m \leq I$. It is these energy levels that form the basis of NMR experiments. The energy levels are separated by an energy $\triangle E$, as $\triangle m = 1$,

$$\triangle E = \gamma\hbar B = \hbar\omega \tag{2.2}$$

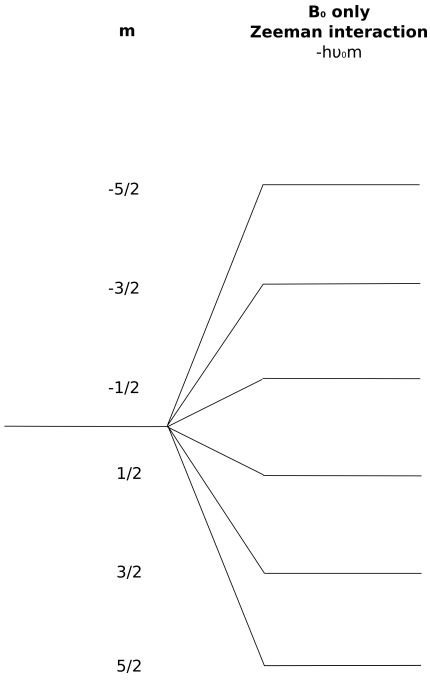

Figure 2.1: Zeeman splitting of a spin $\frac{5}{2}$ nucleus in a magnetic field B_0[1].

where ω is the Larmor frequency in radians per second.

Without any other interactions a particular nucleus would produce a single line at the Larmor frequency[1] resulting in little useful information. There are various interactions which affect the NMR spectra giving rise to both more information and more difficulty in acquiring the information. These interactions include dipolar coupling, J-coupling, chemical and Knight shifts, paramagnetic coupling and quadrupolar interaction. They are all described in detail in reference [1].

2.1.2 Dipolar Coupling

Dipolar coupling is an interaction which occurs through space between two magnetic dipoles, whether the dipoles are the same (homonuclear) or different (heteronuclear). The energy of the interaction is easily obtained using the classical expression for energy between two magnetic dipoles. Using a direct substitution

into the classical dipolar expression for quantum mechanical operators the Hamiltonian is produced. Changing this from Cartesian to polar coordinates gives the so-called "Alphabet" form of the dipolar Hamiltonian.

$$H_D = \frac{\mu_0 \gamma_1 \gamma_2 \hbar^2}{4\pi r^3}(A + B + C + D + E + F) \tag{2.3}$$

Only the A and B terms are independent of time and conserve energy for the homonuclear case, and these two terms are known as the secular part of the Hamiltonian[1]. For the heteronuclear case only the A term remains secular. For both cases both A and B have the same dependence on θ, which is the angle between the internuclear vector and the magnetic field. The properties of the Hamiltonian in both cases are similar. As there is a dependence on θ it means that in a powder sample, where all possible values of θ are present, the interaction gives rise to line broadening. This line shape is distinctive with singularities if isolated pairs of spins exist, but normally a given spin will interact with many other nuclei and the dipolar interaction is only observable as a smooth broadening of the spectrum into a Gaussian-like line[1].

2.1.3 J-coupling

J-coupling is rarely seen in solids due to its relatively weak effects and the broadening due to other interactions. It can be seen in some tin systems where the effect is large. J-coupling is a quantum mechanical indirect interaction, arising from spin-orbital, spin-dipolar and Fermi contact interactions. Two nuclei interact via the electrons between them. The first nucleus perturbs the electrons which in turn produce a magnetic field at the other nucleus. As the interaction relies on intermediate electrons, strong bonding is required as in covalently bonded systems.

The Hamiltonian for this interaction is[1].

$$H_J = h\underline{I}_1 \cdot \underline{\underline{J}}_{12} \cdot \underline{I}_2 \tag{2.4}$$

where $\underline{\underline{J}}_{12}$ is the J-Coupling tensor. Note that there is no B_0 dependency. The number and type of nuclei that are coupled have a significant effect on the spectrum. For two of the same nuclei, the spectrum is split in two with an intensity ratio of 1:1 and a splitting of J_{12}. For three of the same nuclei the spectrum is split in three with an intensity ratio of 1:2:1 with a splitting between each line of J_{12}. The interaction can also occur between different types of nuclei. Heteronuclear J-coupling results in a change of the intensity ratios.

2.1.4 Paramagnetic Coupling

Paramagnetism usually occurs due to unpaired electrons on an ion. The unpaired electrons cause an additional magnetic field at the nucleus. Paramagnetic coupling can be very strong resulting in the signal being broadened to a level where it is not observable. In the range where paramagnetic broadening is observable, but not catastrophic, the information gained can be very informative. The Hamiltonian for this interaction is[1]

$$H_P = \gamma_I \gamma_S h\underline{I} \cdot \underline{\underline{P}} \cdot \underline{S} \tag{2.5}$$

where I is the nuclear spin, S is the electron spin and $\underline{\underline{P}}$ is the coupling tensor. The coupling tensor is dependent on the average component of the electron spin along the magnetic field. This average component can be reduced significantly by thermal flipping. Therefore the shift due to paramagnetic coupling has a $\frac{1}{T}$ dependence. This allows a relatively easy determination of whether paramagnetic coupling is causing a shift by doing variable temperature NMR.

2.1.5 Chemical Shielding

Chemical shielding is the interaction that changed NMR from a simple physical effect to a highly useful spectroscopic technique[1]. It was realised that the exact resonance frequency that was observed for a given nucleus was dependent on the chemical environment it found itself in. The shift of the line is to first-order linear with applied field. Chemical shielding experimentally can be thought of as an isotropic term and an anisotropic term which has an angular dependence. The isotropic term shows the size of the magnetic field due to the electron at the nucleus. The anisotropic term shows the size of the angular dependence of the magnetic field at the nucleus due to the electrons. As the anisotropic term shows the asymmetries of the electron cloud it gives information about the symmetry of the bonding. For a single or double bond system, the stronger the covalent bonds the larger the CSA. The asymmetry of the CSA interaction will also depend on the angle between the bonds. For a multiple bond system the symmetry of the bonds can change the size of the CSA interaction as well as the asymmetry for the same strength of covalent bond. An extreme example of this is for a nucleus in an octahedral coordination where all the bonds are covalent. An octahedral coordination will result in a small CSA interaction despite the bonds themselves being strongly covalent[54].

The field at the nucleus is actually due to two effects, known as the paramagnetic effect and the Temperature Independent Paramagnetic (TIP) effect. The paramagnetic effect is due to the electrons rotating around the applied magnetic field, thus producing a field which opposes the applied field. The TIP effect is due to the applied magnetic field affecting the electron distribution which can be described as mixing excited electron states into the ground state. If any of the

excited states have paramagnetic properties, the overall effect is to support the applied magnetic field[55]. The energy of the interaction is therefore

$$E = -\gamma\hbar\underline{I}\cdot\underline{B_0} = \frac{\mu_0}{2\pi}\gamma h\underline{I}\cdot\left(\underline{M}+\underline{H_0}\right) = \frac{\mu_0}{2\pi}\gamma h\underline{I}\cdot\left(\underline{\underline{1}}-\underline{\underline{\sigma}}-\underline{\underline{\chi}}\right)\cdot\underline{H_0} \qquad (2.6)$$

This expression can be split up into types of effect, chemical shielding and susceptibility effects. $\underline{\underline{1}}-\underline{\underline{\chi}}$ are due to susceptibility effects and are only usually significant in solution state NMR or when the shape of a solid sample (including grains of a powder) is very variable. $\underline{\underline{\sigma}}$, otherwise known as chemical shift, is due to the shape of the electron density. As the chemical shift is affected by the electron density of the environment, the chemical shift is dependent on the nature of the chemical bonding. This chemical shift information has been used to probe the short-range structure of samples identifying local co-ordinations. The chemical shift Hamiltonian can be derived from equation 2.6 and is given by

$$H_{CS} = \gamma_I h I_Z\cdot\sigma_{ZZ}\cdot B_0 \qquad (2.7)$$

σ_{ZZ} is the component of the chemical shift tensor parallel to the applied magnetic field and is obtained by relevant rotations from the PAS of the chemical shielding tensor to the laboratory axis system giving

$$\sigma_{ZZ} = \sigma_{iso} + \zeta\left[\left(3cos^2\theta - 1\right) + \eta\left(sin^2\theta cos2\phi\right)\right] \qquad (2.8)$$

where $\zeta = \sigma_{ZZ} - \sigma_{iso}$ is the anisotropic part, $\eta = \dfrac{\sigma_{11}-\sigma_{22}}{\zeta}$ is the asymmetry parameter, and θ and ϕ are polar angles of the laboratory axis system in the PAS. The subscripts 11, 22 and 33 denote the xx, yy and zz components in the PAS instead of the LAB frame. By definition the xx, yy and zz components are orthogonal and the PAS is chosen such that only the leading diagonal of the tensor is non-zero. The final result gives an interaction which is effectively composed of

two parts, the isotropic shift (σ_{iso}) and the anisotropic shift ($\triangle\sigma$). The isotropic shift of the line given in ppm is $\frac{1}{3}(\sigma_{11}+\sigma_{22}+\sigma_{33})$ and is also defined by

$$\delta_{sample} = \frac{\nu_{sample} - \nu_{reference}}{\nu_{reference}} \times 10^6 \tag{2.9}$$

A standard reference is used so all the spectra can be compared even if the magnetic fields are not the same. This allows for a change in the magnetic field between experiments. The anisotropic part of the interaction gives rise to a range of shifts spreading out the line, leading to a distinctive line shape[1]. The line shape can then be analysed using specialised software to determine the interaction parameters.

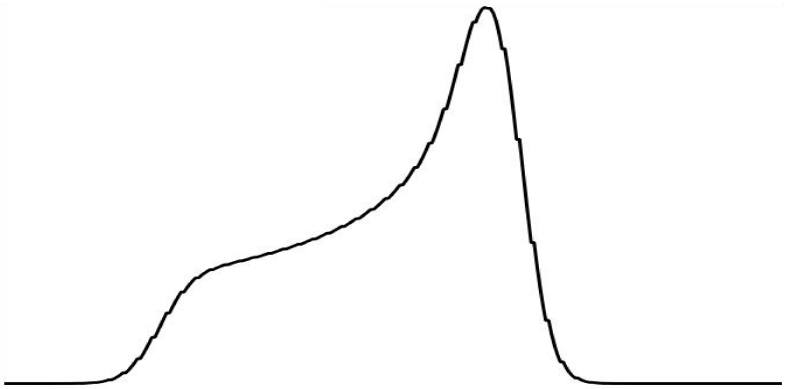

Figure 2.2: CSA line shape with $\sigma_{22} = \sigma_{33}$, therefore $\eta = 1$.

2.1.6 Knight Shift

For a conducting solid there are non-localised conduction electrons. The non-localised electrons still interact with a nucleus, but the nucleus sees a range of electrons as the electrons are non-localised and as such the electrons interact with a range of nuclei. These moving electrons produce a magnetic field at the nucleus.

The conduction electrons occupy a Fermi distribution within the electron states which are filled pairwise due to the Pauli exclusion principle. At zero field each state has an up and a down spin electron so the total magnetic field due to the conduction electrons is zero. However when a magnetic field is applied the energy for each state changes depending on the spin of the electron. This leads to a non-uniformity in the distribution of up and down spin electrons in the electron states which in turn leads to a net magnetisation of the material. The net magnetisation dependency on the applied magnetic field is known as the Pauli susceptibility.

During an experiment the shift of a line is measured which is a sum of the chemical shift and the Knight shift. If the chemical shift can be determined then the Knight shift can also be determined. This is very difficult as both interactions scale with field. The shift in frequency is however given by

$$\triangle\nu = \frac{\gamma B_0}{2\pi}\left(K_{iso} + K_{ax}\left(3cos^2\theta - 1\right)\right) \tag{2.10}$$

where K_{iso} is the isotropic Knight shift, K_{ax} is the anisotropic Knight shift, which is usually axially symmetric, and θ is the angle between the magnetic field and the Z axis of PAS of the Knight shift.

2.1.7 Quadrupolar Interaction

For nuclei with a spin $I > \frac{1}{2}$ the electrical charge distribution is non-spherical giving rise to a quadrupolar moment (eQ) of the nucleus. This interacts with the electric field gradient produced by the electronic environment. The size of the quadrupolar interaction (C_Q) will depend on the product of the eQ with the electric field gradient[1]. The electric field gradient, which is the second derivative of the potential (V), will be a tensor interaction having components $V_{ij} = \frac{\delta^2 V}{\delta i \delta j}$[1]. As

a spatial tensor, in its PAS there should be three components and using Laplace's equation for the electric field gradient tensor as $\bigtriangledown^2 V = 0 \Rightarrow \sum_i V_{ii} = 0$, only two out of the three elements need to be known for all three to be defined. The elements that tend to be chosen to define the tensor are the largest component $V_{ZZ} = eq$ and an asymmetry parameter $\eta = \dfrac{V_{XX} - V_{YY}}{V_{ZZ}}$[1]. Again interactions in NMR tend to be measured in the lab frame so they must first be converted from the PAS. The Hamiltonian is

$$H_Q = \frac{C_Q h}{4I(2I-1)} \left(3\hat{I}_Z^2 - \hat{I}^2\right) + \frac{\eta}{2}\left(\hat{I}_+ + \hat{I}_-\right), \tag{2.11}$$

where $C_Q = \dfrac{e^2 qQ}{h}$ with eQ the quadrupole moment and eq the maximum value of the electric field gradient, and $\hat{I}_+, \hat{I}_-$ are raising and lowering operators respectively[1].

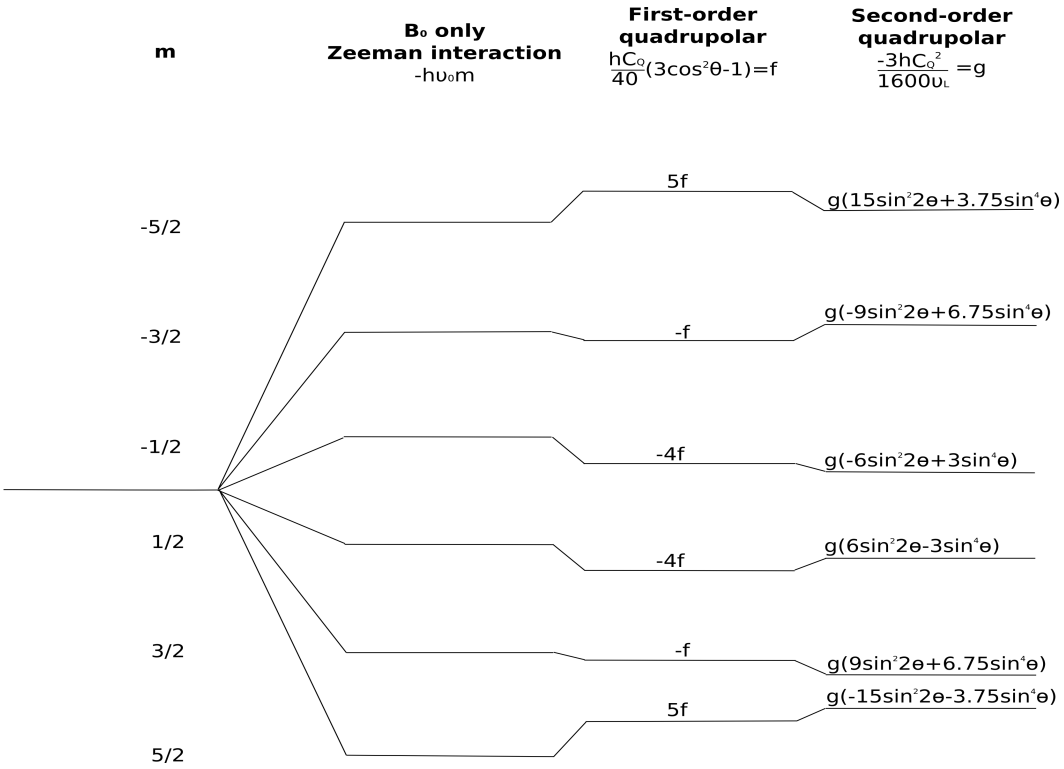

Figure 2.3: Zeeman energy level, first-order and second-order quadrupolar splitting of a $\frac{5}{2}$ spin nucleus[1]

A complication is that an Electric Field Gradient (EFG) is set up by the surrounding charge distribution of the lattice. In response to this EFG the inner electrons of the atom will polarise to reduce their energy state. These polarised inner electrons will cause a secondary EFG at the nucleus counteracting the main EFG. These will give an additional EFG at the nucleus itself if $eq_n = eq(1 - \gamma_\infty)$ where the γ_∞ is the Sternheimer antishielding factor[1].

To obtain a Hamiltonian for individual spins in the lab frame again the Hamiltonian must be obtained from the PAS and converted to the lab frame. In the manipulation, all the terms which do not commute with I_Z need to be removed since these do not affect the spectrum to first-order[1]. This is only really valid in the high field regime ($\nu_{zeeman} \gg \nu_Q$), but as the experiments in this project are all carried out in high fields, in the systems studied here C_Q is never large compared to the Larmor frequency, therefore this is a valid assumption.

The quadrupolar frequency (ν_Q) is the frequency in the NMR spectrum characteristic of the quadrupolar interaction and is defined as

$$\nu_Q = \frac{3C_Q}{[2I(2I-1)]} \tag{2.12}$$

1^{st}- and 2^{nd}-order terms act as perturbations of the Zeeman energy states[1]. The perturbations lead to a splitting of the Zeeman energy states $E_{m,m-1} = E_m - E_{m-1}$ as shown in figure 2.3.

The splittings under MAS are given to first-order by

$$E^{(1)} = \frac{3eQ}{4I(2I-1)}\sqrt{\frac{3}{2}}(1-2m)V_0 \tag{2.13}$$

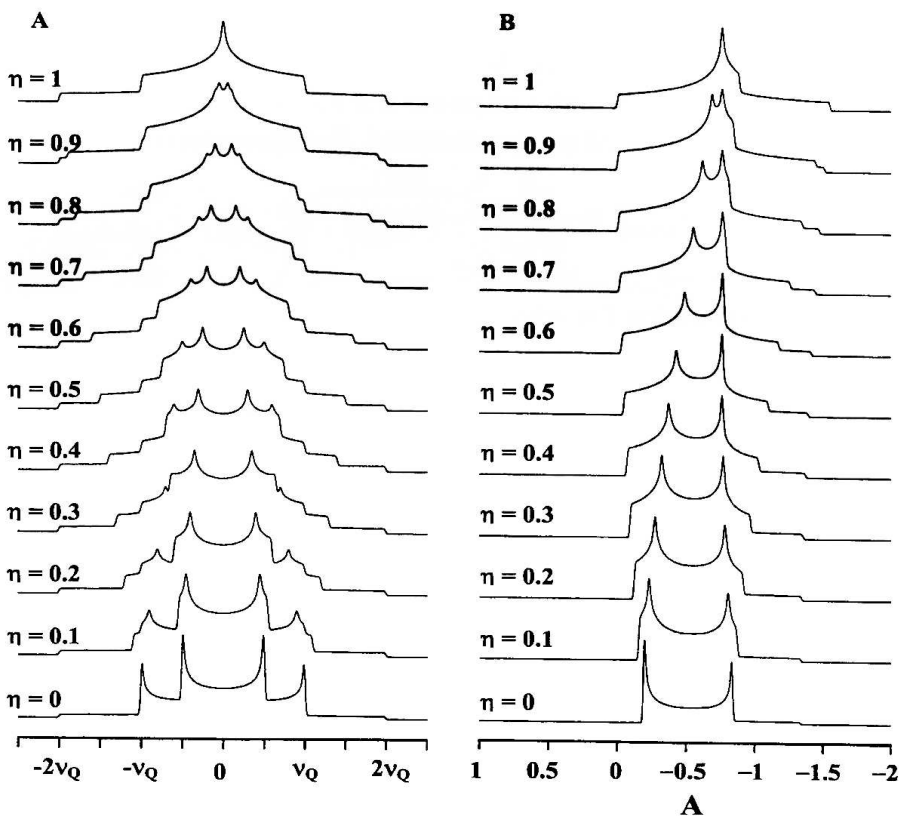

Figure 2.4: Quadrupolar powder patterns for an $I = \frac{3}{2}$ nucleus A:- The outer satellite transitions to first-order, B:- second-order quadrupolar broadening of the central transition, $A = (I(I+1) - 0.75)\nu_Q^2/\nu_0$.

and second-order by

$$E^{(2)} = \frac{-2}{V_0}\left(\frac{eQ}{4I(2I-1)}\right)\Big[V_{-1}V_1(24m(m-1) - 4I(I+1) + 9) + \frac{V_{-2}V_2}{2}(12m(m-1) - 4I(I+1) + 6)\Big] \quad (2.14)$$

where V_i is an element of the second rank tensor of the EFG in the PAS so must be transformed into the lab frame by rotation using the Euler angles α, β, γ. The Euler angles describe the orientation of the magnetic field with respect to the PAS of the EFG tensor. With this transformation and a conversion into polar

coordinates the first-order energy equation becomes

$$E^{(1)} = \frac{C_Q}{8I(2I-1)}(3cos^2\beta - 1 + \eta sin^2\beta cos2\gamma)(3m^2 - I(I+1)) \qquad (2.15)$$

This corresponds to a frequency

$$\nu_m^{(1)} = \frac{3C_Q}{4I(2I-1)}(3cos^2\beta - 1)\left(m - \frac{1}{2}\right) \qquad (2.16)$$

Note that for $m = \frac{1}{2}$ there are no first-order quadrupolar effects on the transition, as the first order effects on the energy levels are the same for $m = \pm\frac{1}{2}$. As there are no first-order effects and the quadrupolar interaction can be large the second-order effects need to be considered, which in the LAB frame gives

$$\begin{aligned} \nu^{(2)}_{\frac{1}{2},-\frac{1}{2}} &= -\frac{1}{6\nu_0}\left(\frac{3\chi_Q}{2I(2I-1)}\right)^2\left(I(I+1) - \frac{3}{4}\right) \times \\ &\quad \left[A(\alpha,\eta)cos^4\beta + B(\alpha,\eta)cos^2\beta + C(\alpha,\eta)\right] \\ &\quad A(\alpha,\eta) = -\frac{27}{8} + \frac{9}{4}\eta cos2\alpha - \frac{3}{8}\eta^2 cos^2 2\alpha \\ &\quad B(\alpha,\eta) = -\frac{30}{8} - \frac{\eta^2}{2} - 2\eta cos2\alpha - \frac{3}{4}\eta^2 cos^2 2\alpha \\ &\quad C(\alpha,\eta) = -\frac{3}{8} + \frac{\eta^2}{3} - \frac{1}{4}\eta cos2\alpha - \frac{3}{8}\eta^2 cos^2 2\alpha \end{aligned} \qquad (2.17)$$

These equations allow the effects on the NMR line shape to be simulated as shown in figure 2.4[56].

2.1.8 Correction of Integrated Intensities of Quadrupolar Interactions

With quadrupolar nuclei the total line intensity is split between the centre band and the spinning side bands. The proportion of the signal in the central band is a function of the quadrupolar interaction parameter, the applied magnetic field

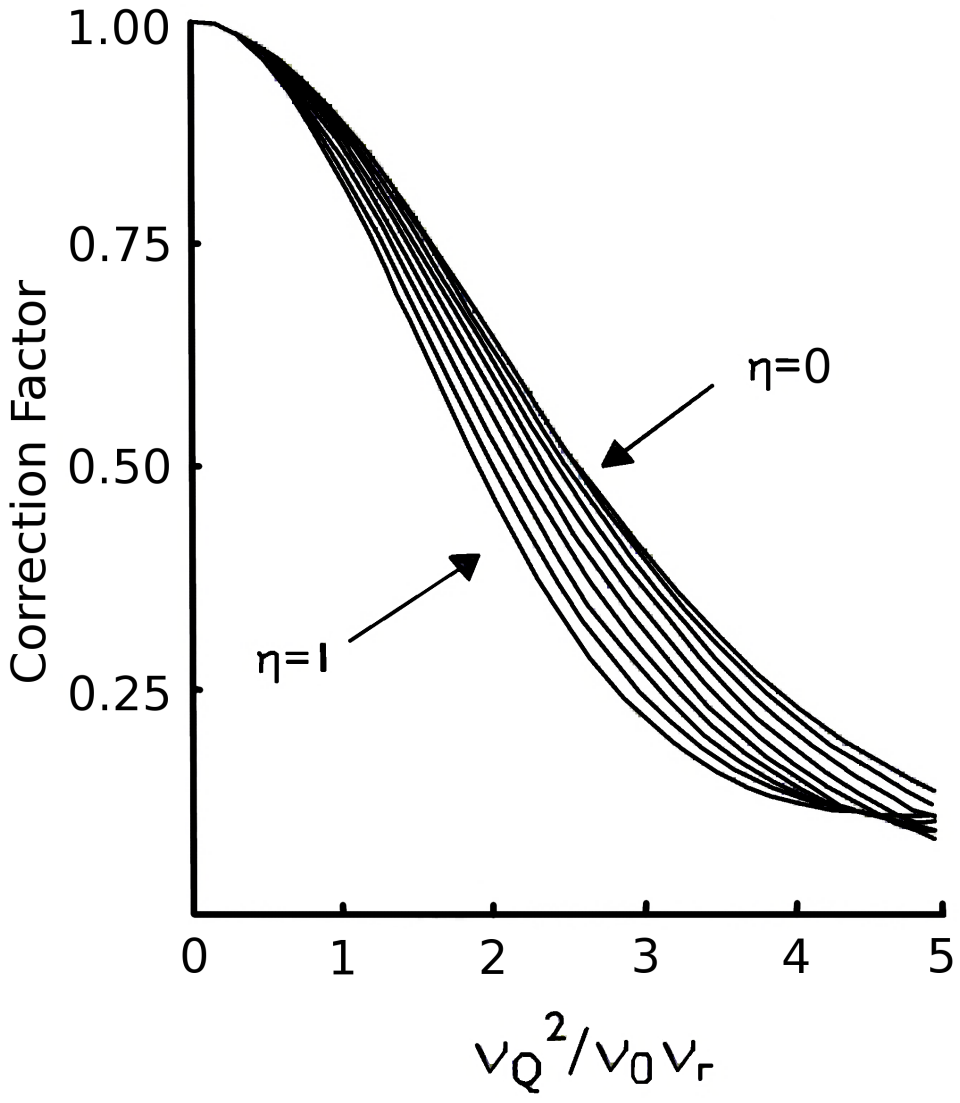

Figure 2.5: The dependence of the intensity of the centre band of an MAS spectra for the central transition as a function of spinning speed (ν_r), Larmor frequency (ν_0) and quadrupole frequency (ν_Q)[2]

and the spinning frequency[1]. If the nucleus being measured has more than one site with different quadrupolar interaction parameters the ratio of the integrated centre bands is not the true ratio of the quantity of sites. To correct this, either the intensity of the spinning side bands must be included, or the intensity of the central band must be corrected. The intensity for the central band depends on

$\frac{\nu_Q^2}{\nu_0\nu_r}$[2], where ν_0 is the Larmor frequency of the nucleus, ν_r is the rate at which the sample is spinning and ν_Q is the quadrupolar frequency. The form of this function has been computed and plotted for easy calculation of the correction factor (graph shown in figure 2.5). Once $\frac{\nu_Q^2}{\nu_0\nu_r}$ has been calculated it is a relatively simple matter to read up to the correct line and across to the correction factor[1].

2.1.9 Magic Angle Spinning

The anisotropic interactions described in section 2.1.7 give rise to broad lines due to powder averaging. For samples where there are multiple sites the different signals can often overlap due to this anisotropic broadening. To simplify the spectra, removal of the anisotropic interaction would be helpful and thus magic angle spinning (MAS) is applied[42]. In MAS the powder sample is loaded into a rotor and spun at up to 60kHz at a fixed angle with respect to the magnetic field.

In an MAS experiment the Hamiltonian must now be transferred from the previous PAS to the lab frame via the rotor axis system (RAS). As the RAS varies with time with respect to the lab frame, the Hamiltonian in the lab frame will be time-dependent. The Hamiltonian can then be split so it has a time-dependent and a time-independent part. For first-order effects $(\propto 3cos^2\theta - 1)$[1], which include dipolar, chemical shielding and first-order quadrupolar, the transformations from the PAS to the RAS to the lab frame cause the time-independent part of the Hamiltonian to gain an additional factor of $3cos^2\beta - 1$, where β is the angle between the axis of the rotor and the magnetic field. If this angle is set to the angle of $54^0 44' 8.2"$, the so called magic angle, then the broadening from this part of the Hamiltonian is removed[1]. MAS has the secondary effect of producing

spinning side bands through the time-dependent part. These side bands occur at integer multiples of the spinning frequency. The spinning side bands are secondary signals which are usually ignored but can contain useful information. However the spinning speed does have to be fast enough, i.e. greater than the residual width, for narrowing to occur. If the signal is strong enough it is possible to see the modulation in the intensity of the spinning side bands, and they can then be used to work out the quadrupolar interaction[1]. This requires a very strong signal and usually very accurate setting of the magic angle for the quadrupolar interaction, when it is called satellite transition spectroscopy[57]. For observation of quadrupolar nuclei the complications that arise for second-order effects under MAS need to be examined.

2.1.10 Second-Order Quadrupolar Effects under MAS

The same rotations that were applied to the first-order quadrupolar effects can be applied to the second-order quadrupolar interaction giving an energy of

$$\begin{aligned} E^{(2)}_{Q,|m\rangle} - E^{(2)}_{Q,|m-1\rangle} \quad \propto \quad & C_0(I,m)F_0(\eta) + \\ & C_2(I,m)P_2(cos\theta)F_2(\beta,\gamma,\eta) + \\ & C_4(I,m)P_4(cos\theta)F_4(\beta,\gamma,\eta) \end{aligned} \tag{2.18}$$

There are two main parts to this equation, the first term is isotropic so just produces a shift, and the second and third terms are anisotropic thus producing broadening. The terms $P_2(cos\theta) = \frac{1}{2}(3cos^2\theta - 1)$ and $P_4(cos\theta) = \frac{1}{8}(35cos^4\theta - 30cos^2\theta + 3)$ are the second and fourth-order Legendre polynomials and do not have zero points at the same angle[1]. A common solution is to spin at the magic angle which removes

the first-order effects and gives some averaging of the second-order quadrupolar interaction, but second-order broadening is not totally removed.

The isotropic effect can produce a significant shift from the centre of gravity of the line from the isotropic chemical shift. The shift can be significant enough so that errors in assignments of peaks to specific structural co-ordinations can occur. The second-order isotropic quadrupolar shift is given by

$$\nu_{Q.iso}^{(2)}(I,m) = -\frac{3C_Q^2}{40\nu_0 I^2(2I-1)^2}\left[I(I+1) - 9m(m-1) - 3\right]\left(1+\frac{\eta^2}{3}\right) \tag{2.19}$$

Under MAS the residual second-order quadrupolar effects produce a line width which is a function of I and m. This line width leaves a condition which must be met for any narrowing to occur, i.e.

$$\nu_r \geq \triangle\nu_Q^{(2)} = f(I)\frac{C_Q^2(6+\eta)^2}{224\nu_0} \tag{2.20}$$

where $f(I)$ is given in Table 2.1 and ν_r is the rate at which the sample is spinning.

I	$\frac{3}{2}$	$\frac{5}{2}$	$\frac{7}{2}$	$\frac{9}{2}$
f(I)	$\frac{1}{3}$	$\frac{2}{25}$	$\frac{5}{147}$	$\frac{1}{54}$

Table 2.1: f(I) for varying spins

2.1.11 Techniques For Removing Second-Order Quadrupolar Effects

There are several methods to remove second-order quadrupolar effects. The various methods split into two main areas, equipment and pulse sequences. The first and most obvious is just to increase the magnetic field as the quadrupolar interaction has a $\frac{1}{B_0}$ dependence. As the quadrupolar interaction has a $\frac{1}{B_0}$ dependence

and the chemical shift has a B_0 dependence, when doubling the field the line width halves and the separation of lines double, assuming the scale is in Hz. This results in a 4-fold gain in resolution. Other equipment-based techniques rely on the orientation dependence of the second-order term of the interaction on the magnet field. Two techniques which rely on the orientation dependence are Double Angle Rotation (DOR) and Dynamic Angle Spinning (DAS). These are both technically demanding, leading to very few examples of these techniques being used. DAS[58][42] flips the rotor quickly between the magic angle ($3cos^2\theta - 1 = 0$) and the zero point of the P_4 Legendre polynomial ($35cos^4\theta - 30cos^2\theta + 3 = 0$). This results in an averaging out of the 1st- and 2nd-order quadrupolar interaction. This technique is implemented in two different ways, one, using a standard stator which is rotated between the two angles and the other implementation is using a clam shell design of stator where jets of air are used to moved the rotor. The former method has the disadvantage that every time the stator is moved the rotor hits the side of the stator and wears out the rotor and stator. The latter method is a more elegant approach, however the design, production and use of the stator is especially difficult. This also has the disadvantage that everytime the rotor is moved it bounces off the stator. The equipment technique DOR[58][42] is more successful than DAS, relying on spinning the sample at both angles at the same time. It is however more difficult to develop in the first place, but does not wear out the equipment quickly. The technique works by spinning two rotors, one inside the other. The outer rotor spins at the magic angle to the magnetic field and the inner rotor spins at the zero point of the P_4 Legendre polynomial to the inner rotor. This results in the quadrupolar interaction being averaged out and leads to very narrow lines.

Using multiple quantum (MQ)[42] techniques the anisotropic quadrupolar term can be refocused so that only the isotropic term of the quadrupolar interaction affects the spectra. This is possible due to the isotropic and anisotropic terms having different rates of evolution depending on the excited transition[59]. The final spectrum contains both the isotropic and anisotropic information. These techniques have made solid state NMR of quadrupolar nuclei much more widely used. However these techniques are not quantitative as they rely on the excitation of the multiple quantum states which is very dependent on the environment of the nuclei and hence may depend on the quadrupolar interaction. The quantification of the MQ experiments can be improved by modifying the pulse sequence and compensating for quadrupolar coupling parameters. Although the corrections result in the technique being more quantifiable it is still not completely reliable.

2.1.12 Signal Amplification Techniques

RAPT

The Rotor Assisted Population Transfer (RAPT)[3] pulse sequence is designed to increase the size of the signal acquired during an experiment by adjusting the population differences between the different energy levels. According to the Boltzmann-distribution, the relative population of the spin states m_I for a spin I nucleus in the high temperature limit is given by[60]

$$p_{m_I} \approx 1 + 2m_I \left(\frac{h\nu_L}{2kT} \right) \tag{2.21}$$

where h is Planck's constant, k is the Boltzmann constant and T is the absolute temperature. For a spin system where only certain energy levels can be occupied

the Boltzmann-distribution can be modified to[60],

$$p_{m_I} \approx 1 + 2m_I\delta \tag{2.22}$$

where $\delta = \left(\frac{h\nu_L}{2kT}\right)$ and the probabilities of different energy levels being populated are shown in figure 2.6. To adjust the population of the nuclear spin energy levels one of two techniques can be used, either transfer of two population levels or a modification of all population levels at once. If the populations are saturated this has the effect of equalising the probability of all the populations being occupied.[60] For a spin $\frac{5}{2}$ nucleus this results in a 3 fold gain in signal as shown in figure 2.6.

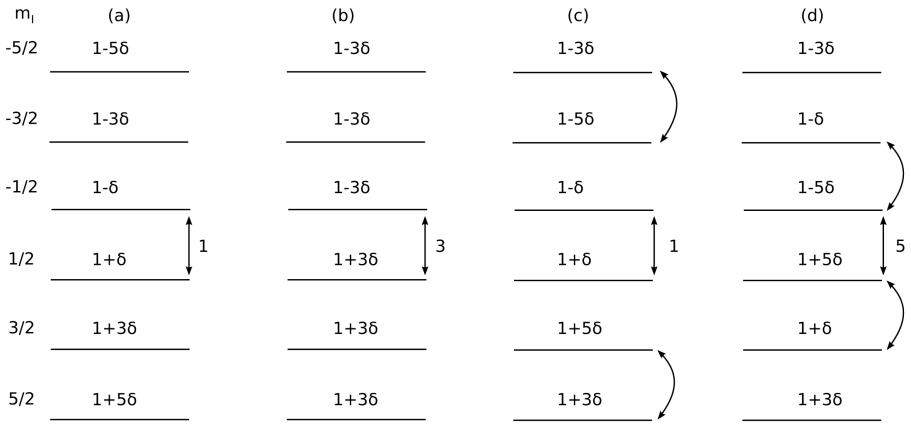

Figure 2.6: Representation of energy levels associated with population distributions for an I=$\frac{5}{2}$ nucleus. (a) at thermal equilibrium, (b) saturation of spin states (c) transfer of the $\pm\frac{5}{2}$ to $\pm\frac{3}{2}$ populations (d) transfer of the $\pm\frac{1}{2}$ to $\pm\frac{3}{2}$ populations. The numbers next to the arrows show the relative gain in signal.[3]

Population saturation can be achieved by applying a series of rapid short pulses with alternating phase before the acquisition pulses as shown in figure 2.7. This is known as Rotor Assisted Population Transfer (RAPT)[3]. The sequence is known as Rotor Assisted as the length of each individual sequence $(2 \cdot d_1 + 2 \cdot d_2)$ should be equal to an integer number of rotor periods (usually one)[3]. The amount of cycles (N) should be large enough to ensure saturation. Extended numbers of

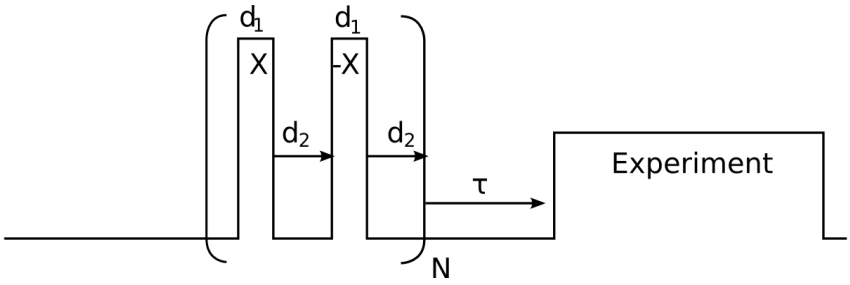

Figure 2.7: The RAPT pulse sequence.

cycles do not gain or lose anything apart from increasing the duty cycle of the probe. The delay between the end of the RAPT sequence and the experiment needs to be short on the scale of spin-lattice relaxation (T_1), otherwise saturation will be lost. The RAPT sequence produces sidebands of the carrier frequency at a frequency of

$$\nu_\phi - \nu_C = \frac{-(\triangle\phi/360^\circ)}{d_1 + d_2}, \tag{2.23}$$

where ϕ is the phase increment between the pulses. It has been found by Yao et al.[61] that the optimum value for $\nu_\phi - \nu_C$ is approximately $\frac{C_Q}{4}$ of the site being observed. The sidebands are used to saturate the satellite transition increasing the population difference between the $-\frac{1}{2}$ and $\frac{1}{2}$ transitions thus increasing the signal[60].

As a modification on this technique other pulse sequences can be used which swap populations. If done correctly they can lead to a gain of $2I$ in signal. These techniques are relatively difficult to implement and use.

Chapter 3

Experimental Details

3.1 Production of Materials

3.1.1 Tin Niobates

Appropriate amounts of tin(II) oxide, tin(IV) oxide, tin metal, sulphur and selenium sulphide and Nb_2O_5 were mixed together by hand in a pot, then in a pestle and mortar. The final mix was then placed in a crucible with carbon paper and a layer of copper powder on top as an oxygen scavenger. The sample was then heated in a furnace in an air atmosphere with a ramp time of 10 minutes up to the firing temperature, held for 30 minutes, then cooled down using a ramp time of 10 minutes. The sample was then split into two. One of the samples was then milled in de-ionised water with 10 mm silicon nitride beads for 10 minutes. The sample was again split into two and one was dried using a centrifuge and an oven. The manufacture process produced tin sulphides as well as the sulphur- or selenium-doped tin niobate. To remove the tin sulphides the sample known as "treated", was then washed using approximately 50% HCl and 50% water at

80°C for 1 hour. The mixture was then allowed to settle and the clear liquid was poured off. A new solution of 50% HCl and 50% water was added and stirred for 1 hour at 80°C. Once allowed to settle the clear liquid was poured off again and a 100% water solution was added, stirred for a short period and a centrifuge was then used to separate the water and precipitate. The precipitate was then dried in an oven overnight at approximately 80°C. The samples which were made using selenium sulphide were washed in an ammonium polysulphide solution instead of HCl, as HCl did not wash off the tin selenides produced during the manufacture. The samples produced are shown in Table 3.1.

Sample Name	**Nominal Composition**	**Firing Temp. °C**	**Processing**
Foordite	$SnNb_2O_6$		
Pyrochlore	$Sn_2Nb_2O_7$		
F600	$Sn_2Nb_2O_{6.3}S_{0.7}$	600	Fired
F700	$Sn_2Nb_2O_{6.3}S_{0.7}$	700	Fired
F800	$Sn_2Nb_2O_{6.3}S_{0.7}$	800	Fired
F900	$Sn_2Nb_2O_{6.3}S_{0.7}$	900	Fired
M600	$Sn_2Nb_2O_{6.3}S_{0.7}$	600	Ball Milled
M700	$Sn_2Nb_2O_{6.3}S_{0.7}$	700	Ball Milled
M800	$Sn_2Nb_2O_{6.3}S_{0.7}$	800	Ball Milled
M900	$Sn_2Nb_2O_{6.3}S_{0.7}$	900	Ball Milled
T600	$Sn_2Nb_2O_{6.3}S_{0.7}$	600	Treated in HCl
T700	$Sn_2Nb_2O_{6.3}S_{0.7}$	700	Treated in HCl
T800	$Sn_2Nb_2O_{6.3}S_{0.7}$	800	Treated in HCl
T900	$Sn_2Nb_2O_{6.3}S_{0.7}$	900	Treated in HCl
F900Se	$Sn_2Nb_2O_{6.3}S_{0.47}Se_{0.23}$	900	Fired
M900Se	$Sn_2Nb_2O_{6.3}S_{0.47}Se_{0.23}$	900	Milled
HCl900Se	$Sn_2Nb_2O_{6.3}S_{0.47}Se_{0.23}$	900	Treated in HCl
Amm900Se	$Sn_2Nb_2O_{6.3}S_{0.47}Se_{0.23}$	900	Treated in Ammonia Polysulphide

Table 3.1: Tin Niobate Samples

3.1.2 Tin Tungstates

The tin tungstates were produced by Johnson Matthey at their Sonning Common Technology Centre. Equal molar quantities of SnO and WO_3 were mixed together using a pestle and mortar. The mixture was then placed in a cylindrical alumina crucible with a layer of copper on top to prevent oxidation of the tin(II). The remaining volume in the crucible was then filled with TiO_2 powder and a lid was put on the crucible. The crucible was then fired for 10 hours at 700°C to gain the alpha tin tungstate or at 1000°C to gain the beta tin tungstate. To produce the sulphur doped samples SnS was used in the production and fired at 700°C.

Sample Name	**Nominal Composition**	**Other Information**
Alpha Tin Tungstate	$SnWO_4$	
Beta Tin Tungstate	$SnWO_4$	
C887-28	$SnWO_{3.65}S_{0.35}$	
C887-29	$SnWO_{3.3}S_{0.7}$	
C887-32B	$SnWO_{3.65}S_{0.35}$	Acid Washed

Table 3.2: Tin Tungstate Samples

3.1.3 CuInSSe doped ZnSe

The CuInSSe doped ZnSe samples were produced by Johnson Matthey at their Sonning Common Technology Centre. Appropriate amounts of copper sulphide, indium sulphide and indium selenide were mixed together using a pestle and mortar. The mixture was then calcined in an evacuated quartz ampoule at 800°C for 10 hours, using heating and cooling rates of 5° per minute. The $CuInS_xSe_{2-x}$ (x=1 or 2) was then mixed with relevant quantities of zinc selenide and placed in an evacuated quartz ampoule. The mixture was then calcined at 850°C for 5 hours using heating and cooling rates of 10°C per minute. The fast fired method was

conducted by placing the mixed material in a crucible, sealing with a carbon disc then covering with TiO_2 to act as an oxygen scavenger. The sample was then heated in air to 850°C at 42.5°C per minute, held at temperature for 30 minutes then cooled at 95°C per minute.

Samples Name	**Nominal Composition**	**Firing Conditions**
$CuInSe_2$	$CuInSe_2$	
CuInSSe	CuInSSe	
ZnSe	ZnSe	
$2\%CuInSe_2$	$CuInSe_2(ZnSe)_{49}$	Normal
$2\%CuInSe_2FF$	$CuInSe_2(ZnSe)_{49}$	Fast Fired
2%CuInSSeFF	$CuInSSe(ZnSe)_{49}$	Fast Fired
$5\%CuInSe_2$	$CuInSe_2(ZnSe)_{19}$	Normal

Table 3.3: CuInSSe doped ZnSe Samples

3.1.4 Doped Al-Ni Hydroxycarbonates

Johnson Matthey produced these catalysts via a co-precipitation route. Typically a solution of nickel nitrate was dissolved in 200 ml water and the solution consisting of sodium carbonate and sodium aluminate also in 200 ml water was slowly added to 300 ml boiling water. This results in a green material precipitating out, known as "Green Cake". This is then reduced in hydrogen at 430°C and encapsulated in saturated fat to give the finished catalyst. For the cerium and zirconium-doped systems the respective nitrates were added to the nickel nitrate solution and the rest of the preparation was carried out in the same way. The samples which used a phospholipid modifier were made, then remelted and treated with 30 wt% phospholipid.

Samples Name	%Ni	%Zr/Ce	%Al	Treatment	Dopants
Pricat 9920				Reduced	None
Pricat 9925				Fired	None
Pricat 9925 R600				Reduced at 600°	None
CP325 + P Modifier Fresh	20	-	1	Fresh Catalyst	
CP325 + P Modifier Used	20		1	Used Catalyst	
Ni-Zr-Al R430	5	1.6	0.5	Reduced at 430°	Zr
Ni-Zr-Al R600	3	1	0.2	Reduced at 600°	Zr
Ni-Zr-Al F430	18	5	1.4	Fired at 430°	Zr
Ni-Zr-Al F600	18	5	1.4	Fired at 600°	Zr
Ni-Ce-Al R430	2	1	0.2	Reduced at 430°	Ce
Ni-Ce-Al R600	3	1.2	0.3	Reduced at 600°	Ce
Ni-Ce-Al F430	11	5	1	Fired at 430°	Ce
Ni-Ce-Al F600	11	5	1	Fired at 600°	Ce

Table 3.4: Samples of Catalyst for Hydrogenation of Edible Oils

3.1.5 Mesoporous Oxides

Yuxiang Rao and David Antonelli from the University of Windsor, Canada produced the mesoporous oxide samples. For the mesoporous niobium oxide a solution of Niobium (V) Ethoxide ($Nb(OE_t)_5$) (5.0 g) in ethanol (10 ml) was treated with tetradecylamine (0.25 - 1 equivalents). This produced a new amino(ethoxy)niobium complex which was then treated with 10-20 ml of water which caused a rapid reaction producing a white gelatinous precipitate. The precipitate was then heated at 100-180°C for seven days to produce the final mesoporous oxide. For the other oxides the original ethoxide was changed for a suitable replacement[18]. For the samples which had the template removed, this was done by treating the sample with 70% nitric acid at pH 1-2 in ethanol for 1-12 hours at room temperature, followed by stirring in ethanol for 12 to 24 hours. All of the samples were treated afterwards using 20% enriched ^{17}O water by heating the sample and water in an inert atmosphere in a sealed vessel at 140°C for 24 hours. All of the samples except the ^{15}N enriched samples had the amine template removed before the ^{17}O

enrichment process. The samples which were heated were heated using a tube furnace for 2 hours whilst N_2 was passed over the sample. The heating was done in a nitrogen atmosphere to try to reduce the loss of ^{17}O during the heating process. The amorphous niobia (Amor Nb) was produced via a sol-gel route to gain an amorphous Nb_2O_5.

Sample Name	Nominal Composition	Other Information
Meso Ta II	Ta_2O_5	Template Removed
Meso Ti	TiO_2	Template Removed
Meso Nb II	Nb_2O_5	Template Removed
Meso Ta II 250	Ta_2O_5	Heated to 250°, Template Removed
Meso Ta II 500	Ta_2O_5	Heated to 500°, Template Removed
Meso Ta II 750	Ta_2O_5	Heated to 750°, Template Removed
Meso Ti 250	TiO_2	Heated to 250°, Template Removed
Meso Ti 500	TiO_2	Heated to 500°, Template Removed
Meso Ti 750	TiO_2	Heated to 750°, Template Removed
Meso Nb II 250	Nb_2O_5	Heated to 250°, Template Removed
Meso Nb II 500	Nb_2O_5	Heated to 500°, Template Removed
Meso Nb II 750	Nb_2O_5	Heated to 750°, Template Removed
Meso Nb 15N	Nb_2O_5+1wt%^{15}N amine	^{15}N Enriched
Meso Ta 15N	Ta_2O_5+1wt%^{15}N amine	^{15}N Enriched
Meso Ti 15N	TiO_2+1wt%^{15}N amine	^{15}N Enriched
Meso Si 15N	SiO_2+1wt%^{15}N amine	^{15}N Enriched
Amor Nb	Nb_2O_5	

Table 3.5: Mesoporous Oxide Samples

3.1.6 Enamels

The enamels were produced by Johnson Matthey by milling gold and silver organometallic precursors with a finely divided glass frit to produce a powder and heated to 400°C. The exact manufacture process is proprietary. The powder is then mixed with an organic medium to form an ink for printing. This isprinted onto coated paper. Once dry the coating can be slid onto the ceramic using waterslide tech-

niques and fired at 700-900°C during which the final colour develops depending on the substrate. The final heating process is done using a ramp up rate of 35°C per minute, a hold time of 5 minutes then a cooling rate of 10°C per minute. The multicomponent glass frit is relatively complicated containing Al_2O_3, B_2O_3, BaO, Bi_2O_3, CaO, CdO, CoO, Fe_2O_3, K_2O, La_2O_3, Li_2O, MgO, Na_2O, P_2O_5, PbO, SiO_2, SrO, TiO_2, V_2O_5, ZnO and ZrO_2.

Sample Name	**%Au**	**%Ag**	**%SnO_2**	**Milled**	**Int. Heating**	**Ink Prep.**	**Firing**
RU3386-I-400	0.3	0.75	12.8	Partial	400°C	No	900°C
RU3386-III-400	0.3	0.75	12.8	Fully	400°C	No	900°C
RU3386-III-340	0.3	0.75	12.8	Fully	340°C	No	900°C
RU3389-710	2.0	0.75	12.8	Fully	400°C	Yes	710°C
RU3389-900	2.0	0.75	12.8	Fully	400°C	Yes	900°C
RU3389-ff	2.0	0.75	12.8	Fully	No	No	No
RU3389-9f	2.0	0.75	12.8	Fully	400°C	No	900°C

Table 3.6: Enamel Samples

3.2 NMR Experiments and Equipment

An NMR experiment requires several pieces of equipment which can be loosely categorised as the magnet, probe and spectrometer. The magnetic field is usually between 2 and 21 Tesla and is generated using a superconducting solenoid held in a liquid helium bath. The solenoid consists of the main coil which produces the main field and a series of other superconducting coils wrapped around the main coil. These coils known as the "cryo-shims" are used to correct the main magnetic field to produce a very stable and homogeneous magnetic field (less than 1 in 10^9) over a small volume at the centre which is known as the "sweet spot". The magnet is constructed so that there is a bore in the centre, which in a wide bore

magnet is 89 mm. Inside the bore sit the room temperature shims and the probe. As the probe contains materials which interact with the magnetic field it reduces the homogeneity of the field. The room temperature shims are a series of coils through which current can be passed to produce small magnetic fields which can be changed to counteract the effects from different probes.

The simplest form of probe is a single channel static probe which contains a coil attached to two capacitors which can be adjusted to change the resonance frequency and impedance of the coil[62]. In an MAS experiment the sample sits inside a rotor which is supported by two air bearings through which bearing gas is blown to stop the rotor hitting the bearing surfaces. On the top and/or bottom of a rotor are a series of fins over which the drive gas is blown. The speed of a rotor is usually measured using a mark on a rotor and an optical sensor. Speeds up to 60 kHz using a 1.8 mm outer diameter rotor have recently become available commercially and speeds reliably up to 70 kHz and very unreliably up to 90 kHz are being achieved by research groups. The bearings and coils are supported in a plastic stator which can be moved so that it is at the magic angle to the magnetic field. Most probes are also double or triple resonance probes, which means that they can pulse and receive at two or three frequencies simultaneously. This is necessary as most spectrometers have a useable bandwidth of one or two MHz which is usually smaller than the gap between the Larmor frequencies of two nuclei. A triple resonance probe still uses one coil, but with a series of notch and band pass filters in the circuit along with variable capacitors and inductors to tune each part of the circuit.

The spectrometer is simply a frequency generator, amplifier and receiver. The pulse is generated with a given frequency and phase, which is then amplified

and delivered to the probe. The signal is received by the pre-amplifier, transmitted to the receiver, mixed with the input frequency where the sum is filtered off and the difference is then digitised and recorded[63]. As the receiver side of the system is very sensitive a series of safety systems stop the initial pulse from being transmitted into the receiver. One system is a $\lambda/4$ cable with one end connected to the probe and the other end connected to the pre-amplifier and a pair of cross diodes which are grounded. During the pulse the voltage at the cross diodes is high enough for them to pass current so the voltage drop across the $\lambda/4$ cable is large. The impedance of the $\lambda/4$ is high so the pulse is transmitted into the probe. During acquisition, the voltage at the cross diodes is low, so they do not allow current to pass to ground so the $\lambda/4$ cable looks like 50 Ω so the signal is passed to the pre-amplifier.

Equipment Used

Field	Magnet Make	Spectrometer Make	Nuclei Studied
18.8T	Magnex	Chemagnetics Infinity Plus	^{93}Nb, ^{65}Cu
14.1T	Magnex	Chemagnetics Infinity	^{93}Nb, ^{65}Cu, ^{27}Al
		Bruker Advance II+	^{115}In
8.45T	Oxford Spectrospin	Chemagnetics Infinity	^{17}O
7.05T	Oxford Spectrospin	Varian Infinity Plus	^{15}N
7.05$\pm$0.5T	Magnex	Chemagnetics Infinity	^{17}O
4.7T	Magnex	Chemagnetics Infinity Lite	^{119}Sn

Table 3.7: Spectrometers used during experiments

The magnets and spectrometers used are shown in table 3.7 and the probes are shown in table 3.8. A series of different experiments were carried out with varying B_1 fields and pulse lengths chosen to suit the situation. For narrow line spectroscopy a relatively weak B_1 field of 20-50 kHz was used with a pulse width of around 5 μs. For wide line static spectroscopy a larger B_1 field of approximately

Field	Manufacturer	Rotor Size(mm)
18.8T	Varian MAS	4.0
18.8T	Varian MAS	2.5
14.1T	Varian T3 MAS	3.2
14.1T	Bruker MAS	2.5
14.1T	Bruker Static	5.0
14.1T	Bruker MAS	3.2
14.1T	Bruker MAS	4.0
7.05T-8.45T	Bruker MAS	4.0
7.05T-8.45T	Apex MAS	4.0
4.7T-8.45T	Doty MAS	4.0

Table 3.8: Probes used for experiments

200 kHz and a pulse width of 0.5 μs was used. The reason for a hard short pulse is that the excitation profile of a pulse is proportional to the inverse of the pulse width. For wider line spectroscopy it is preferable to excite the whole line uniformly hence a short pulse. A short pulse will result in a very small tip angle of the magnetisation vector, requiring a relatively high B_1 field. For narrower lines which can be acquired under MAS a much softer longer pulse is used of 20-50 kHz and a pulse length of 1-4 μs so as to not excite the outer transitions and to put less stress on the equipment.

3.2.1 One Pulse Experiment

A one pulse experiment is a single pulse which tips the magnetisation vector and then after a set delay known as "dead time", the Free Induction Decay (FID) is acquired. This experiment has the advantage of being very simple and being quantitative. This experiment is used on samples which have fairly narrow signals so the FID is long compared to the dead time. Ideally the dead time would be zero. However, due to equipment constraints the dead time is usually in the 10 μs range. The length of the dead time means that for a signal wider than 10 kHz

more than 10% of the signal is lost in the dead time. To get around this problem a spin echo is used.

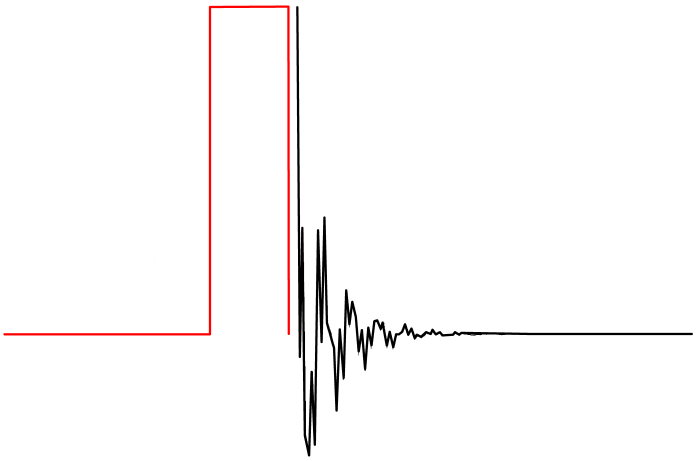

Figure 3.1: A single pulse experiment

For quadrupolar nuclei the rate of rotation of the magnetisation vector is dependent on the size of the electric field gradient (EFG). This is known as nutation rates[64]. The rate of rotation of the magnetisation vector (ν_1) is proportional to C_Q. In the small ($< 5°$) tip angle approximation the tip angle of the magnetisation vector is independent of C_Q so for quadrupolar nuclei the tip angle used in the experiment needs to be small so that the relative intensities of sites with varying C_Q are still quantitative[65].

The length and power of a pulse is also a matter for consideration. The power of a pulse relates to a certain ν_1 value and thus the length of the pulse for a given tip angle. The width of the pulse is linked to the excitation profile of that pulse. The excitation profile of a pulse is approximated as the Fourier Transform (FT) of the excitation pulse.[66] The shorter the pulse, the wider the excitation profile of the pulse and the more power required to achieve the same tip angle. A problem which is linked to this is the excitation of the satellite transitions. The

wider the excitation profile, the more likely the excitation of the satellite transitions. So in a situation where the central transition is being observed and the satellite transitions overlap the central transition, the length of the excitation pulse must be carefully chosen.

3.2.2 Echo and Hard Echo Experiments

There are two types of spin echo. Both consist of two pulses designed to use the T_2 relaxation to refocus the signal so that a signal can be acquired. The Hahn echo consists of a first pulse which tips the magnetisation vector by n°, an evolution time (τ), a second pulse of 2n° with a 180° phase change from the first pulse and after a time τ the spins realign and cause a spin echo. This echo can be observed and results in a signal which is not affected by dead time.

The second variant of this experiment is known as a solid echo. Instead of the second pulse being twice as long as the first pulse, the second pulse is the same length as the first with only a 90° phase change from the first pulse. This pulse sequence is also known as the quadrupole echo as it uses the quadrupolar interaction as a means to produce the echo. The solid echo has the advantage of resulting in a better line shape for very wide lines as the short pulse has a larger bandwidth than a long pulse.

The two pulse sequences have different advantages. The spin echo results in a larger signal, whereas the solid echo results in less distorted line shapes due to the second pulse having a broader excitation profile. These experiments are usually used when a signal is too broad for a single pulse experiment. If the T_2 relaxation

is too short the signal can have decayed before the signal can be acquired. Due to this effect this experiment is only quantitative if the T_2 relaxation of the sample is significantly longer than the evolution time.

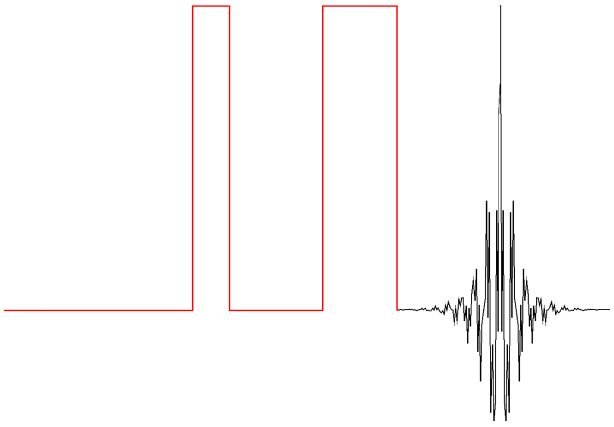

Figure 3.2: A spin echo experiment

3.2.3 Signal Amplification Pulse Sequences

RAPT

The pulse sequence was optimised using $Mg(OH)_2$, with a 1 μs delay between the pulses and a pulse length of 1.3 μs. The RAPT cycle was repeated 150 times and a delay of 10 μs between the end of the RAPT pulse and the beginning of the experiment was used. This resulted in a gain in signal by a factor of 2.1. The width between the RAPT pulses was left short and the width of the pulse optimised for greatest signal, then the length of the RAPT sequence was increased until complete saturation had occurred and increased slightly more to make sure that the same effect would occur in the actual samples.

Cross Polarisation

Cross polarisation uses the population difference of one type of nucleus and transfers it to another. This technique is usually done from protons to another nucleus (high to low gyromagnetic ratio). The technique relies on the dipolar coupling between the two different nuclei to transfer the population differences. In an ideal situation this is done by applying a pulse to both the protons and the other nucleus. The pulses are calibrated so that the rate at which the magnetisation vectors rotate around the B_1 field is the same. This is achieved so that $\gamma_H B_{1,H} = \gamma_X B_{1,X}$ which is known as the Hartmann-Hahn condition. The pulse length is optimised so that the maximum population difference has been transferred. The signal is then usually acquired with decoupling.

A modification of cross polarisation is the use of ramped amplitude modulated pulses (RAMP)[67]. If the dipolar coupling is much greater than the MAS rate then there is a single band which satisfies the Hartmann-Hahn condition and a standard CP experiment in this range can create an efficient transfer of magnetisation. If however the MAS rate is similar in size to the dipolar coupling then there becomes a series of bands which satisfy the Hartmann-Hahn condition and are separated by the spinning speed. Although magnetisation transfer still occurs if a pulse is used at the central band, it is more efficient to produce pulses at all of the bands. This can be done by RAMP-CP, where the CP pulse is swept in amplitude across a chosen range. The sweeping of amplitudes also has the effect that the Hartmann-Hahn condition will be exactly matched at some point for all chemical environments and is less critical on setup of the pulse powers.

Decoupling

Often in materials where CP is used to acquire a signal the dipolar coupling results in broad lines. Using decoupling[68, 69] results in a removal of the dipolar coupling between the two coupled nuclei (usually protons and an element referred to as X). The general idea of decoupling is to keep the protons occupied so that they do not couple with the X nucleus. The simplest method to do this is to apply a continuous wave (CW) on the proton channel during acquisition of the X channel. The CW produces a rapid fluctuation of the protons between Zeeman states. If the fluctuations can be made faster than the interaction between the protons and the X nucleus then the line begins to narrow as the broadening due to heteronuclear dipolar coupling is removed. Often the size of the coupling is relatively large so very high power pulses are required and as heteronuclear dipole coupling has been removed the lines tend to be very narrow which results in a long acquisition time being required. The long acquisition time and the high power results in a lot of stress on the components of a probe which can break down resulting in arcing.

Many people have been researching alternative methods to CW decoupling, one of note is the two pulse phase modulated (TPPM) decoupling[4] which is a series of pulses with alternating phases. Theoretically the time between the pulses is zero, however due to technical constraints there is a very small gap between each pulse. TPPM has proven to be more effective at decoupling than CW and as such less power is required to get the same effect. In TPPM the phase change between the pulses needs to be optimised along with the pulse width. Typical values for this are a phase of $\pm 15^{\circ}$ and a pulse width resulting in a tip angle of approximately 170°.

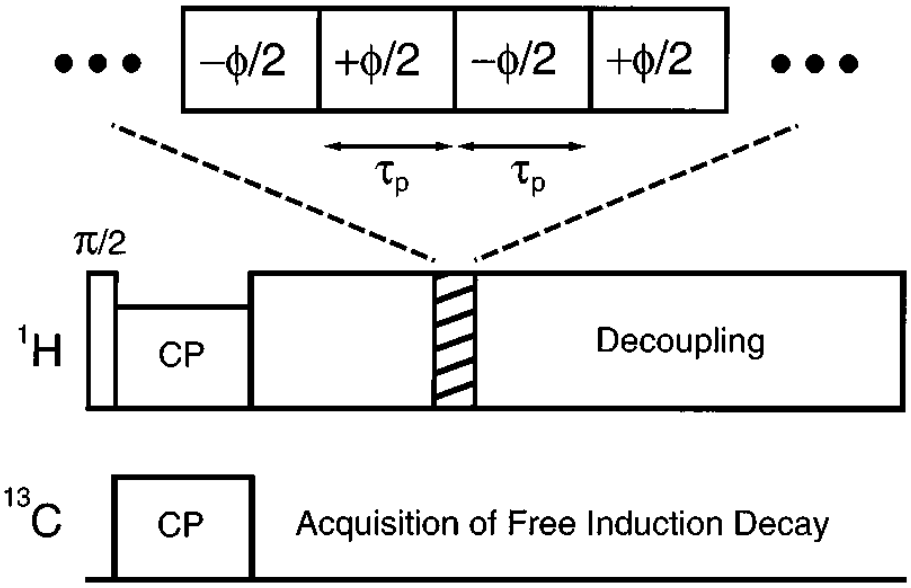

Figure 3.3: A CP pulse sequence using TPPM decoupling. The expanded region shows the TPPM pulse sequence[4].

3.2.4 Determination of T_1 and T_2

A set of simple experiments exist to be able to obtain T_1 and T_2 values. T_1 is useful to know so that the delay period between two experiments can be optimised. If the delay is too short, signal is lost. There is a series of solutions to the maximum amount of signal that can be obtained in a given amount of time. With a 90^o pulse the amount of signal that can obtained in a given amount of time is at a maximum. However, if the pulse delay is slightly too short or the tip angle is slightly too large the amount of signal obtained is dramatically reduced. The advantage with a smaller tip angle is that if the pulse delay is slightly too short or the tip angle slightly too large the effect on the received signal intensity over a given amount of time is much smaller than a similar error when a larger tip angle and pulse delay are used.

To determine T_1, two techniques are usually used. The first involved a simple pulse delay array and determining where the signal has stopped increasing which results in a useable pulse delay. The second, inversion-recovery uses two pulses and measures the size of the signal as a function of time. The pulse sequence consists of a 180^o pulse and a 90^o pulse. The time between the pulses is varied and the size of the signal after the 90^o pulse is measured and follows a relation of $A = A_0(1 - e^{-t/T_1})$.

T_2 is also useful to know as in experiments like QCPMG[70][71] where the T_2 is used to refocus the spins. If acquisition continues after the signal has died away due to T_2 the overall signal is reduced in quality as noise is being added onto the signal. Also, if two sites in a material have different T_2 values and a spin echo is being used, the relative intensities will be incorrect and using the T_2 values for each site the relative intensities can be corrected.

To determine T_2 a 90^o-τ-180^o pulse sequence is used and the size of the echo formed is measured as a function of the time between the pulses. In liquids the amplitude of the echo follows the relation of $A = A_0 e^{-2\tau/T_2}$.

Chapter 4

Simulation Program QuadFit

A program called QuadFit has been written which is designed to make retrieval of information from solid state NMR spectra of amorphous materials possible. A similar program, also known as QuadFit, was written during my MSc[72]. This original program was written in Visual Basic and had the ability to simulate quadrupolar line shapes with $\eta = 0$ and distributions of C_Q for either static or MAS samples. The version of QuadFit produced during my MSc also had the ability to produce CSA line shapes without distributions. The new version of QuadFit written as part of my PhD has the ability to simulate the quadrupolar interaction under MAS, and CSA and quadrupolar (1^{st} and 2^{nd} order) interactions whilst static, including combined interactions. To make the retrieval of information possible QuadFit is capable of simulating lines with distributions of interaction parameters, using a Gaussian distribution for quadrupolar and CSA lines or a Czjzek distribution for quadrupolar lines. The program has been written using Java to allow for cross platform compatibility and absolute stability. The user interface is fairly simple, with a series of keyboard shortcuts to increase the speed of fitting. To reduce the

complexity and thus increase the speed of calculations perfect pulses are assumed and only the static and infinite spinning speed limits are considered. This has the effect of reducing the number of variables in the fit, although it does limit the accuracy. Although programs like Simpson[73] can take into account all of the possible parameters, QuadFit has the advantage of being able to calculate line-shapes very quickly making fitting of a spectra possible in relatively short periods of time.

For a given interaction, if the sample is a single crystal the effect on the spectra will be to shift the resonance.[74] For a given interaction strength the amount the resonance is shifted is dependent on the angle of the single crystal to the magnetic field.[75] For a powder, there are many single crystals which are randomly orientated so a "powder pattern" needs to be calculated which takes into account the random orientations of the individual components. The simplest form of calculating the powder pattern is to calculate the shift of the resonance for all given orientations. Calculating a powder pattern can be done by using Sphere Stepping (SS)[76] where the whole sphere is stepped round in a given step size. This can be very time consuming with a single line taking 75 s to produce and a distribution taking hours. An alternative method is using Alderman-Grant Interpolation (AGI)[77], as described later. The speed gains can be dramatic. Figure 4.1 shows simulated spectra using the two different methods and Table 4.1 compares the methods.

Line	Type of Tiling	Speed of Calculation	Relative Speed
A	AGI	$\sim$1.6s$\Rightarrow$2mins 40s	47
	19,800 Field Directions	for a 100 line distribution	
B	AGI	$\sim$0.13s$\Rightarrow$13s	577
	1,740 Field Directions	for a 100 line distribution	
C	SS	$\sim$75s$\Rightarrow$2hours	1
	25.9×10^6 Field Directions	for a 100 line distribution	
D	SS	$\sim$3s$\Rightarrow$5mins	25
	1.04×10^6 Field Directions	for a 100 line distribution	

Table 4.1: Comparison of Alderman-Grant Interpolation and Sphere Stepping

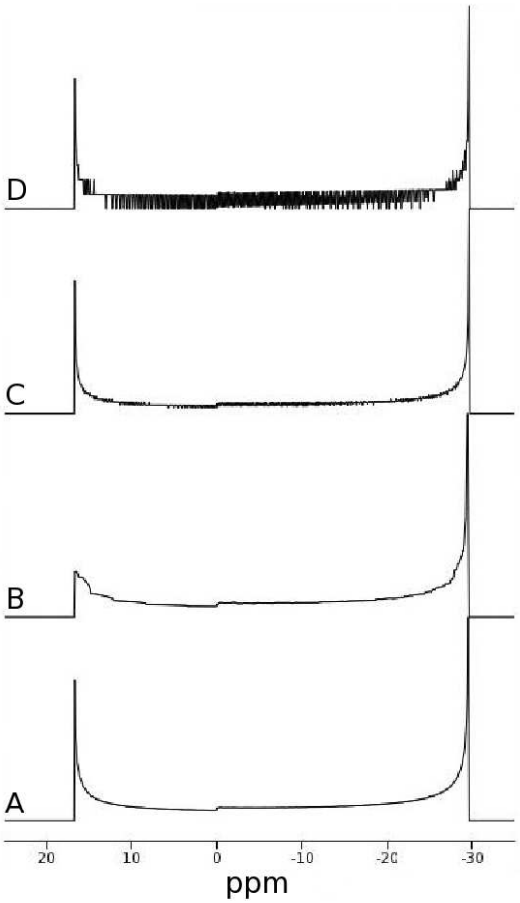

Figure 4.1: Speed and quality comparison of Alderman-Grant Interpolation (A:- 19,800 and B:- 1,740 field directions) and Sphere Stepping methods(C:-25.9×10^6 D:-1.04×10^6) field directions.

4.1 Alderman-Grant Interpolation

Alderman-Grant interpolation[77] involves calculating the field directions by using an octahedron instead of a sphere. This has many advantages, not least reducing the calculation times for a powder pattern.

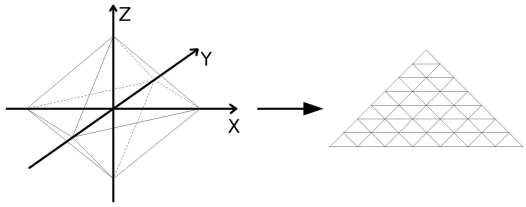

Figure 4.2: Depiction of method behind Alderman-Grant interpolation. Black lines are Cartesian axes. Lines on one face of octahedral are lines of constant x,y,z leading to a triangular segmentation of each face

Each face of the octahedron is broken down into triangles. For each corner of each triangle the distance from the centre is calculated and the frequency of the point is calculated for that field direction. For each triangle the corners are sorted by frequency to produce a "tent".

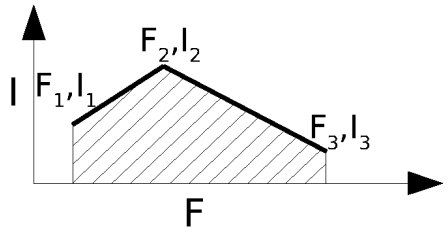

Figure 4.3: Frequencies sorted and plotted against intensity, area is proportional to solid angle at the centre of the octahedron.

The area of the tent is then scaled using the solid angle of the triangle as subtended at the centre of the octahedron. Then the tents are all added together to give a final line shape.

All the orientation-dependent functions (orientations as defined in section 4.5.1) depend on cosine theta and not sine theta. This means the bottom half of the octahedron does not need to be considered as 0^o theta is in the x,y plane. This method is effective due to not needing to calculate complicated sine and cosine functions as these can be determined from the x,y,z co-ordinates of each vertex. During normal sphere stepping the intensity from any one point needs to be corrected by the sine of the angle between the vector for that point to the vector for the pole. This occurs due to the increased spacial density of points which are calculated near the poles. Due to the way the octahedron is split up the number of points over any area is constant which results in a reduction in the number of points calculated at the poles and the removal of the need to multiply each intensity by the sine function.

4.2 Capabilities

Second-order quadrupolar and chemical shift anisotropy are handled for half-integer spin nuclei spinning and both half-integer and integer spin nuclei static. Combinations of the interactions are also supported in the static case. Distributions of interaction parameters are also supported in all cases. To produce a line shape with a distribution of interaction parameters a series of lines are calculated using Alderman-Grant Interpolation[77] with varying interaction parameters. These lines are then added together with scaling depending on the centre and width of the distribution. Different distributions can be used including flat, Gaussian and Czjzek[78]. The Czjzek distribution was designed for a distribution in quadrupolar interactions using an ionic model[79, 80] and tries to correlate the change in C_Q

with asymmetry. As such the Czjzek distribution can only be used for sites which have non-zero asymmetry and a distribution in either or both asymmetry and field gradients.

Due to the number of parameters which are available to fit a spectrum multiple magnetic field data are required to produce an accurate fit. The chemical shift, centre and width of the distributions should stay approximately constant. The broadening however is allowed to change. With a good set of spectra at 3 or more magnetic fields, fits as accurate as $\pm$ 0.1ppm for isotropic shifts, $\pm$ 0.05MHz centre/width for C_Q and $\pm$ 0.05 for the asymmetry are achievable.

In figure 4.4 an example of a complicated fit is shown. This fit was performed by keeping the interaction parameters the same between the fields and changing them until a good fit was obtained at all fields. The results are shown in table 4.2. Despite there being 5 overlapping sites the interaction parameters were obtained to a high degree of accuracy as shown in table 4.2. The high field data yield information about the positions of any singularities whilst the low field data are very sensitive to changes in the centre and width of any distributions.

Site	1	2	3	4	5
δ_{iso} **(ppm)**	43.6±1.3	33.0±2.2	26.3±2.2	15.4±2.5	8.4±1.0
C_Q **Centre (MHz)**	5.0±0.1	3.9±0.1	4.0±0.1	10.5±0.1	4.0±0.1
C_Q **Width (MHz)**	1.0±0.1	1.1±0.1	1.0±0.1	0.0±0.1	0.0±0.1
Broadening (Hz)	150±10	150±10	150±10	450±25	700±100
Intensity (%)	29.0±3.0	9.1±3.0	3.8±0.5	49.2±0.5	9.0±3.5

Table 4.2: Fitting Parameters for Al_5BO_9 Mullite, η=0 in all cases.

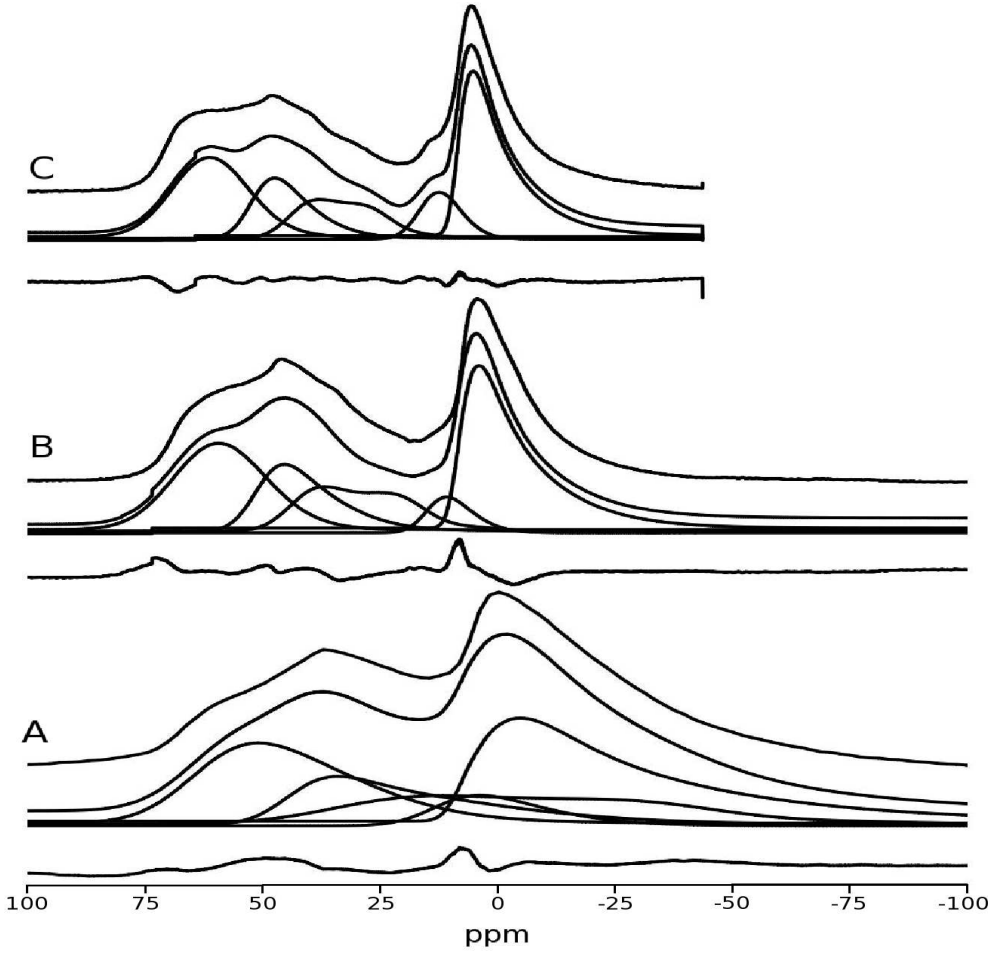

Figure 4.4: ^{27}Al MAS NMR spectra of Al_5BO_9 Mullite at A:-8.46T, B:-14.1T and C:-18.8T

4.3 Effects of Distributions

4.3.1 Chemical Shift Anisotropy Whilst Static

From figure 4.5 it can be seen that the effects of different types of distribution are fairly obvious. If there is a distribution in span (B) there is a general broadening of both the left and the right hand steps, however the central singularity stays sharp. With a distribution in skew (C) the central singularity becomes broadened

and the left and right steps broaden slightly. With a combination of using the central singularity and the broadening of the outer steps an accurate fit can be obtained. However if another form of broadening is present which is not known, multiple field data will have to be used to constrain the fit. This is possible as the CSA interaction scales with field.

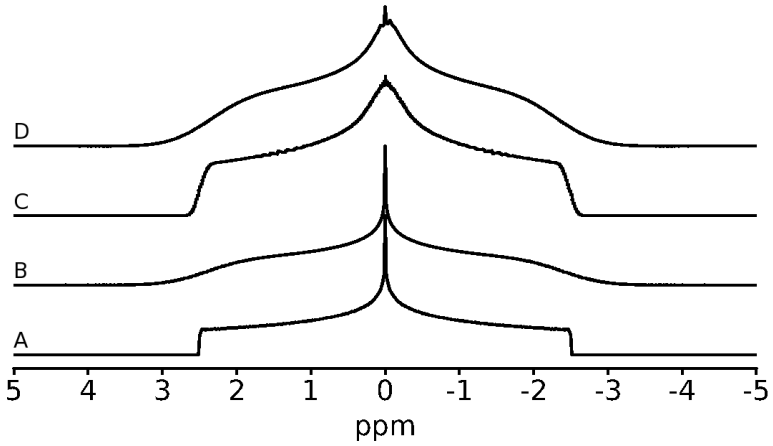

Figure 4.5: CSA line shapes with A:- no distribution, B:- distribution in span, C:- distribution in skew and D:- distribution in both span and skew.

Line	A	B	C	D
Span Centre (ppm)	5	5	5	5
Span Width (ppm)	0	2	0	2
Skew Centre	0	0	0	0
Skew Width	0	0	0.3	0.3

Table 4.3: Parameters for CSA line shapes in figure 4.5

4.3.2 Static 2^{nd}-Order Quadrupolar

From figure 4.6 it can be seen that adding a distribution in C_Q (B) causes the two singularities to broaden, with the step in the centre of the spectra remaining unaffected. Adding a distribution in asymmetry (C) results in a broadening of the

right hand peak more than the left hand one and the step in the centre is also broadened. By taking careful account of the relative widths of the two peaks and whether the step in the centre has been broadened the amount of distribution in both asymmetry and C_Q can be estimated. As the differences are relatively subtle, if there is more than one site, multiple magnetic field data will probably be required.

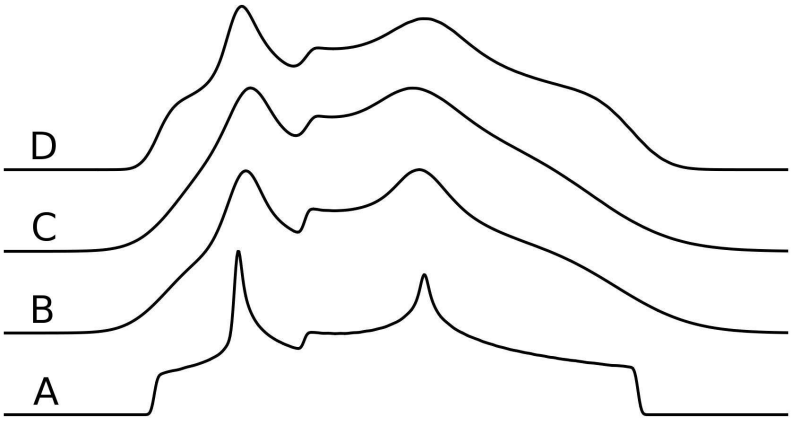

Figure 4.6: Static second-order quadrupolar line shapes showing the central transition with A:- no distribution, B:- a distribution in C_Q, C:- a distribution in asymmetry and D:- a distribution in both asymmetry and C_Q (See table 4.4)

Line	A	B	C	D
C_Q Centre (MHz)	5	5	5	5
C_Q Width (MHz)	0	0.5	0	0.5
η Centre	0.5	0.5	0.5	0.5
η Width	0	0	0.3	0.3

Table 4.4: Parameters for figure 4.6

4.3.3 Central Transition 2^{nd}-Order Quadrupolar Interaction under MAS

The effects of adding various distributions for second-order quadrupolar lines under magic angle spinning are shown in figure 4.7. By adding a distribution in C_Q (B) the left hand singularity only broadens slightly whilst the right hand singularity is broadened much more dramatically resulting in a tail. By adding a distribution in asymmetry (C) to the line a much more complicated line appears. A shoulder appears on the left which is heavily broadened and the right hand peak remains relatively unbroadened. When a distribution of both C_Q and asymmetry are used, the shape of the tail allows the C_Q to be constrained, and the shape of the shoulder on the left allows the asymmetry to be constrained. However due to the number of parameters and the amount of information in the line, often multiple magnetic field data is required to constrain the total fit accurately.

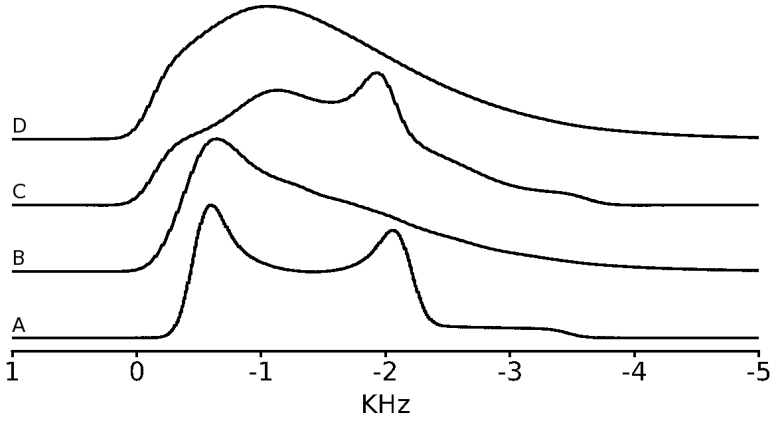

Figure 4.7: Second order quadrupolar line shapes under infinite speed magic angle spinning with A:- no distribution, B:- distribution of C_Q, C:- distribution in asymmetry and D:- a distribution in asymmetry and C_Q

Line	A	B	C	D
C_Q Centre (MHz)	6	6	6	6
C_Q Width (MHz)	0	2.5	0	2.5
η Centre	0	0	0.5	0.5
η Width	0	0	0.2	0.2

Table 4.5: Parameters for figure 4.7

4.3.4 Quadrupolar Interaction for Integer Spin Nuclei

Due to there not being a dominant central transition, all of the transitions have to be accounted for with integer spin nuclei. The outer transitions produce very broad resonances and as such are usually ignored. As the lines are so wide often spinning is unable to fully narrow the interaction so it is usual to acquire static spectra of integer spin nuclei. The advantage with integer spin nuclei is that the amount of information contained in the spectra due to extra transitions is larger than the central transition of half-integer spin nuclei. The extra information comes from the different transitions which are essentially acting as multiple field data. The increased information in the spectra can lead to a very accurate fit, with the interaction parameters being highly constrained. As can be seen from figure 4.8 some of the features of the line are unaffected by distributions in C_Q (B) or asymmetry (C). Using the shape of these shoulders an accurate fit can be obtained. The only problem with this method is that a high signal to noise ratio is required. Coupled with the lines being very wide this means that spectra can take up to a week to obtain. Due to the often very large line width a method known as field sweeping can be used. Field sweeping required a spectrum to be acquired at one frequency, then the field is changed slightly and another spectrum is acquired. This method is analogous to frequency stepping, but instead of moving the frequency, the line is moved instead.

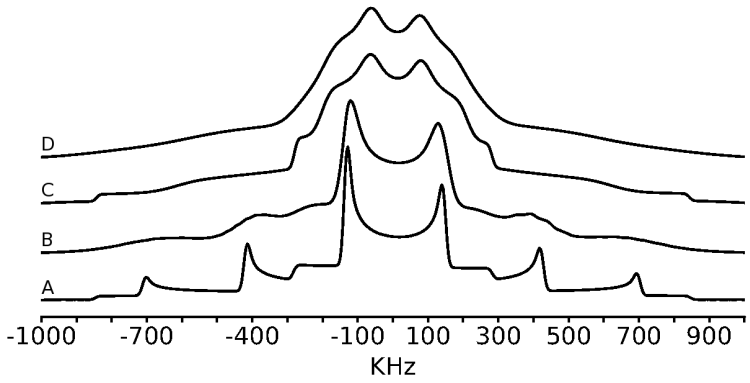

Figure 4.8: First and Second-order quadrupolar line shapes for an I=3 nucleus with A:- no distribution, B:- distribution in C_Q, C:- a distribution in asymmetry and D:- a distribution in both asymmetry and C_Q

Line	A	B	C	D
C_Q Centre (MHz)	5	5	5	5
C_Q Width (MHz)	0	1	0	1
η Centre	0	0	0.5	0.5
η Width	0	0	0.2	0.2

Table 4.6: Parameters for figure 4.8

Figure 4.9 shows a static ^{10}B NMR spectrum of B_2O_3. The advantage of ^{10}B as opposed to ^{11}B (spin-$\frac{3}{2}$) is that due to ^{10}B being integer spin the quadrupole interaction is much more pronounced so can be determined more accurately[81]. Separation of similar sites is possible due to slight differences in the quadrupole interaction rather than the chemical shift. In contrast to ^{10}B, ^{11}B spectra can be difficult to deconvolve because of the small line widths of different sites in the central transitions, resulting in the features of different sites being indistinguishable. The effect of using distributions on the fit of the spectra are shown in figure 4.9. In this case, from the spectra there is no evidence of a distribution in asymmetry and the C_Q has been constrained accurately. A paper concerning ^{10}B NMR spectra using this QuadFit approach has been recently published[82].

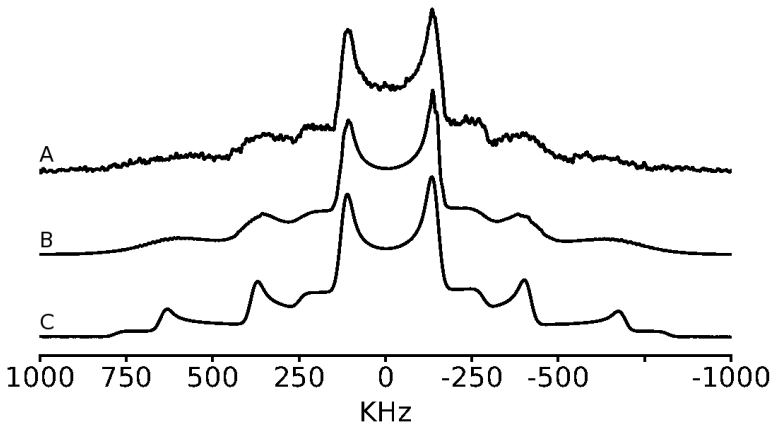

Figure 4.9: A:- ^{10}B NMR spectrum of B_2O_3 using a field swept 7.05T Varian-Chemagnetics spectrometer, B:- Fit using a distribution in C_Q and C:- a fit without any distributions

Line	B	C
Broadening (kHz) $\pm$ 1.0	0	14.2
Shift (ppm) $\pm$ 50	-620	-620
C_Q Centre (MHz) $\pm$ 0.2	5.2	5.2
C_Q Width (MHz) $\pm$ 0.1	1.6	0
$\eta \pm$ **0.1**	0	0

Table 4.7: Parameters for figure 4.9

4.3.5 Combined CSA and Quadrupolar Interactions Whilst Static

Line	B	C
Broadening (Hz)	3200	2000
Shift (ppm)	-563.5	-563.5
Span (ppm)	137.3	137.3
Skew	-0.6	-0.6
C_Q Centre (MHz)	0.55	0.55
C_Q Width (MHz)	0.2	0
η_Q	0	0
α	0	0
β	70	70
γ	0	0

Table 4.8: Parameters for figure 4.10

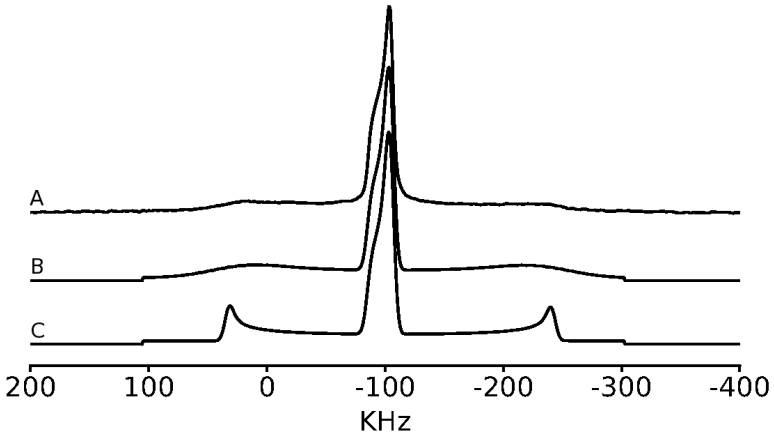

Figure 4.10: A:-^{65}Cu static NMR spectrum of $CuInSe_2$ taken on a 14.1T Varian-Infinity Plus, B:- Fit using combined CSA and Quadrupolar with a distribution of C_Q, C:- Fit using combined CSA and Quadrupolar without any distributions

Figure 4.10 shows a fit using combined CSA and quadrupolar interactions. This occurrence is fairly common in some quadrupolar nuclei. If the CSA cannot be spun out or information from it is required, this method can result in some useful information. Due to the CSA and the quadrupolar interactions not necessarily having the same principal axis system another 3 parameters known as the Euler angles must be taken into account[83]. This results in a total of 7 parameters if no distributions are required. If distributions are required the number of parameters can reach 11 without taking account of intensity, broadening and isotropic shift. This requires multiple magnetic field data to constrain the fit and extract the information or some information to be previously known, such as the quadrupolar interaction parameters. The advantage with this technique is that if the quadrupolar interaction is small enough, the outer transitions can be observed and used to constrain quadrupolar interaction parameters. With the small C_Q the central transition is dominated by the CSA interaction which can then have its parameters determined. The relative orientation of the two systems can then be determined

by the position of the features of the outer transition relative to the central, CSA dominated, peak. This method results in approximations for the Euler angles and fairly accurate results of the CSA and quadrupolar interactions. Distributions in this case are relatively easy to use as the interactions can be treated separately. The CSA interaction fits as a simple line without any distributions, however the outer transitions of the quadrupolar interaction require a distribution in C_Q for a good fit to be obtained. To constrain all of the parameters accurately up to 4 fields could be required with a high enough signal to noise ratio that all the features of the lines are easily visible.

Effects of Distributions on Line Shape

As the differences caused by different distributions of interactions can be subtle it is best to view them as the magnetic field changes. For this reason a series of plots have been produced which have various distribution and mixtures of distributions at two different fields. The second order quadrupolar interaction (in Hz) scales

Line	ν_L **MHz** **MHz**	C_Q **Centre** **MHz**	C_Q **Width** **MHz**	η **Centre**	η **Width**	**Span Centre ppm**	**Span Width ppm**	**Skew Centre**	**Skew Width**
A	156.33	5	0	0.5	0	50	0	0.5	0
B	78.17	5	0	0.5	0	50	0	0.5	0
C	156.33	5	0.5	0.5	0	50	0	0.5	0
D	78.17	5	0.5	0.5	0	50	0	0.5	0
E	156.33	5	0	0.5	0.3	50	0	0.5	0
F	78.17	5	0	0.5	0.3	50	0	0.5	0
G	156.33	5	0	0.5	0	50	10	0.5	0
H	78.17	5	0	0.5	0	50	10	0.5	0
I	156.33	5	0	0.5	0	50	0	0.5	0.3
J	78.17	5	0	0.5	0	50	0	0.5	0.3

Table 4.9: Parameters for figure 4.11

inversely with magnetic field and the chemical shift interaction (in Hz) scales with field. Using this the contributions to the line shape can be determined using multi-

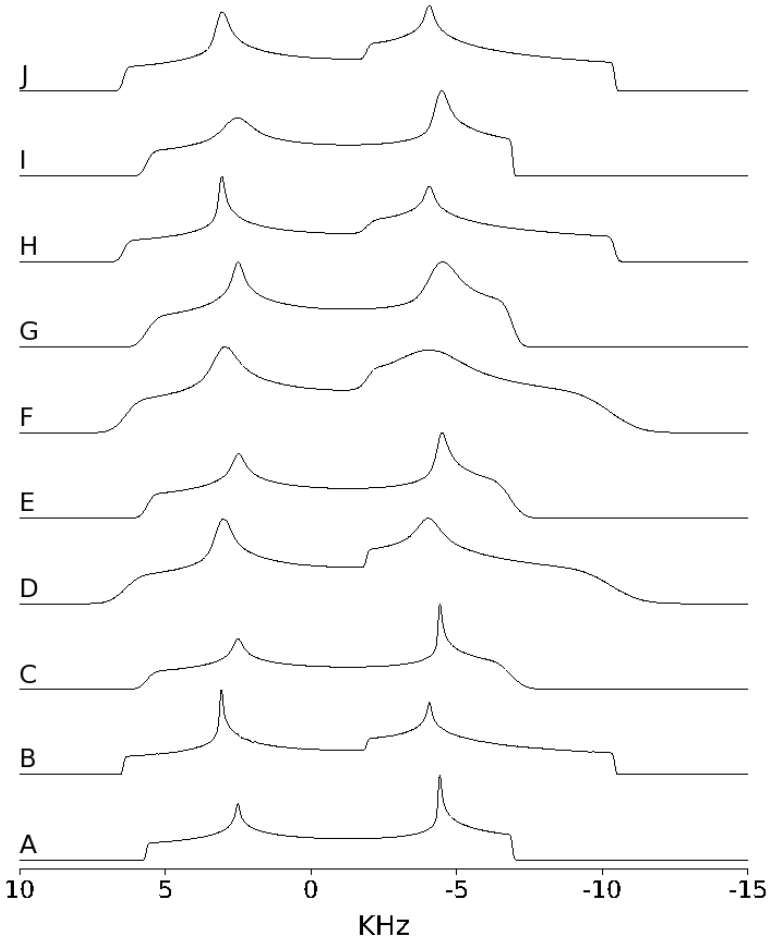

Figure 4.11: Showing the effect of various distributions on line shape at variable magnetic field. The CSA and quadrupole tensors are assumed to be coincident and the spin is $\frac{5}{2}$ in these simulations. Parameters are shown in table 4.9

ple magnetic field data. This is best shown by lines A and B in figure 4.11. When changing magnetic field the singularities both move by a small amount, but not significantly, implying that both quadrupolar and chemical shift interactions make contributions to the singularities. The shoulder at lower frequency significantly reduces in intensity as the field increases implying it is dominated by the quadrupolar interaction. When a distribution in C_Q is added, a general broadening occurs with the singularity at lower shift being more broadened than the singularity at higher

shift. The shoulders also broaden and as expected the broadening becomes worse at lower field. With a distribution in the asymmetry parameter there is a slight broadening of the whole line at higher fields, however the broadening of the lower shift half of the line is much more significant than the high shift side of the line. Again it is obvious that the broadening is due to a quadrupolar interaction as the broadening is worse at lower fields. With the distributions in span and skew they are both worse at higher field. The distributions in span have the effect of broadening the whole line whilst the distribution in skew does not broaden the shoulder at low shift. Using the broadening variations with field and noting which features change, the line can be fitted accurately.

Line	ν_L **MHz** **MHz**	C_Q **Centre** **MHz**	C_Q **Width** **MHz**	η **Centre**	η **Width**	**Span Centre ppm**	**Span Width ppm**	**Skew Centre**	**Skew Width**
A	156.33	5	0.5	0.5	0.5	50	0	0.5	0
B	78.17	5	0.5	0.5	0.5	50	0	0.5	0
C	156.33	5	0.5	0.5	0	50	10	0.5	0
D	78.17	5	0.5	0.5	0	50	10	0.5	0
E	156.33	5	0.5	0.5	0	50	0	0.5	0.3
F	78.17	5	0.5	0.5	0	50	0	0.5	0.3
G	156.33	5	0	0.5	0.3	50	10	0.5	0
H	78.17	5	0	0.5	0.3	50	10	0.5	0
I	156.33	5	0	0.5	0.3	50	0	0.5	0.3
J	78.17	5	0	0.5	0.3	50	0	0.5	0.3
K	156.33	5	0	0.5	0	50	10	0.5	0.3
L	78.17	5	0	0.5	0	50	10	0.5	0.3

Table 4.10: Parameters for simulations shown in figure 4.12

Once more than one parameter has a distribution it becomes much more difficult to determine which parameters have the distributions. Distributions which are entirely due to either the chemical shift or quadrupolar interaction are simple to spot as at either low or high field respectively the signal narrows and then the features of the lines can be used to work out which features are being broadened due to which distribution. If however the broadening is due to a mixture of the

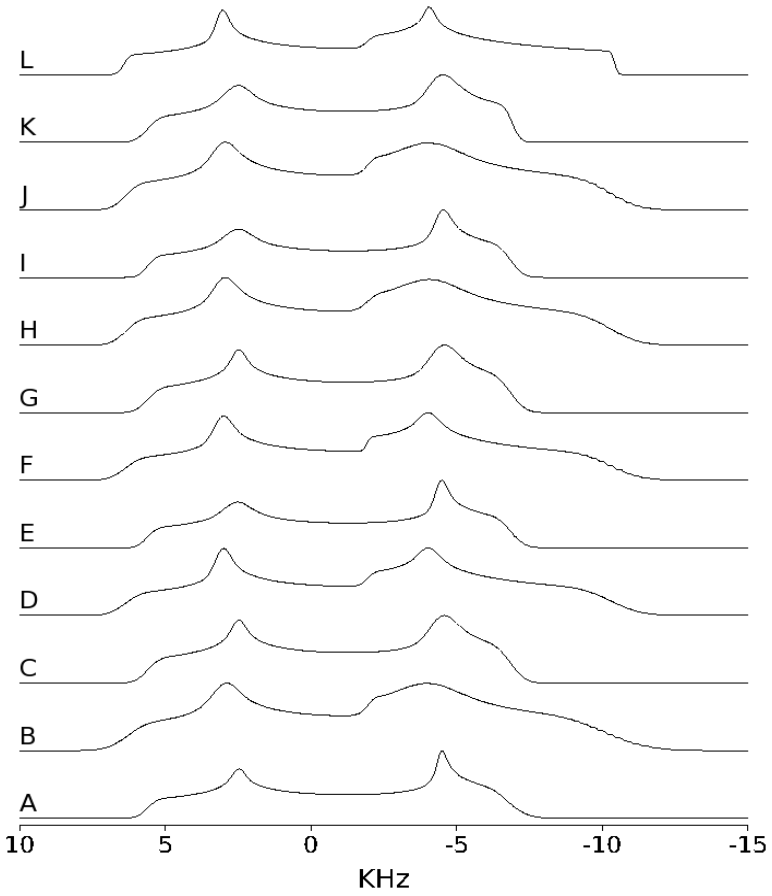

Figure 4.12: Showing the effect of various distributions on line shape at variable field. The CSA and quadrupole tensors are assumed to be coincident and the spin is $\frac{5}{2}$ in these simulations. Parameters are shown in table 4.10

two interactions as shown in figures 4.12 and 4.13, distinguishing which parameters have distributions is very difficult. As can be seen any line with a distribution in asymmetry has a significantly broadened singularity and shoulder on the low shift side. Along with careful consideration and multiple magnetic field data the different distributions and interactions can be determined.

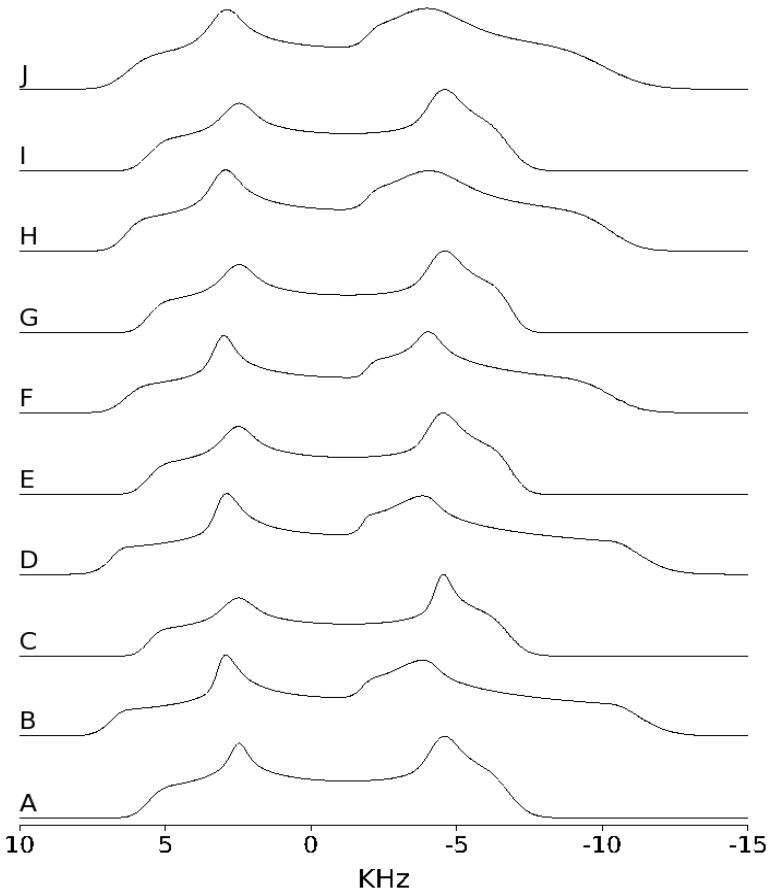

Figure 4.13: Showing the effect of various distributions on line shape at variable field. The CSA and quadrupole tensors are assumed to be coincident and the spin is $\frac{5}{2}$ in these simulations. Parameters are shown in table 4.11

Line	ν_L **MHz** **MHz**	C_Q **Centre** **MHz**	C_Q **Width** **MHz**	η **Centre**	η **Width**	**Span Centre ppm**	**Span Width ppm**	**Skew Centre**	**Skew Width**
A	156.33	5	0.5	0.5	0.3	50	10	0.5	0
B	78.17	5	0.5	0.5	0.3	50	10	0.5	0
C	156.33	5	0.5	0.5	0.3	50	0	0.5	0.3
D	78.17	5	0.5	0.5	0.3	50	0	0.5	0.3
E	156.33	5	0.5	0.5	0	50	10	0.5	0.3
F	78.17	5	0.5	0.5	0	50	10	0.5	0.3
G	156.33	5	0	0.5	0.3	50	10	0.5	0.3
H	78.17	5	0	0.5	0.3	50	10	0.5	0.3
I	156.33	5	0.5	0.5	0.3	50	10	0.5	0.3
J	78.17	5	0.5	0.5	0.3	50	10	0.5	0.3

Table 4.11: Parameters for simulations shown in figure 4.13

4.4 Interface

When the program is started a window appears where the Larmor frequency and the spin of the nucleus can be set. Once the Larmor frequency and spin have been set they cannot be changed. The next step in the program is the main interface.

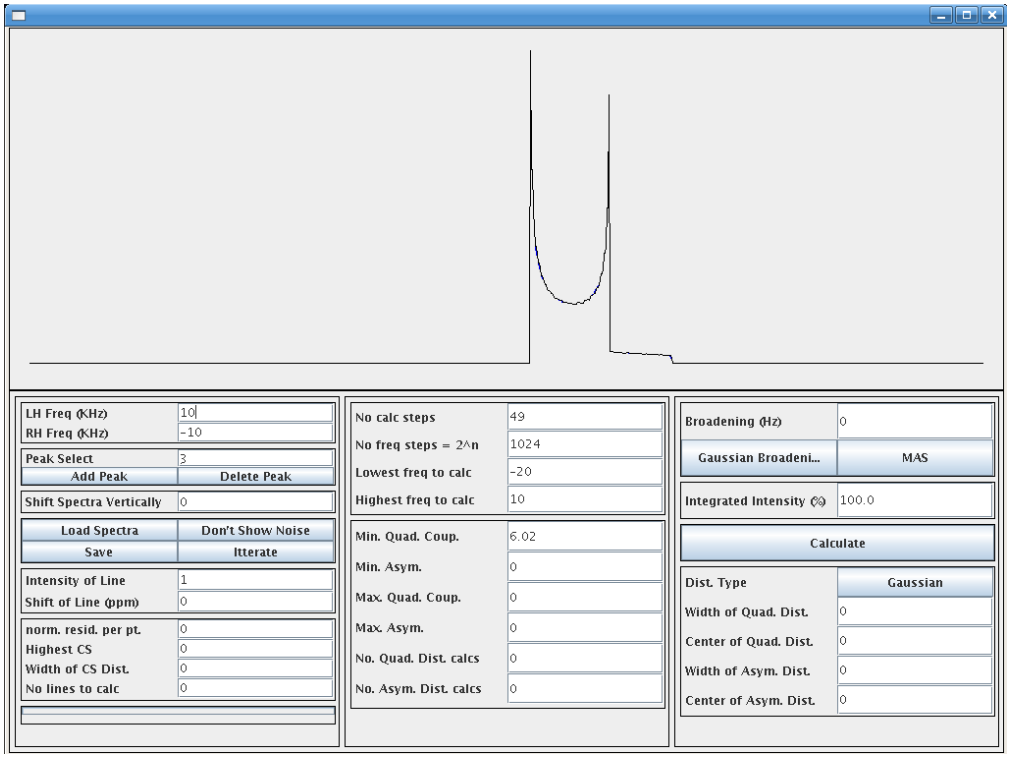

Figure 4.14: Interface for QuadFit, shows a line shape with quadrupole asymmetry = 0, quadrupole coupling constant = 6.02MHz, Larmor frequency = 156.33MHz and a spin of $\frac{5}{2}$.

The interface is split into a series of different sections. The left panel contains window control, peak controls (adding, shift and intensity) and loading and saving of spectra. The central panel contains the calculation parameters. The right panel contains broadening, integrated intensity and the distribution parameters of the interactions. When a combined CSA and quadrupolar line is selected as the line type, another window opens which contains all of the parameters which

can be altered including the calculation ranges for the distribution parameters.

The program is designed to allow fast changing of the centre, width and type of distributions. To add a distribution, once the line has been added to the fit, choose the type of line, the range over which the line is to be calculated in frequency space and the range of interaction parameters over which the line needs to be calculated. Once this is done the program calculates the lines and stores them, so if the centre and width of the distribution changes the way the lines are added together is changed and all the lines are not recalculated. If any of the parameters are changed apart from the centre or width of the distribution, height, shift and broadening, then the lines will have to be recalculated.

4.5 Conventions and Equations used for Interactions

4.5.1 Central Transition Second-Order Quadrupolar Interaction under MAS

The standard conventions are used here, where $C_Q = \frac{e^2qQ}{h}$ and $\eta = \frac{V_{XX}-V_{YY}}{V_{ZZ}}$. θ is the angle between the B_0 field direction and the PAS of the quadrupolar tensor. ϕ is then the angle from an arbitrary axis which is perpendicular to the B_0 field to the X axis of the PAS of the quadrupolar interaction. The limit of infinite speed spinning is used so no spinning side bands are calculated. Although this is not as

accurate as other methods the advantages in computational time are significant.

$$a = \frac{21}{16} - \frac{7}{8}\eta cos2\phi + \frac{7}{48}\left(\eta cos2\phi\right)^2$$
$$b = -\frac{9}{8} + \frac{1}{12}\eta^2 + \eta cos2\phi - \frac{7}{24}\left(\eta cos2\phi\right)^2$$
$$c = \frac{5}{16} - \frac{1}{8}\eta cos2\phi + \frac{7}{48}\left(\eta cos2\phi\right)^2$$

$$\nu_{MASQ} = \frac{-1}{6 \cdot \nu_L}\left(\frac{3C_Q}{2I(2I+1)}\right)^2 \cdot \left(2I\left(2I+1\right) - \frac{3}{4}\right) \cdot \left(a \cdot cos^4\theta + b \cdot cos^2\theta + c\right) \text{[56]} \tag{4.1}$$

4.5.2 Second-Order Quadrupolar Interaction for a Static Sample

The same conventions are used here as in the spinning case.

$$a = -\frac{27}{8} - \frac{9}{4}\eta cos2\phi - \frac{3}{8}\left(\eta cos2\phi\right)^2$$
$$b = \frac{15}{4} - \frac{1}{2}\eta^2 + 2\eta cos2\phi + \frac{3}{4}\left(\eta cos2\phi\right)^2$$
$$c = -\frac{3}{8} + \frac{1}{3}\eta^2 + \frac{1}{4}\eta cos2\phi - \frac{3}{8}\left(\eta cos2\phi\right)^2$$

$$\nu_{staticQ} = -\frac{1}{6 \cdot \nu_L}\left(\frac{3 \cdot C_Q}{2I(2I-1)}\right)^2 \cdot \left(I(I+1) - \frac{3}{4}\right) \cdot \left(a \cdot cos^4\theta + b \cdot cos^2\theta + c\right) \text{[84]} \tag{4.2}$$

4.5.3 Quadrupolar Interaction for Integer Spin Nuclei

The same conventions are used as for the half-integer spinning case, however as there is no dominant central transition all of the transitions must be calculated. The scaling factor used for the different transitions is $I(I+1) - m(m-1)$, where the transitions are from $m \rightarrow m-1$.

$$a = \frac{1}{2}\left[\left(I + \frac{3}{2}\right)\left(I - \frac{1}{2}\right) - 3\left(m - \frac{1}{2}\right)^2\right]$$

$$b = 4\left[\left(I+\frac{3}{2}\right)\left(I-\frac{1}{2}\right)-6\left(m-\frac{1}{2}\right)^2\right]$$

$$c = 12I(I+1)-40m(m-1)-27$$

$$d = \frac{1}{2}(3I(I+1)-5m(m-1)-6)$$

$$e = 8I(I+1)-20m(m-1)-15$$

$$A = 3cos^2\theta - 1 + \eta cos2\phi - \eta cos2\phi cos^2\phi$$

$$\begin{aligned} C =& a\big(cos^4\theta\,(3-\eta cos2\phi)^2 + 2cos^2\theta\,\big(-9+2\eta^2-(\eta cos2\phi)^2\big) \\ &+ (3+\eta cos2\phi)^2\big) + b\big(cos^4\theta(3-\eta cos2\phi)^2 \\ &+ cos^2\theta\big(-9+\eta^2+6\eta cos2\phi-2(\eta cos2\phi)^2\big) + \big(\eta^2 cos2\phi\big)^2\big) \end{aligned}$$

$$\begin{aligned} E =& c\left[cos^2\theta(3-\eta cos2\phi)^2\right]^3 + cos^4\theta\big[-36+3\eta^2+42\eta cos2\phi \\ &- \eta^3 cos2\phi - 19(\eta cos2\phi)^2 + 3(\eta cos2\phi)^3 + cos^2\theta\big\{9-4\eta^2-15cos2\phi\eta \\ &+ 2\eta^4 cos2\phi + 11(\eta cos2\phi)^2 - 3(\eta cos2\phi)^3\big\} + \big\{\eta^4 cos2\phi \\ &- (\eta cos2\phi)^2 + (\eta cos2\phi)^3\big\}\big] + d\big[\,\big\{cos^2\theta(3-\eta cos2\phi)\big\}^3 \\ &+ cos^4\theta\big\{-63+12\eta^2+33\eta cos2\phi-4\eta^3 cos2\phi-13(\eta cos2\phi)^2 \\ &+ 3(\eta cos2\phi)^3\big\} + cos^2\theta\big\{45-4\eta^2-9cos2\phi\eta+4\eta^3 cos2\phi-(\eta cos2\phi)^2 \\ &- 3(\eta cos2\phi)^3\big\} + \big\{-9+3\eta cos2\phi+5(\eta cos2\phi)^2+(\eta cos2\phi)^3\big\}\big] \\ &+ e\big[\,\big\{cos^2\theta(3-\eta cos2\phi)\big\}^3 + cos^4\theta\big\{-54+9\eta^2+36\eta cos2\phi \\ &- 3\eta^3 cos2\phi - 15(\eta cos2\phi)^2 + 3(\eta cos2\phi)^3\big\} + cos^2\theta \\ &\cdot\big\{27-6\eta^2-9cos2\phi\eta+4\eta^3 cos2\phi-3(\eta cos2\phi)^2-3(\eta cos2\phi)^3\big\} \\ &+ \big\{-3\eta^2-\eta^3 cos2\phi+3(\eta cos2\phi)^2+(\eta cos2\phi)^3\big\}\big] \end{aligned}$$

$$\nu_Q = \frac{3C_Q}{2I(2I-1)}$$

$$\begin{aligned}\nu_{stat,int,Q} = \nu_Q \frac{1}{2}\left(m-\frac{1}{2}\right)A + \left(\frac{3C_Q\nu_Q}{144I(2I-1)}\right)C \\ + \left(\frac{3C_Q\nu_Q^2}{288I(2I-1)}\right)E\left(m-\frac{1}{2}\right)\text{[85]}\end{aligned} \tag{4.3}$$

4.5.4 Chemical Shielding

The Herzfeld-Berger convention[86] has been used for the chemical shielding. The isotropic shift is defined as

$$\delta_{iso} = -\frac{\sigma_{11}+\sigma_{22}+\sigma_{33}}{3}$$

the span is defined as[87]

$$W = \sigma_{33} - \sigma_{11}, W \geq 0$$

and the skew is defined as

$$k = \frac{3(\sigma_{22}-\sigma_{iso})}{W}, 1 \geq k \geq -1.$$

$$X = -sin\theta cos\phi, Y = cos\theta, Z = sin\theta sin\phi$$

$$\sigma_{22} = -W\eta/3, \sigma_{33} = \frac{1}{2}(-\sigma_{22}-W), \sigma_{11} = -\sigma_{22}-\sigma_{33}$$

$$\nu_{CSA} = \nu_L\left(\sigma_{11}X^2 + \sigma_{22}Y^2 + \sigma_{33}Z^2\right)\text{[55]} \tag{4.4}$$

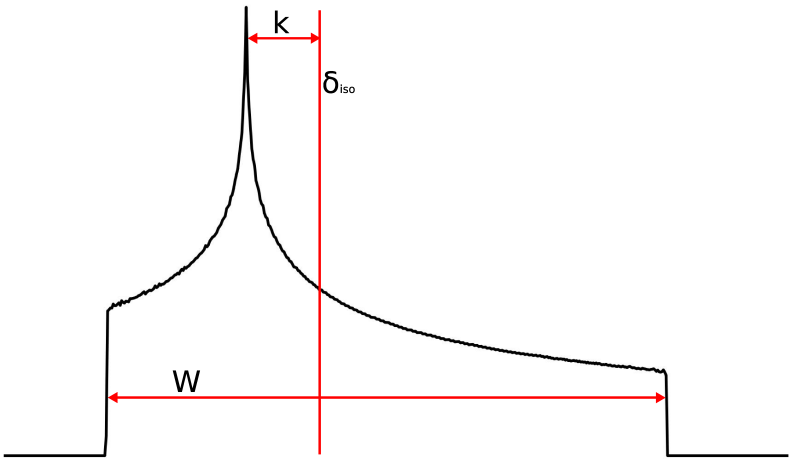

Figure 4.15: Chemical Shift Convention

4.5.5 Combined CSA and Quadrupolar Interaction

Due to the chemical shift tensor and the electric field gradient tensor not generally having the same principal axis system, it is necessary to take account of their relative orientation. The two axis systems are related by the Euler angles α, β, γ, where α is a rotation of the EFG tensor around the Z axis, β is a rotation around the X' axis and γ is a rotation around the Y" axis. These rotations result in the CSA tensor being rotated into the same orientation as the EFG tensor. Due to some of the symmetries breaking down when the two interactions are combined the method to produce this line is a form of sphere stepping. Although the method is not quite as quick as Alderman-Grant interpolation this only results in a factor of 8 slow down for a similar quality spectrum, resulting in a spectrum taking approximately 1s to calculate.

$$cosx = cos\phi sin\theta, cosy = sin\phi sin\theta, cosz = cos\theta$$

$$cos2\phi = \frac{cos^2x - cos^2y}{sin^2\theta}$$

$$\sigma_{22} = -W\eta/3, \sigma_{33} = \frac{1}{2}(-\sigma_{22} - W), \sigma_{11} = -\sigma_{22} - \sigma_{33}$$

$$\nu_{Q1^{st}} = \frac{\nu_Q}{4}(1-2m) \cdot \left(3cos^2\theta - 1 + \eta cos2\phi sin^2\theta\right) \text{[88]}$$

$$A = 24m(m-1) - 4I(I+1) + 9$$

$$B = \frac{1}{4}(6m(m-1) - 2I(I+1) + 3)$$

$$\nu_{Q2^{nd}} = \frac{\nu_Q^2}{12\nu_L}\left[\frac{3}{2}sin^2\theta\left((A+B)cos^2\theta - B\right) - \eta cos2\phi sin^2\theta\left((A+B)sin^2\theta + B\right)\right.$$
$$\left. + \frac{\eta^2}{6}\left(A - (A+4B)cos^2\theta - (A+B)cos^2 2\phi\left(cos^2\theta - 1\right)^2\right)\right] \text{[88]}$$

$$A\phi_1 = cosx \cdot cos\alpha + cosy \cdot sin\alpha$$

$$A\phi_2 = cosy \cdot cos\alpha - cosx \cdot sin\alpha$$

$$CSXA = cos\gamma cos\beta A\phi_1 + sin\gamma A\phi_2 - cos\gamma sin\beta cosz$$

$$CSYA = -sin\gamma cos\beta A\phi_1 + cos\gamma A\phi_2 + sin\gamma sin\beta cosz$$

$$CSZA = sin\beta A\psi_1 + cos\beta cosz$$

$$\nu_{CSA} = \nu_L\left(CSXA\sigma_{11}CSXA + CSYA\sigma_{22}CSYA + CSZA\sigma_{33}CSZA\right) \text{[88]}$$

$$\nu_{CSA,Q} = \nu_{Q1^{st}} + \nu_{Q2^{nd}} + \nu_{CSA} \tag{4.5}$$

Chapter 5

Tin Niobates

Tin niobates have the potential to be a new orange pigment replacing some of the traditional cadmium-based pigments which are becoming subject to more stringent legislation. These pigments have many applications ranging from plastics to artists' pigments through to glazes on ceramics. The new generation of pigments has been successful at replacing most colours with a non-toxic variant. The red and orange range of colours has proven difficult to replace. The tin niobates of interest are sulphur-doped with the pyrochlore structure as shown in figure 5.1. The base form of the tin niobate is a strong yellow colour and the addition of sulphur to the structure results in a strong orange colour. Other advantages of this material are the relative ease in which it can be produced and the high temperature stability it shows.

5.1 Model Compounds

The pyrochlore structure as show in figure 5.1 is constructed of corner sharing octahedra, which are partially occupied by Nb(V) and Sn(IV)[12]. The octahedra

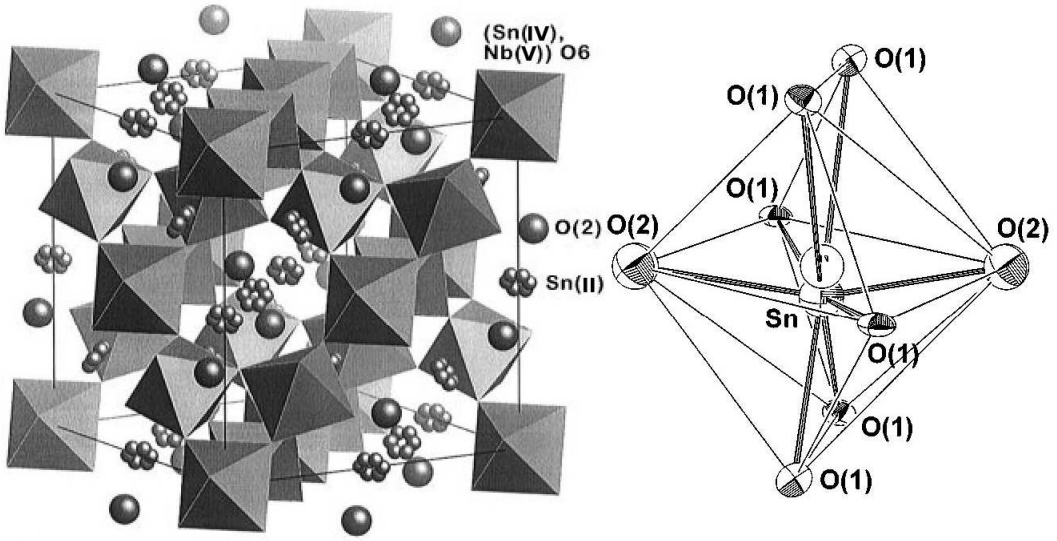

Figure 5.1: Pyrochlore Structure [5]

are arranged in a tetrahedron, this arrangement leaves tunnels in the [110], [101] and [011] directions. At the intersection of the tunnels caverties are formed which are partially occupied by oxygen in the O(2) position and a lone pair of electrons. The tunnels are occupied by tin(II) which are slightly off centre, this results in a distorted Sn(II) site with 6 oxygens from the octahedra in the O(1) position and up to two oxygens in the O(2) position. The partial occupation of the ocahedra and the cavity leads to the chemical formula $Sn_2Nb_2O_7$ being an idealised form of the actual chemical composition. The levels of Sn(II) and Sn(IV) are difficult to determine, being dependent on the exact chemical composition of the final material. For an initial composition of $Sn_2Nb_2O_7$ as reported by Cruz et al.[5] the actual composition as derived from Mössbauer spectroscopy and chemical analysis is $Sn^{II}_{1.18}Nb_{1.68}Sn^{IV}_{0.37}O_6$, so 23.63% of the tin is Sn(IV) in the octahedra. The final composition and the amount of Sn(IV) of the samples produced here can not be assumed to be the same as in the paper by Cruz et al. as the production methods are not exactly the same.

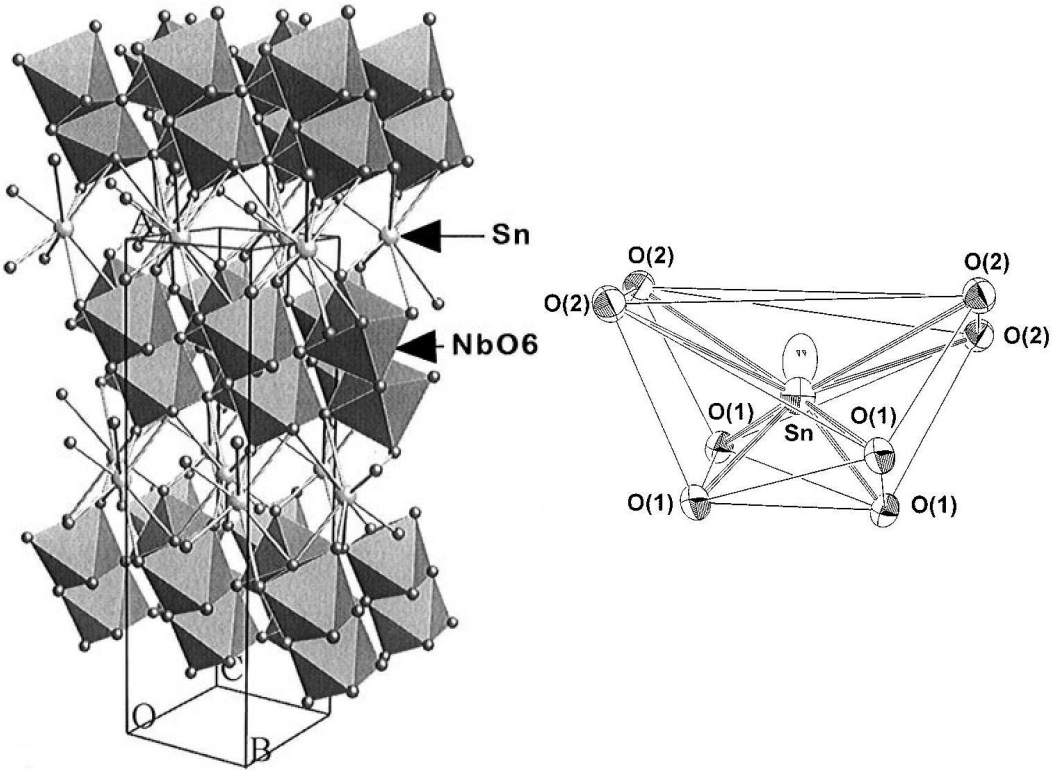

Figure 5.2: Foordite Structure [5]

The foordite ($SnNb_2O_6$) structure (shown in figure 5.2) is somewhat simpler. The structure consists of layers of niobium octahedra which are interlinked by tin. The layers of niobium octahedra are two thick. The layers of niobium octahedra are constructed of pairs of edge-sharing octahedra which are linked together with pairs of corner sharing octahedra. Although there are two forms of linking octahedra they do not seem to result in chemically distinct niobium sites.

The ^{93}Nb NMR spectra of pyrochlore and foordite forms of tin tungstate are shown in figures 5.3 and 5.4 respectively. The model compounds are being studied to allow tracking of the conversion between the two phases of tin niobate. The spectra of the two compounds are significantly different with the pyrochlore showing no structure in the line shape. The pyrochlore spectrum narrows slightly

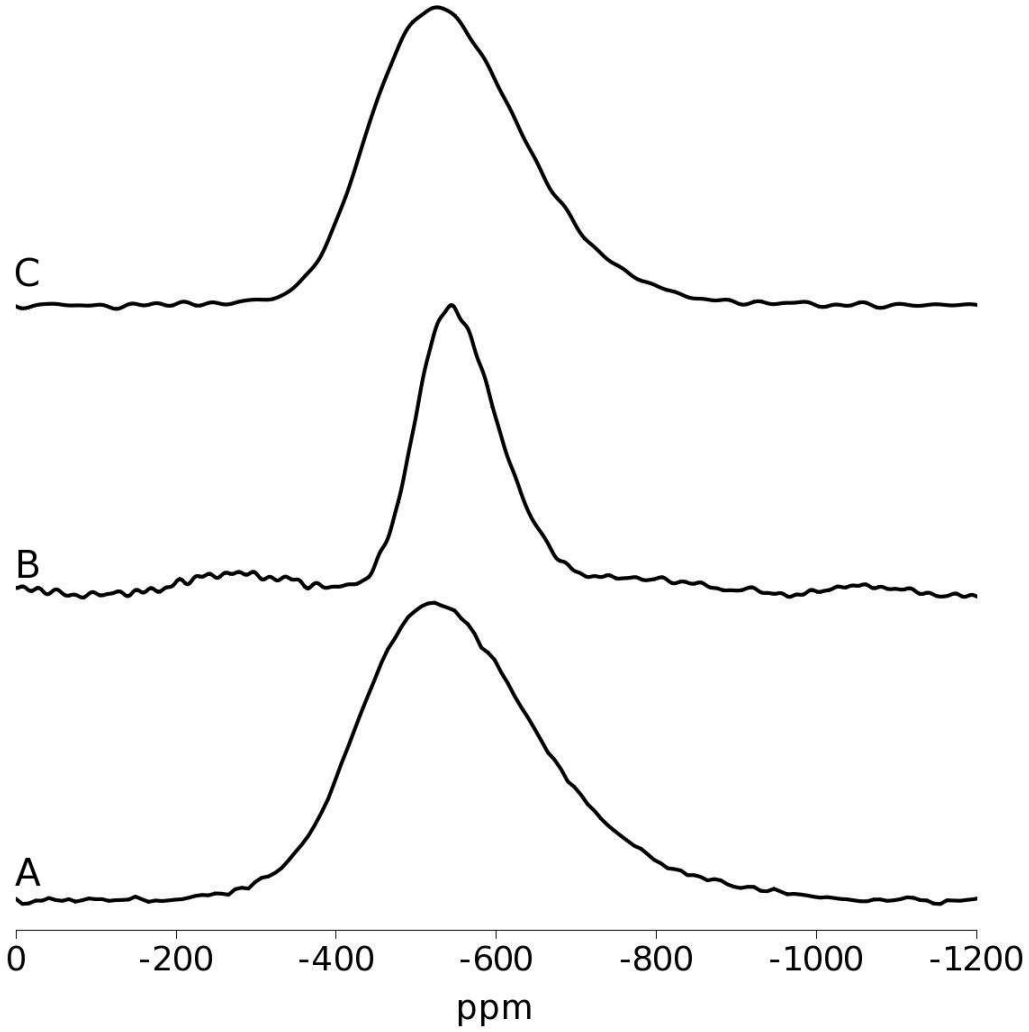

Figure 5.3: ^{93}Nb NMR spectra of pyrochlore tin niobates ($Sn_2Nb_2O_7$). A:-Static at 14.1T, B:-MAS at 14.1T and C:-Static at 18.8T

at higher field, but not to 75% of the width at 14.1T. As the spectra are static the relatively small amount of narrowing by increasing field implies that there is a significant chemical shift anisotropy contribution to the line width in addition to second-order quadrupolar broadening. The lack of features is due to a distribution in one or more of the interaction parameters due to some atomic disorder in the material which is expected due to the partial occupancy of the octahedra. The

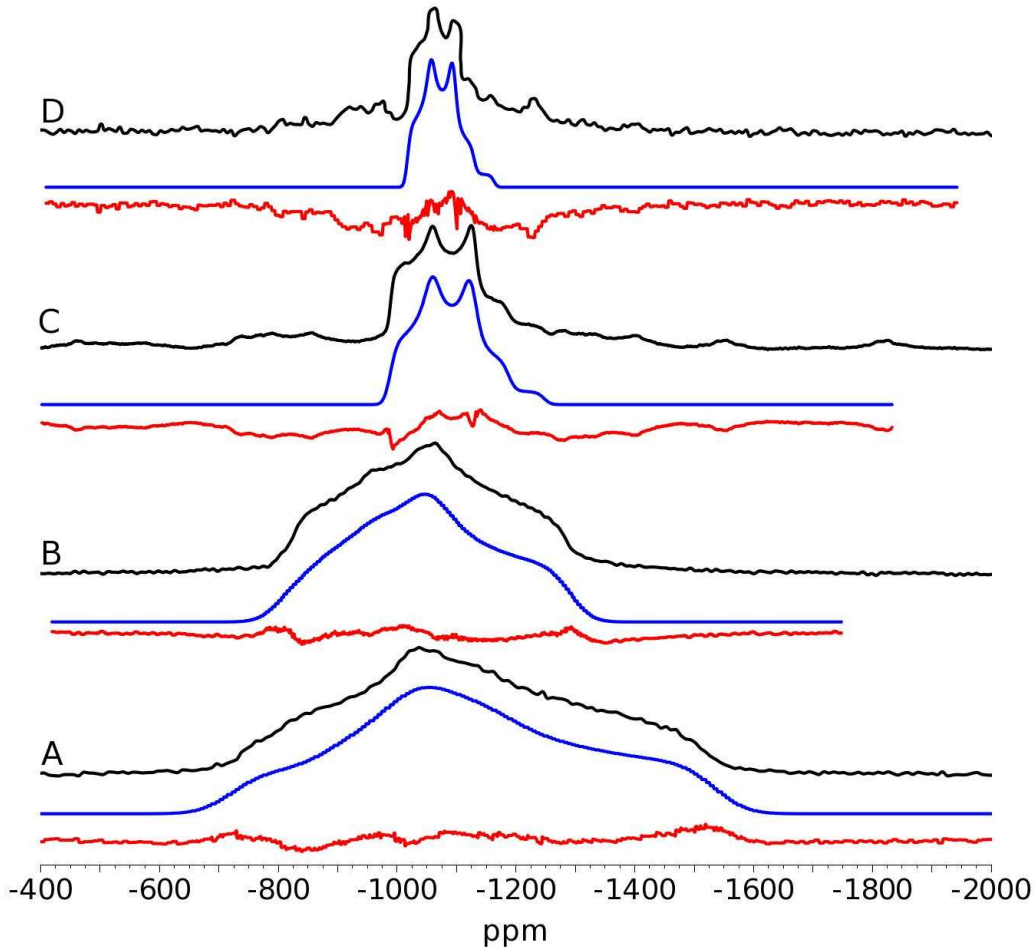

Figure 5.4: ^{93}Nb NMR spectra and simulation of foordite tin niobates ($SnNb_2O_6$). A:-Static at 14.1T, B:-Static at 18.8T, C:-MAS at 14.1T and D:-MAS at 18.8T

distributions in interaction parameters and the lack of features in the line shape mean that fitting the spectra with a reasonable level of confidence is not possible. The foordite structure as shown in figure 5.2 shows complete occupancy of the niobium octahedra so has higher structural ordering leading to the spectra showing sharp features. At an increased magnetic field the spectrum narrows implying it is dominated by the second-order quadrupolar interaction. The spectra along with simulations are shown in figure 5.4, and the simulation parameters are shown in table 5.1.

Span	274±3ppm
Skew	0.20±0.2
C_Q	40.1±0.5
η_Q	0.48±0.2
Shift	-1014±5ppm
Broadening	7000±250Hz
α	90±2°
β	90±2°
γ	157±2°

Table 5.1: Simulation Parameters for Foordite in figure 5.4.

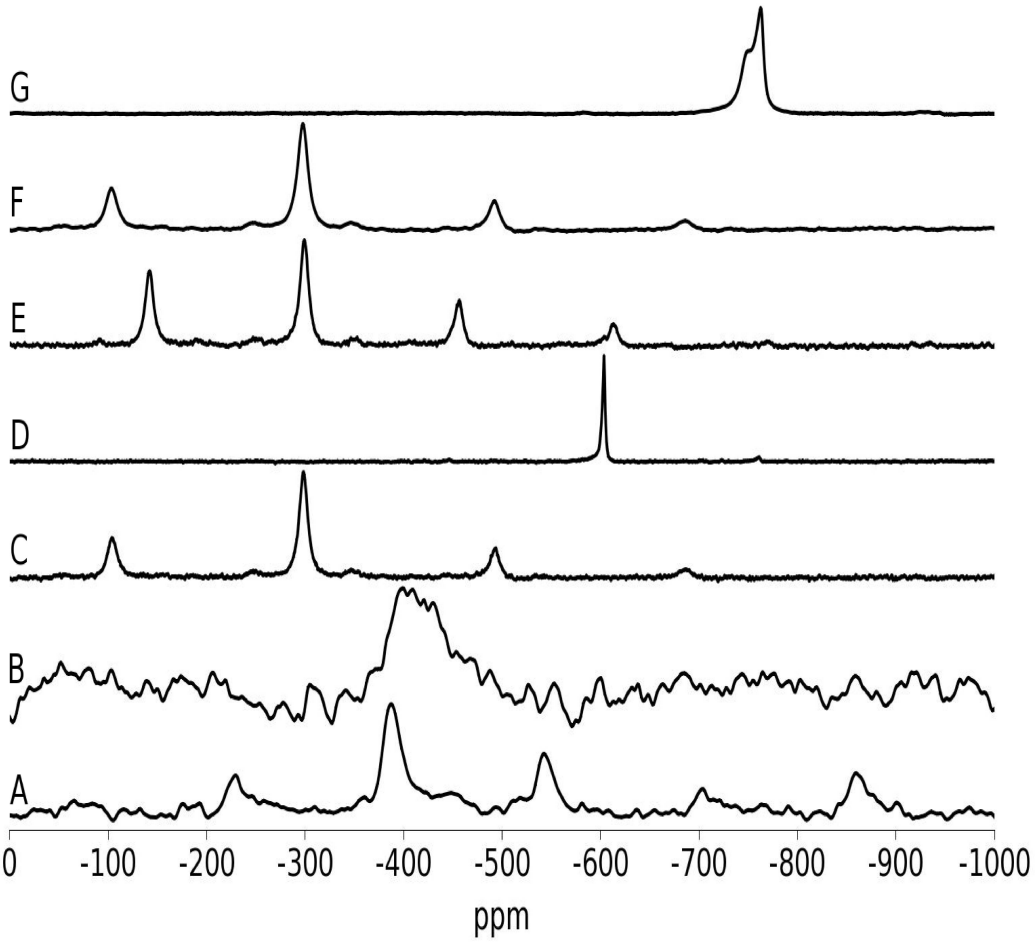

Figure 5.5: ^{119}Sn NMR spectra of model tin compounds. A:- $SnNb_2O_6$, B:- $Sn_2Nb_2O_7$, C:- SnO, D:- SnO_2, E:-SnSe, F:- SnS, G:- SnS_2

As part of the tin study a series of model tin compounds were studied. As with the niobium spectra, the tin spectra show a marked difference between the two different phases of tin niobate. The foordite with the fully occupied sites has a narrow line and the pyrochlore with partial occupancy has a much broader line shape. Unfortunately the shift of the ^{119}Sn lines is similar effectively preventing a determination of the relative amounts of foordite and pyrochlore tin niobate. The ^{119}Sn shifts and line widths for the model compounds are shown in table 5.2. Referring back to these model compounds the tin spectra of the pigments can be used to determine the levels of various impurities. Both the SnS and SnSe samples show J-coupling between ^{119}Sn and ^{117}Sn resulting in a splitting of the central peak into three peaks, the centre of which is significantly the strongest. The SnS_2 sample shows a splitting of the tin site. As the structure is hexagonal the tin sites are chemically equivalent. Spin-spin coupling is obviously not the cause of the second site. Similar secondary sites have been observed before[47] and it has been proposed that the secondary signal is due to structural effects. Exactly what the "Structural Effects" are has not been published.

Compound	**Shift (ppm)**	**Line Width (Hz)**
$SnNb_2O_6$	-387±2	900±50
$Sn_2Nb_2O_7$	-403±10	2400±200
SnO	-296.9±0.5	385±10
SnO_2	-602.9±0.5	132±5
SnSe	-299.0±0.5	395±5
SnS	297.7±0.5	526±5
SnS_2	-762.3±1.0	804±20

Table 5.2: ^{119}Sn NMR shift and line width of model compounds.

5.2 Results and Analysis

As seen from the model compounds the niobium spectra are particularly useful at determining whether the tin niobate has the pyrochlore or foordite structure. There is an obvious conversion between foordite and pyrochlore which can be easily seen when comparing the ^{93}Nb static spectra in figure 5.6 to the model compounds. The foordite phase seems to have completely converted to the pyrochlore by 900°C and the proportion of the two phases is shown in table 5.3. The selenium-doped samples seem to have either a shifted foordite phase which is partially washed away during the washing using ammonia poly-sulphide or a niobium-containing impurity which is not soluble in HCl. A seperate niobium containing phase although not present in the XRD results (as summarised in table 5.4) is still a possibility. The seperate niobium containing phase is likely to be amorphous, so it's XRD resonance will be very broad and so difficult to detect. As niobium has such a large quadrupole moment it is very sensitive to changes in the symmetry of the site. The line width would then be expected to increase significantly if the selenium was distorting the niobium sites. The line width of the selenium-doped samples in comparison to the sulphur-doped samples is very similar and so it can be assumed that the selenium and sulphur do not sit in a site close to the niobium.

Firing Temperature °C	**Pyrochlore ±5%**
600	>95
700	86
800	71
900	<5

Table 5.3: Percentage of tin niobate which is pyrochlore. All spectra shown are of the treated sulphur-doped samples

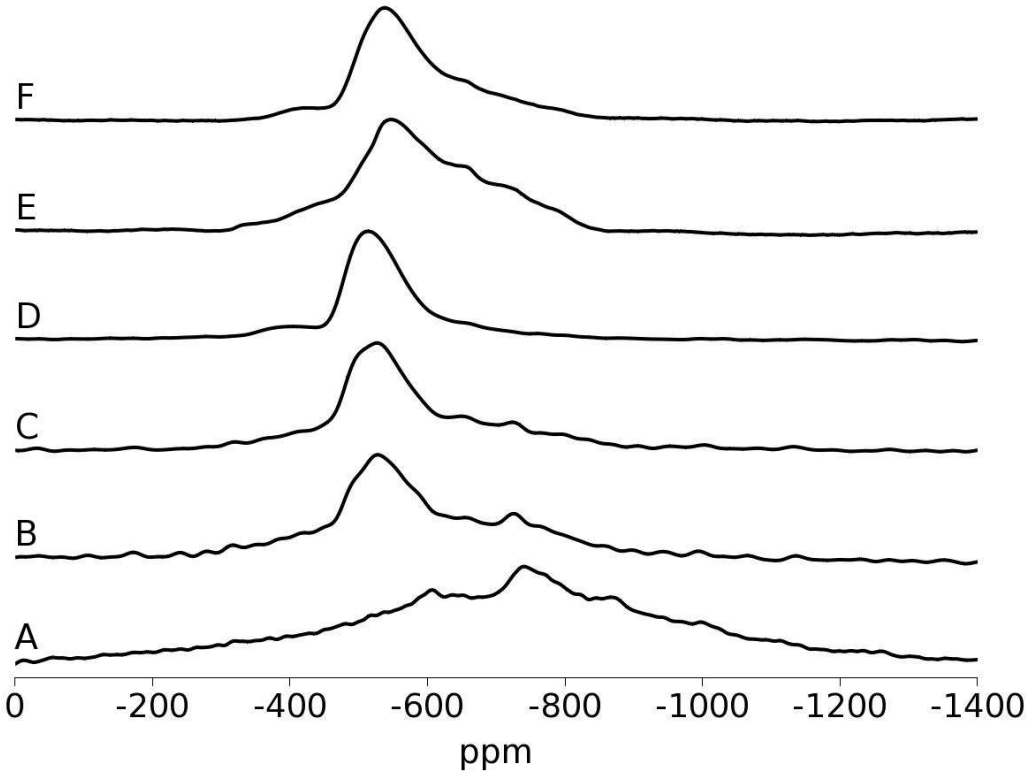

Figure 5.6: ^{93}Nb static NMR spectra at 14.1T of a temperature series of treated tin niobates. A-D:-Sulphur-doped tin niobates fired at A:-600°C, B:-700°C, C:-800°C, D:-900°C and E,F are sulphur and selenium-doped, fired at 900°C and treated with HCl and ammonia polysulphide respectively.

Sample	**Phases**				
	Nb_2O_5	SnO_2	SnS	Sn	$SnS_{0.5}Se_{0.5}$
F600	medium	medium	medium	medium	NA
F700	medium	medium	medium	medium	NA
F800	ND	weak	medium	ND	NA
F900	ND	ND	weak	ND	NA
F900Se	ND	ND	ND	ND	weak

Table 5.4: XRD diffraction strength information of tin niobates after firing. Supplied by Johnson Matthey. ND - Not Detected, NA - Not Applicable.

When the tin niobates are produced they are a bright orange with a slight grey tinge to them. After ball milling the pigment turns a grey colour due to the tin sulphide spreading out over the particles. It was proposed that the ball milling

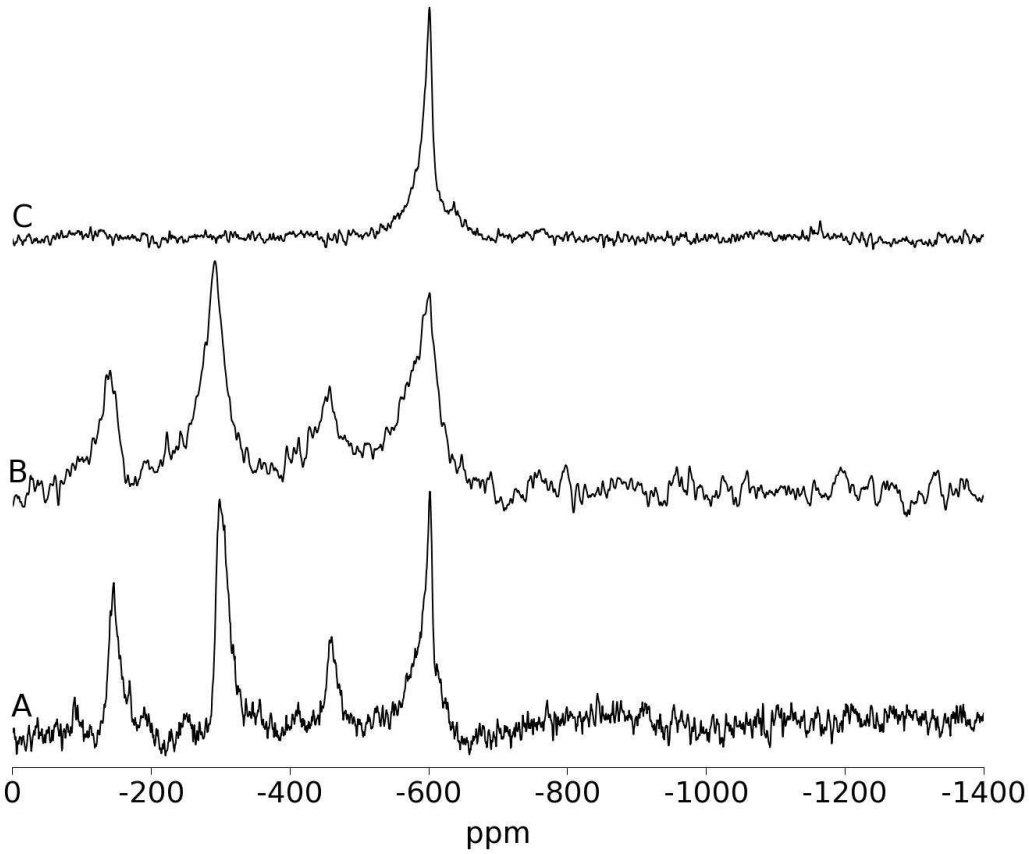

Figure 5.7: ^{119}Sn MAS NMR spectra of $Sn_2Nb_2O_{6.3}S_{0.7}$ at 4.7T A:-after firing, B:- after ball milling and C:- after treating in HCl

could remove some of the tin sulphide. From the ^{119}Sn MAS NMR spectra shown in figure 5.7 ball milling has the effect of broadening the spectra slightly. The broadening is due to the tin sulphide being spread out in a thin layer over the particles of pigments rather than being a bulk tin sulphide so surface effects are much larger.

The effect of washing the samples in HCl is dramatic, since it results in almost complete removal of tin sulphide and tin oxide impurities as shown in figure 5.7. The line shifts for the milled and treated pyrochlore are similar, however the

milled sample is significantly wider. During the milling process the particles reduce in size and the tin sulphide is spread over the surface of the pigment particles. The reduction in size results in more surface effects in each particle and thus more disorder in the material. The increased level of disorder in the pigment shows as an increase in line width.

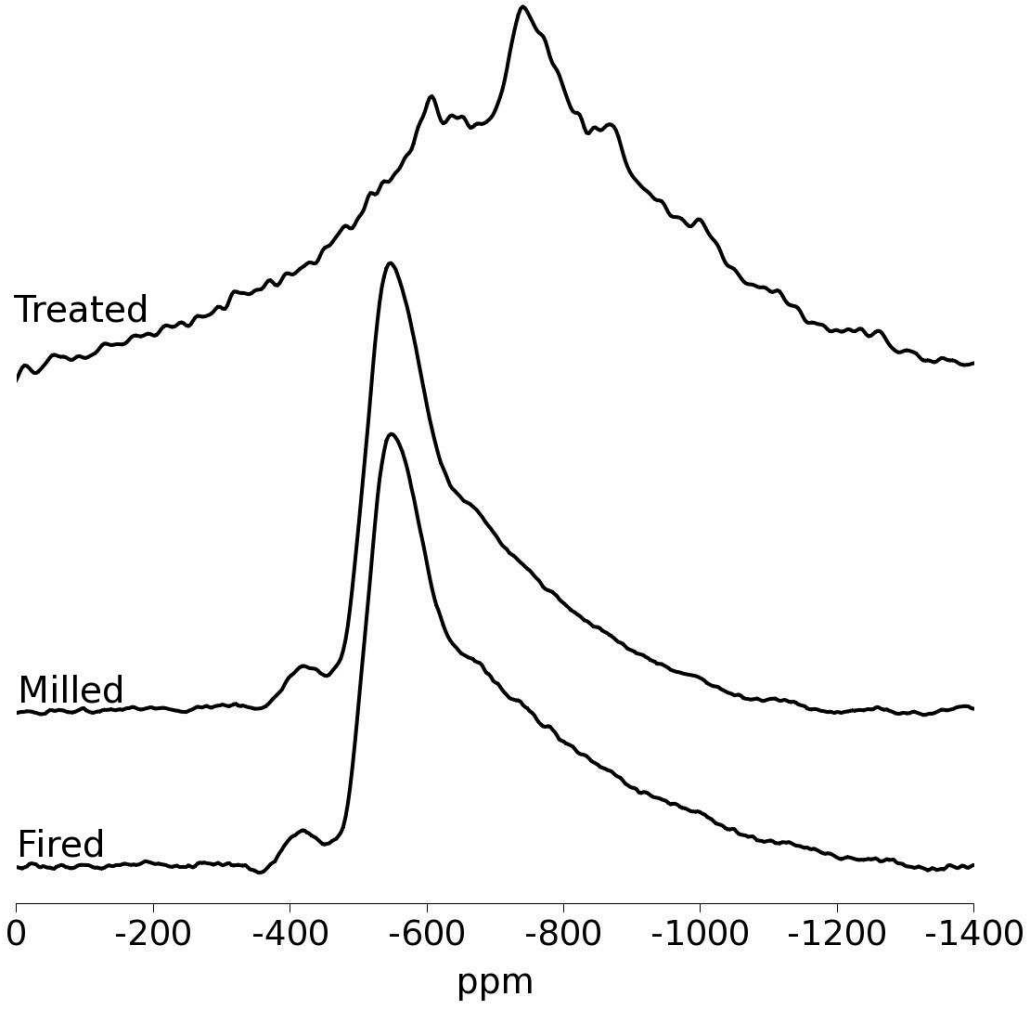

Figure 5.8: ^{93}Nb MAS NMR spectra, acquired at 14.1T, of sulphur-doped tin niobates fired at 600°C and at various processing stages.

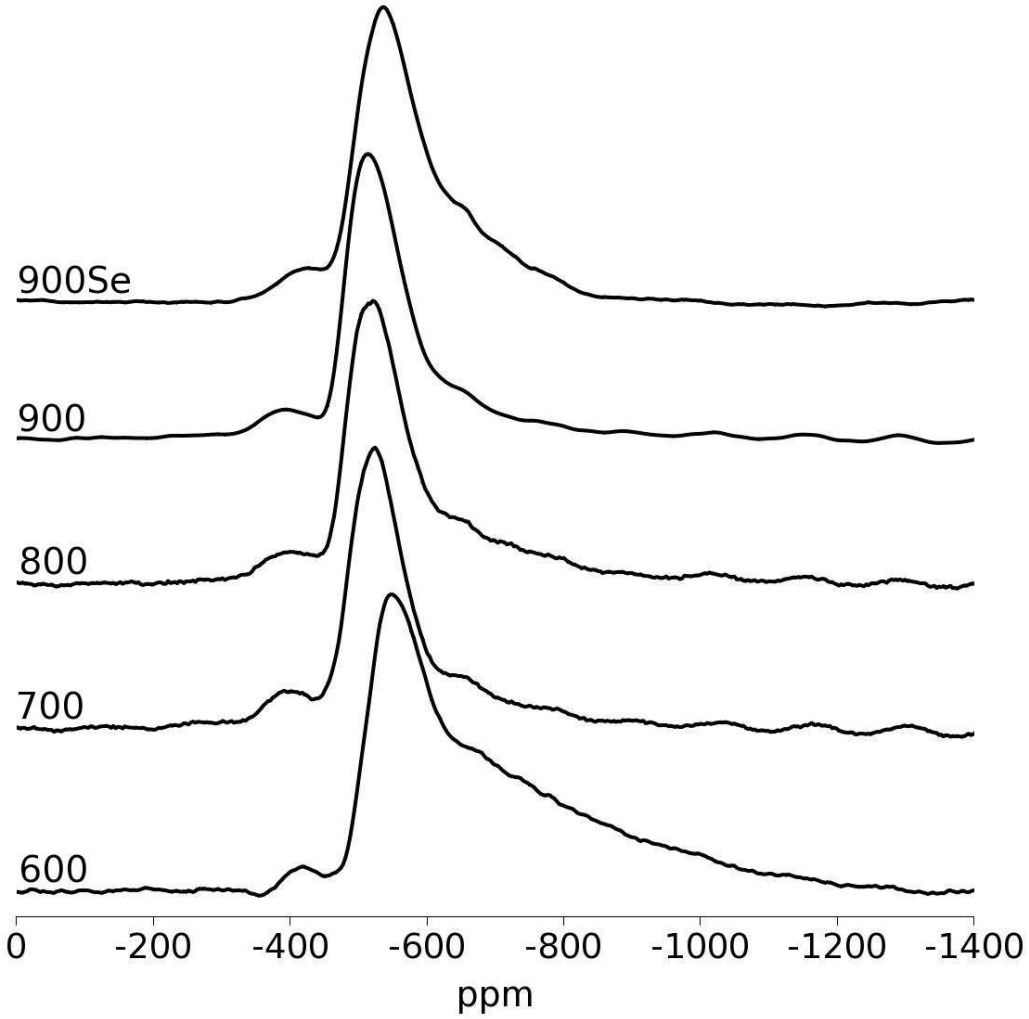

Figure 5.9: ^{93}Nb MAS NMR spectra acquired at 14.1T of tin niobates. Firing temperatures are shown in °C and the sample labelled 900Se is a sulphur and selenium doped tin niobate

Figure 5.8 shows that the washing has the effect of removing the Nb_2O_5 which has a similar shift and line shape to the pyrochlore. Figure 5.8 shows very similar lines for both the fired and the milled versions of the material. Figures 5.9 and 5.10 show the fired and milled versions of the pigments respectively. The differences between the two are very small and as such show that the milling process does not affect the niobium site in the material. The change in the niobium site

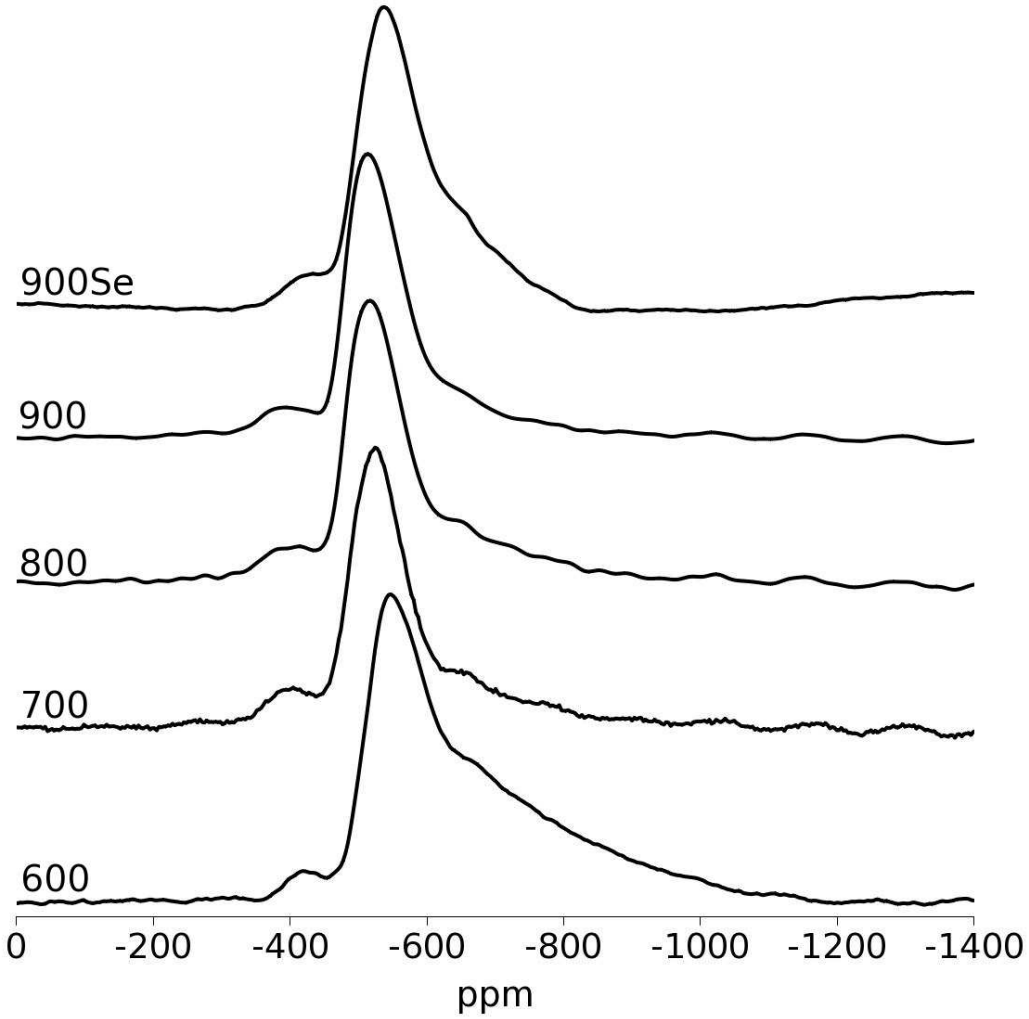

Figure 5.10: ^{93}Nb MAS NMR spectra acquired at 14.1T of Tin Niobates after milling. Firing temperatures are shown in °C and the sample labelled 900Se is a sulphur and selenium doped tin niobate

as temperature increases shows a shift from a mixture of foordite and niobium oxide (as shown by figure 5.8) to a mixture of pyrochlore and niobium oxide after heating to 900°C. The production of Nb_2O_5 is expected during the conversion from foordite to pyrochlore as the phase change results in an excess of niobium and oxygen in the ratio of 2:5. The peak at approximately -400ppm is a spinning side band of the foordite/pyrochlore/niobium oxide mixture.

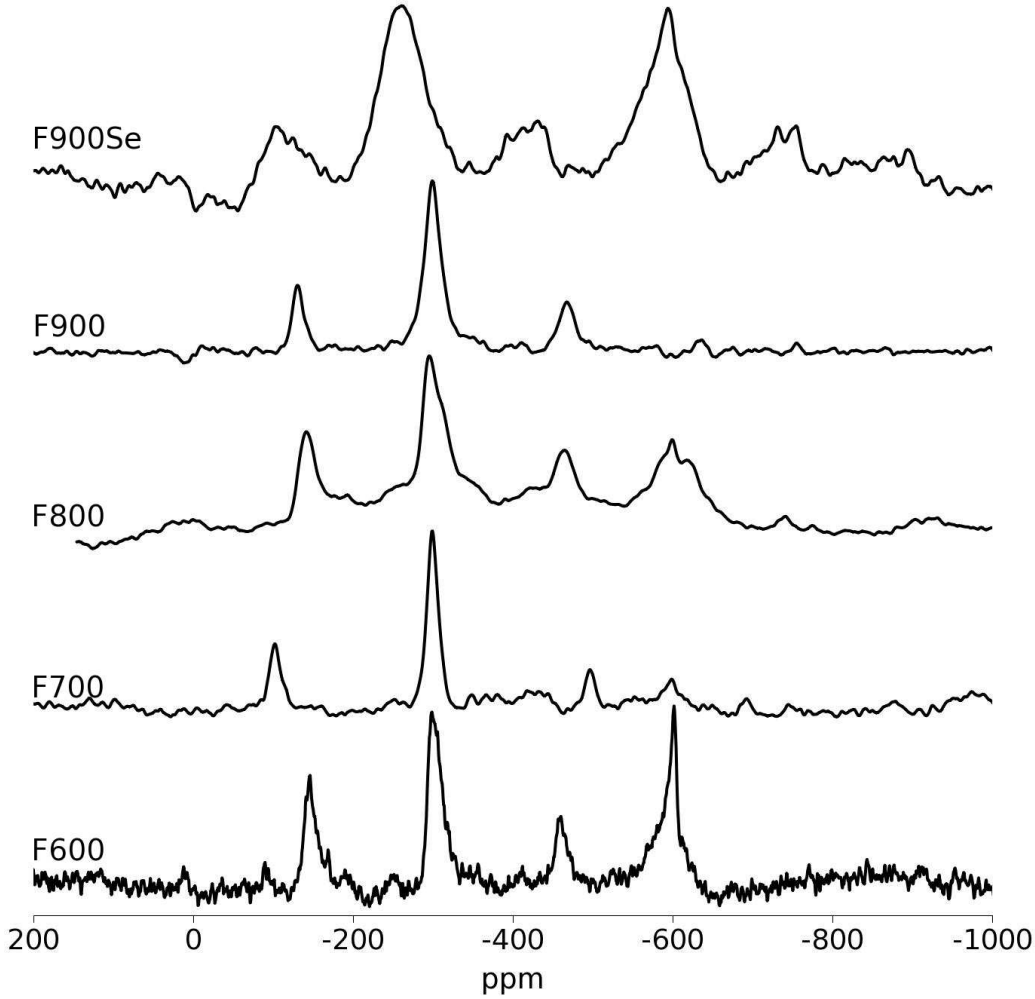

Figure 5.11: ^{119}Sn MAS NMR spectra of tin niobates at 4.7T. The samples are from the fired temperature series with the firing temperature given in the name.

Figure 5.11 shows a ^{119}Sn temperature series. The peaks at approximately -300ppm are in the region of the SnS and SnO_2 signals. As it is known that significant quantities of tin sulphide are produced it is a reasonable assumption that most of the signal is from tin sulphide. The peaks at approximately -600ppm are due to the doped tin niobate. Ignoring the sample produced at 700°C, the relative intensity of the doped tin niobate to the impurities drops as firing temperature increases as also shown in figure 5.12. The spectrum of $Sn_2Nb_2O_{6.3}S_{0.46}Se_{0.24}$

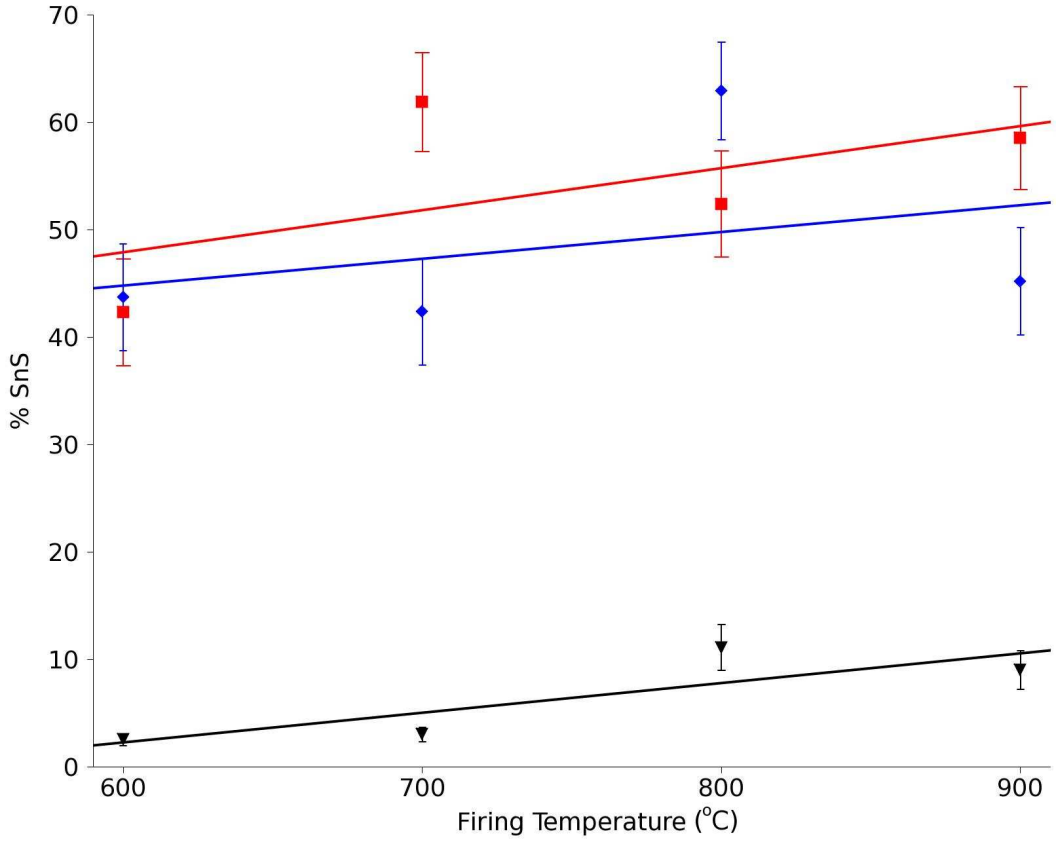

Figure 5.12: Levels of SnS detected in tin niobates corrected for relaxation effects. Red is fired, Blue milled and Black treated.

(figure 5.11 F900Se) is broader than the sulphur-doped tin niobates (figure 5.11 F600, F700, F800, F900). For the tin niobate line (−600ppm) the broadening is due to the selenium being included into the structure causing distortions in the structure and thus some atomic and structural disorder. The line associated with SnS is also broader due to the impurities including SnSe which has a similar, but not identical shift to SnS and SnO_2, thus two lines overlapping results in a broader signal. During the measurements of the SnS and tin niobate levels it was determined that the amounts of tin sulphide that were being reported was too large compared to the amount of tin niobate. As the spectra were acquired using an echo it was decided to try to measure the T_2 of the samples. It was found that

the T_2 of the tin niobate was short in comparison to the delay between the pulses due to the signal vanishing with a τ delay of two rotor periods when spinning at 12kHz and the T_2 of the tin sulphide was long compared to the delay between the pulses. To compensate for this a series of samples were run with known SnS to $Sn_2Nb_2O_7$ ratios and the discrepancy between the measured and the known ratios were measured. The results are shown in table 5.5 and a correction factor of 2.2±0.1 was calculated. A more accurate correction factor could have been calculated if the T_2 of the tin niobate was measured, however a signal was difficult to obtain without the sample spinning and the signal had decayed completely after two rotor periods when spinning at 12kHz.

wt% SnS	**Predicted Molar Ratio SnS:$Sn_2Nb_2O_7$**	**Measured Molar Ratio SnS:$Sn_2Nb_2O_7$**	**Correction Factor**
10	0.39:2	0.89±0.17:2	2.3±0.40
20	0.89:2	1.90±0.30:2	2.1±0.35
30	1.52:2	3.53±0.71:2	2.3±0.45

Table 5.5: Error correction of SnS Levels

Figure 5.13 shows a composite spectrum of tin metal and the normal shift range of tin for $Sn_2Nb_2O_{6.3}S_{0.7}$ fired at 700°C. The spectrum was obtained by acquiring a spectrum for the two regions separately, as the regions are sufficiently separate that it would be difficult to excite both regions. A spectrum of the tin metal region was obtained for all of the samples. The spectra were all normalised using the amount of sample in the rotor and the amount of scans. These results are represented in figure 5.14. The figure shows the relative amounts of tin metal per gram of sample if the amount of SnS was completely removed. This has been calculated from the signal per gram of the standard sample then combining it with the corrected levels of tin niobate in the material. The levels of tin metal drop off as the temperature of firing increases. There is little difference between the fired

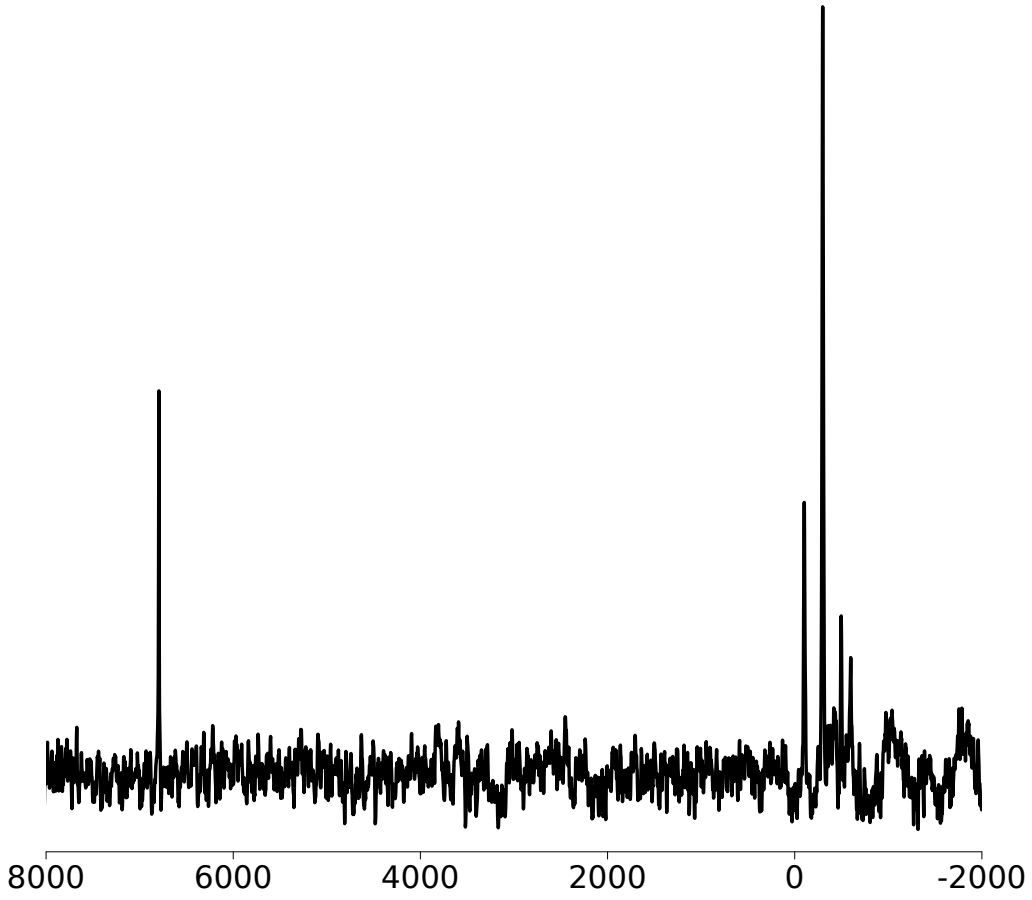

Figure 5.13: A composite ^{119}Sn MAS NMR spectrum of tin metal and normal shift ranges for $Sn_2Nb_2O_{6.3}S_{0.7}$ fired at 700°C.

and the milled samples, and an increase in the levels of tin metal in the treated samples. This is the opposite effect to what was expected, it can be explained by the washing in HCl not removing the tin metal and removing some of the tin niobate during the pouring off of the HCl and water.

Firing the sample at 900°C produces almost complete conversion from the foordite to the pyrochlore phase of the tin niobate. The washing of the samples in HCl reduces the levels of impurities to almost zero apart from tin metal which

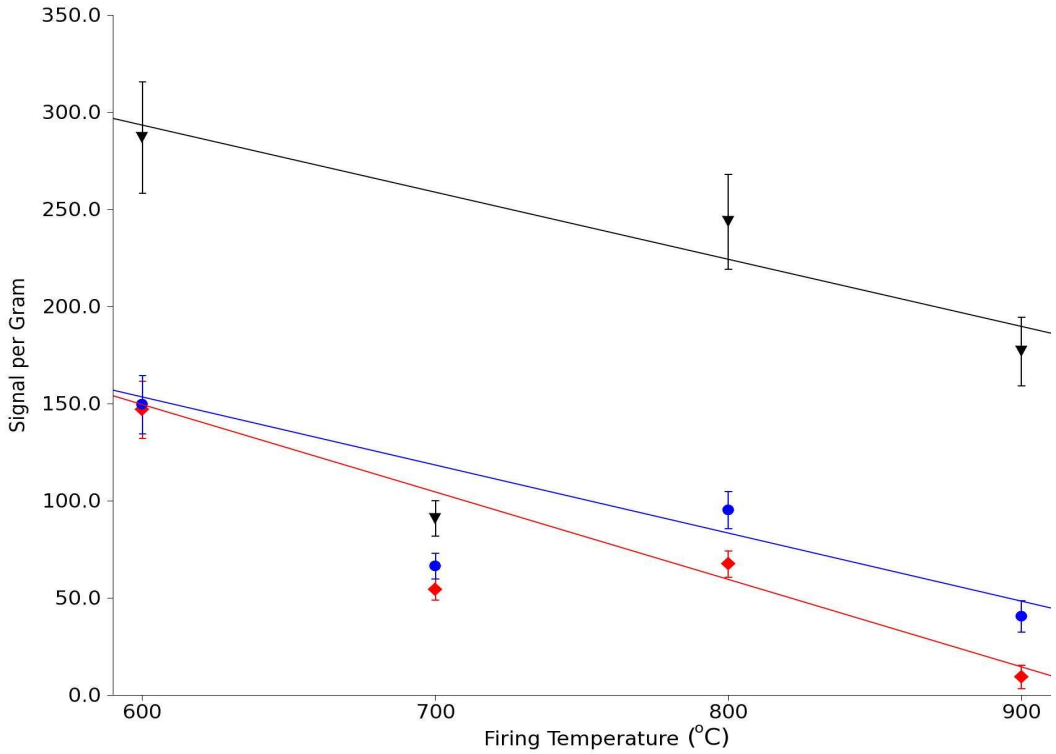

Figure 5.14: Levels of tin metal after removal of SnS. Red:- Fired, Blue:- Milled and Black:- Treated

increases in proportion to the rest of the sample probably due to preferential losses of the tin niobate during the pouring off of the excess HCl and water.

It is evident from the XRD data and the tin NMR spectra that as the firing temperature increases the amount of SnS increases in the sample and the amount of tin metal decreases. This implies that as the material changes from foordite to pyrochlore sulphur comes out of the structure reacting with the tin metal, increasing the levels of SnS but decreasing the levels of tin metal. Selenium was added to one of the samples as it acts in a very similar way to sulphur, but is larger so would distort the structure allowing determination of the sites in which the sulphur sits. The niobium spectra (figures 5.9 and 5.10) show no increase in width with the addition of selenium. As niobium has a large quadrupole moment it

is very sensitive to the symmetry of a site. If selenium was close to the niobium a significant increase in line width would be expected. As an increase in line width is not observed the sulphur and selenium are not closely associated with the niobium. Looking at the pyrochlore phase tin niobate (figure 5.1), it can be seen that not to affect the niobium the sulphur would have to be taking up the O(2) position in the structure.

5.3 Conclusion

Although sulphur doped tin niobates don't produce red pigments they do produce a strongly coloured orange pigment. The firing process at 900°C produces complete conversion from the foordite to the pyrochlore form of tin niobate. During the manufacture of the pigments, significant amounts of tin sulphide are produced which are washed off by treating with HCl. A study into the saturation level of sulphur in the system would allow a design of the manufacture process to either remove all tin sulphide produced or minimise the levels. A study into the amount of firing time would also be of interest to discover whether a longer firing period would result in a larger inclusion of sulphur in the system. The selenium included in the structure allowed the determination that the sulphur and selenium sit in the O(2) position in the structure as shown in figure 5.1.

Chapter 6

Copper Indium Sulphur Selenide doped Zinc Selenides

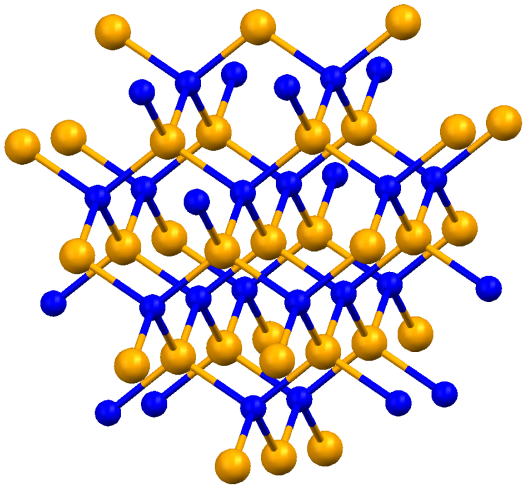

Figure 6.1: ZnSe Structure[6]. Blue is Zn and orange is Se.

During the F-Colours project it was noted that with the inclusion of selenium and sulphur into various materials there tended to be a shift in the band gap towards longer wave lengths[13]. This led to the idea of studying a system which has many NMR accessible nuclei, relatively simple known structures and exhibits

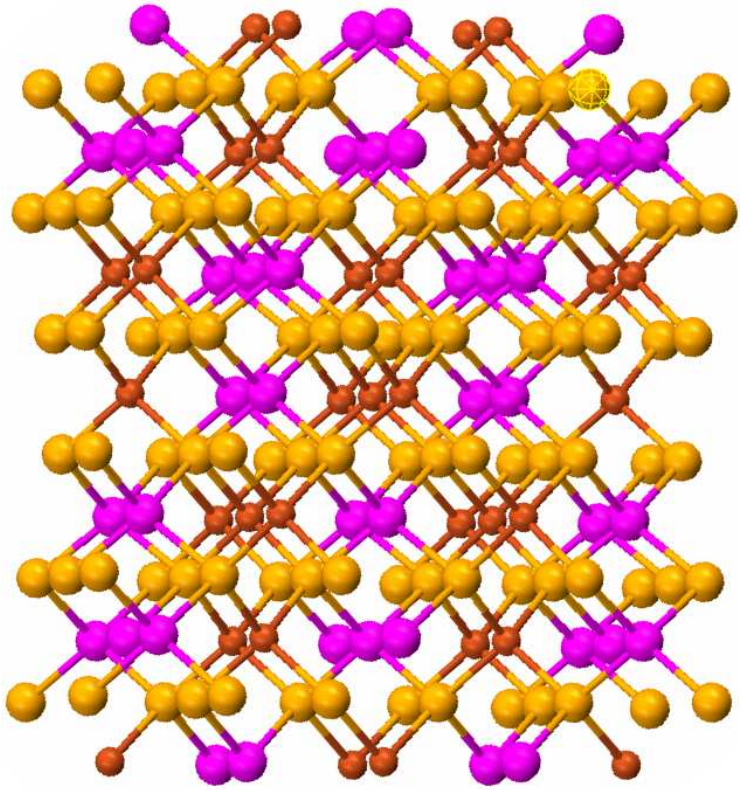

Figure 6.2: $CuInSe_2$ Structure[7]. Red is Cu, pink is In and orange is Se.

the shift towards longer wave lengths with the addition of sulphur and selenium. The system being studied is a copper indium sulphur selenide doped zinc selenide. Zinc selenide is a bright yellow, and with the addition of the dopant the colour shifts to a strong orange. The base material which is the zinc selenide has a simple cubic structure as shown in figure 6.1 and is known as Stilleite. Each zinc is bonded to 4 selenium atoms and vice-versa. Copper indium selenide is a tetragonal structure and is shown in figure 6.2. The copper indium selenide is made up of planes of alternating columns of indium and copper, with selenium in alternate planes. The structures of $CuInS_2$ and $CuInSe_2$ are the same[89], so although no crystal structures for CuInSSe have been published the structure is probably similar to $CuInSe_2$ with a 50% occupancy for the selenium site with selenium and sulphur.

6.1 Model Compounds

Material	Shift (ppm)	No. Acquisition	Recycle Delay (s)	Total Time (Hours)
K_2SeO_4	-206.4	96	600	16
Na_2SeO_4	-210.9	1784	5	2.5
SeO_2	340.3	3762	5	5.2
CdSe	-1743	8	600	1.3
ZnSe	-1622	12	600	2
$NbSe_2$	2495	33568	0.1	1

Table 6.1: Shifts of model compounds

^{77}Se is relatively uncommon in solid state NMR studies, especially in inorganic systems where protons can not be used to increase the amount of signal via cross polarisation. Due to the lack of information on structural influences on ^{77}Se NMR parameters a series of model compounds was studied to explore the experimental conditions which are required to get a signal and to determine which systems can be studied. Figures 6.3, 6.4 and 6.5 show data from a series of model compounds. They have been split into 3 separate plots due to their large shift ranges shown in table 6.1. As apparent from these samples selenium has a particularly large shift range of at least 4200 ppm. Most of the spectra show a single sharp peak implying that the chemical shift anisotropy is relatively small and has been spun out completely by MAS. The niobium selenide however shows a large spinning side band manifold implying that the CSA is relatively large. The other key piece of information gained is that obtaining spectra for even model materials can take large amounts of time. At 8.45 T using a 4 mm varian rotor it took approximately 2 hours with a 10 minute pulse delay to get a signal to noise ratio of 15:1 for a pure zinc selenide sample. This means that although it would be

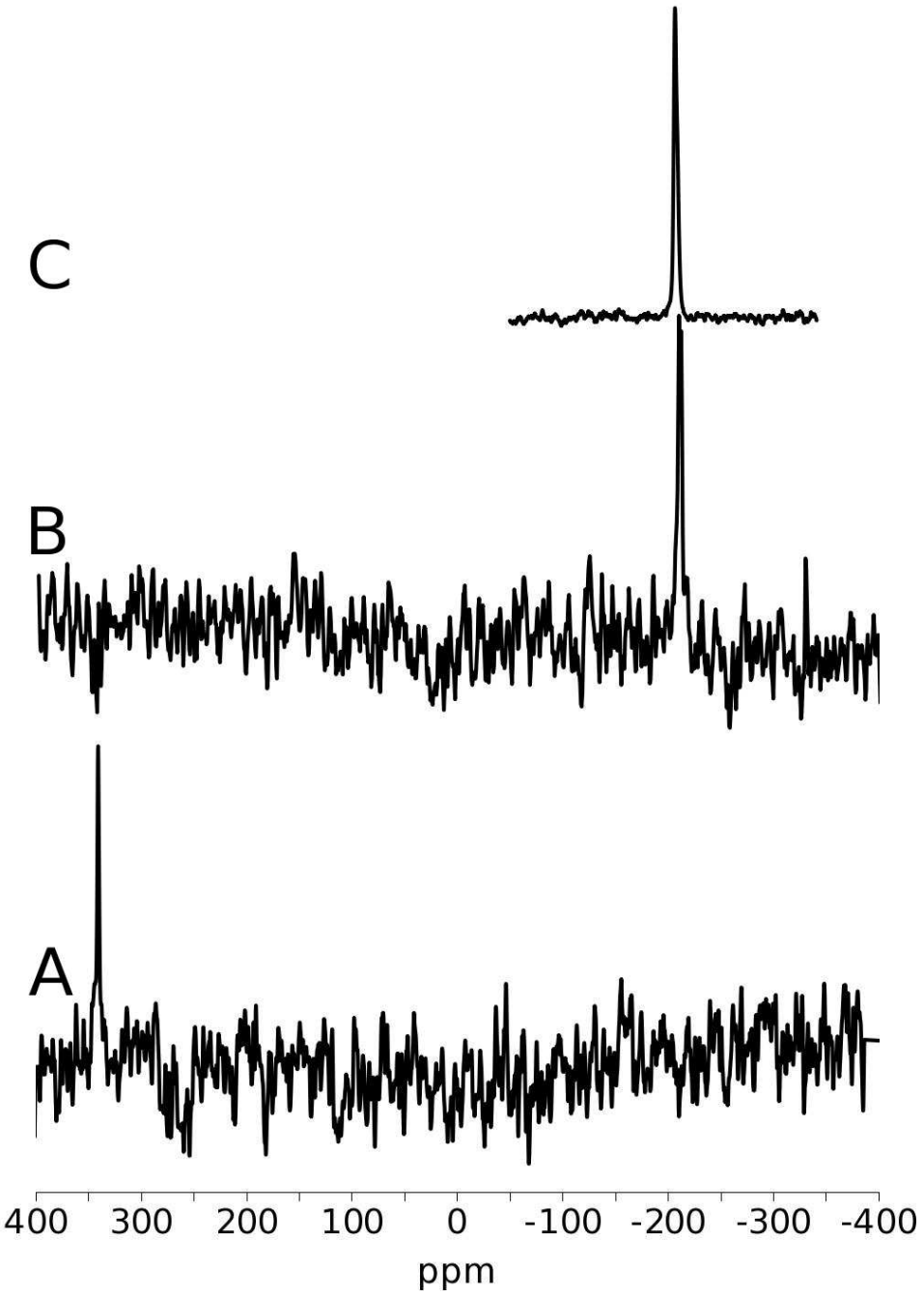

Figure 6.3: ^{77}Se MAS NMR at 8.45 T of A:-SeO_2, B:-Na_2SeO_4 and C:-K_2SeO_4

ideal to get a signal from the copper indium selenide it would take an excessively long time, even if the signal was narrow. Despite trying, signals from either the CuInSSe or the $CuInSe_2$ samples were not obtained. As the quadrupolar nuclei in

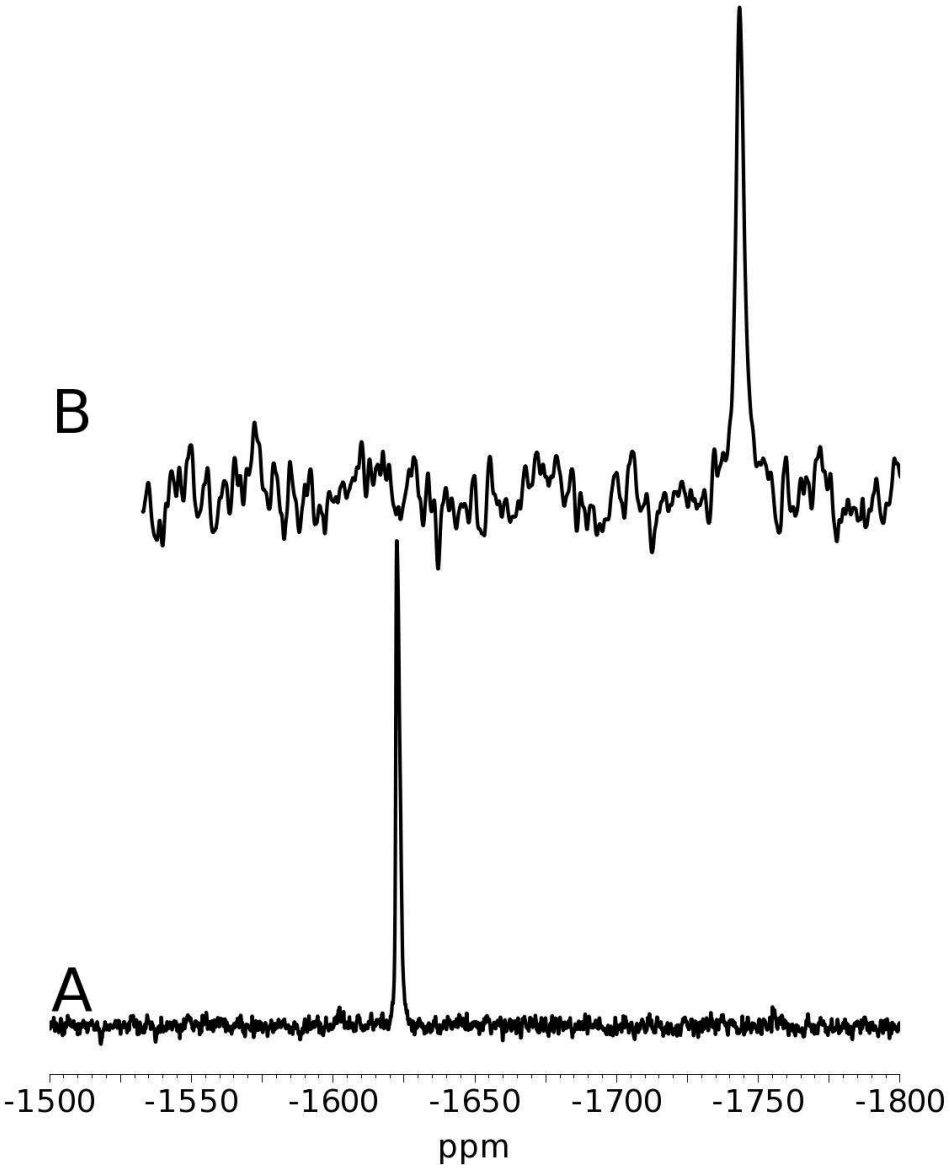

Figure 6.4: ^{77}Se MAS NMR at 8.45 T of A:-ZnSe and B:-CdSe

the material should form an effective relaxation mechanism it must be assumed that the line widths were too broad to measure.

The copper NMR data for $CuInSe_2$ are shown in figures 6.6 and 6.7 and the copper data for the CuInSSe are shown in figure 6.8. The extra line in the 18.8 T data is from the copper coil. As the coil is metallic copper the resonance from

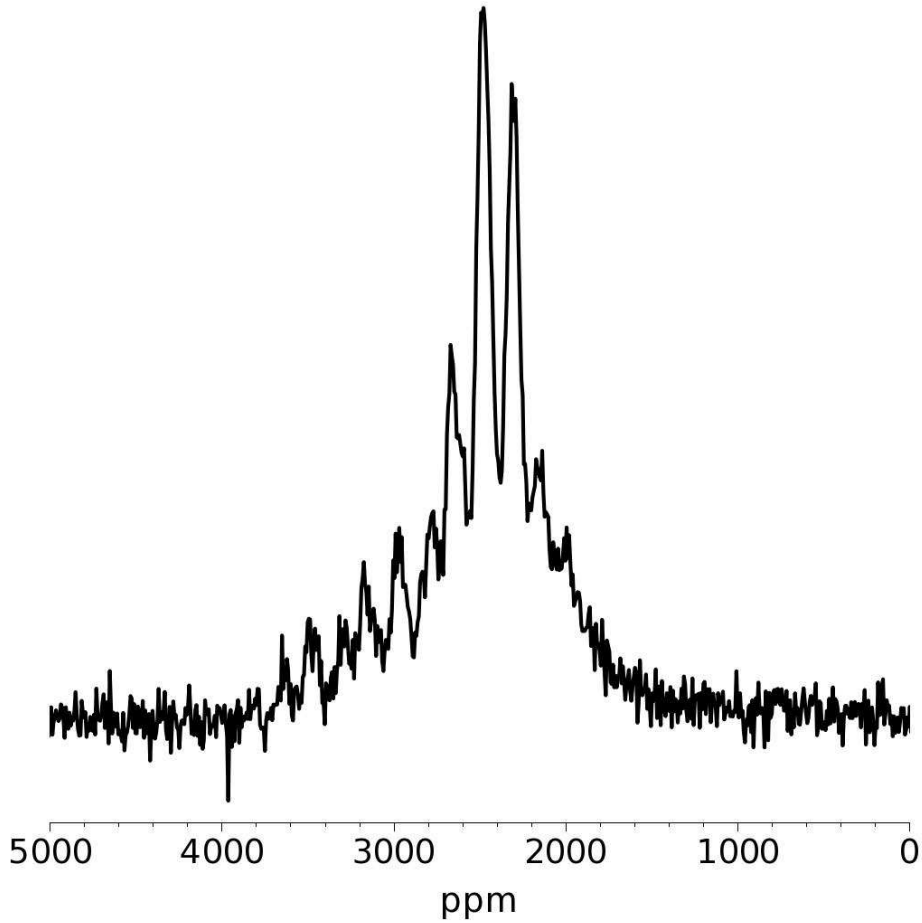

Figure 6.5: ^{77}Se MAS NMR at 8.45 T of $NbSe_2$

it is Knight shifted away by 0.2394%[90] from the central resonance and, as it is physically separated from the sample, is out of phase. The different features of the lines can be easily assigned to different types of interactions due to the way they change with field. The central line stays the same width (in ppm) with increasing magnetic field which means it scales with field. The scaling with field is indicative of chemical shielding anisotropy. The shape of the central line is also typical of this interaction. For $CuInSe_2$ the outer transitions for the quadrupolar interaction are visible as the wider line which can be seen best at 18.8 T. The wide line has

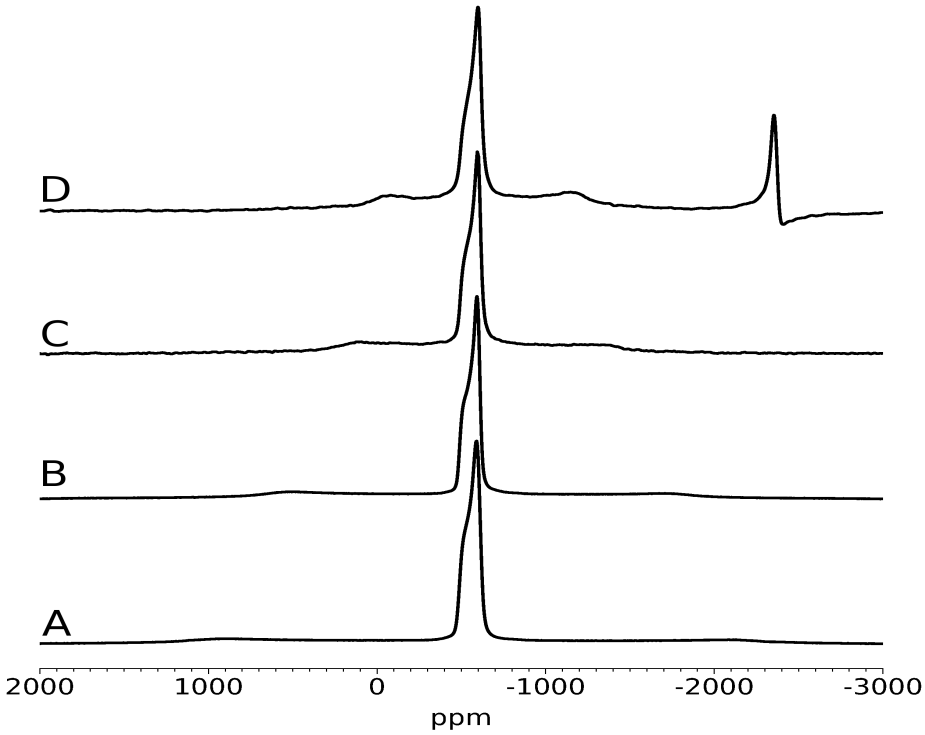

Figure 6.6: ^{65}Cu static NMR spectra of $CuInSe_2$ at A:-7.05T, B:-9.40T, C:-14.10T and D:-18.8T

been attributed to the quadrupolar interaction as it narrows in a linear fashion (in ppm) with increasing field. The only reason the outer transitions are visible in this material is that the quadrupolar interaction is quite small for ^{65}Cu. The copper data for the $CuInSe_2$ shows a very symmetric copper site where the central line is dominated by the CSA interaction as shown in table 6.2. There is a slight amount of disorder in the material as there is a distribution in the quadrupolar coupling constant. The distribution in the quadrupolar interaction can be seen by the fact the the outer singularities are not sharp. If there was no distribution these peaks would be much sharper. The CuInSSe data (figure 6.8) are more complicated than the $CuInSe_2$ data. The site of the copper is less symmetrical in this compound so the quadrupolar interaction is larger and the central line is no longer dominated by

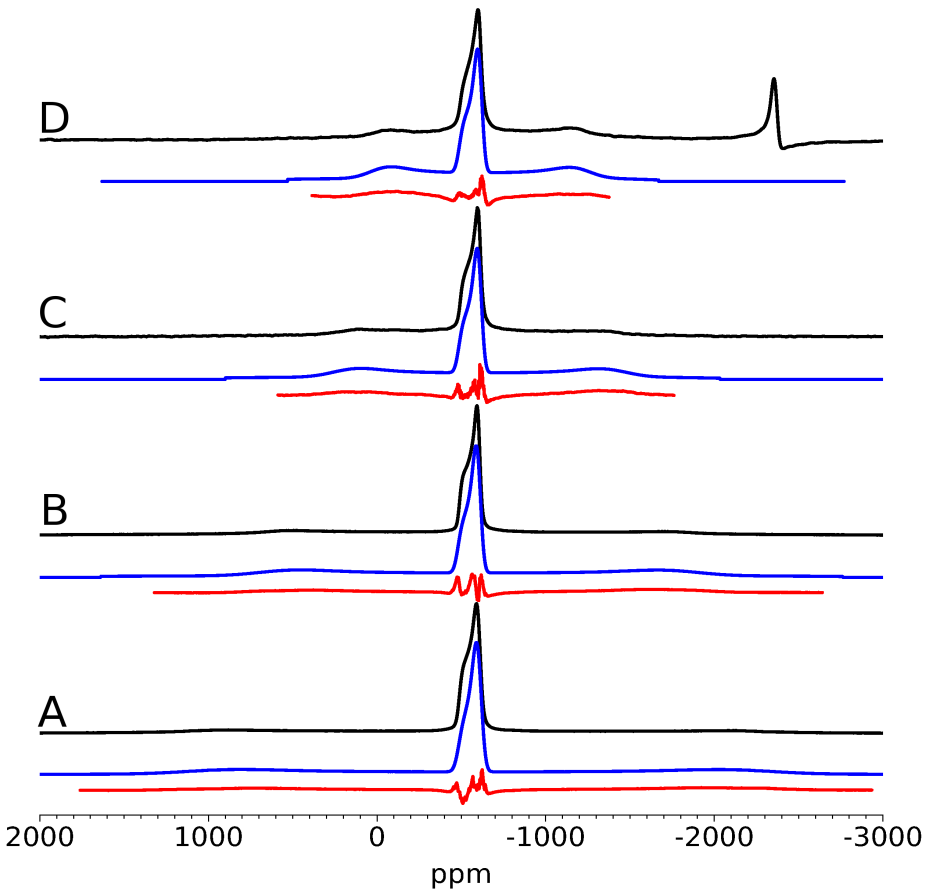

Figure 6.7: Fitted ^{65}Cu static NMR spectra of $CuInSe_2$ at A:-7.05T, B:-9.40T, C:-14.10T and D:-18.8T. Black:- Experimental data, Blue:- Fit and Red:- Difference

the CSA interaction. The copper is likely to be less symmetric due to differences in nearest neighbour of sulphur and selenium in the structure. This can be seen as the line narrows at higher field and the typical line shapes associated with the CSA interaction are not present. As different features of the line can not be attributed to different interactions separately the line becomes far more difficult to fit, especially as there is likely to be a distribution in one or more parameters. Despite the difficulty in obtaining a fit an estimate of the quadrupolar interaction being in the range of 5 MHz and span of the CSA interaction being in the range of 400 ppm can be made.

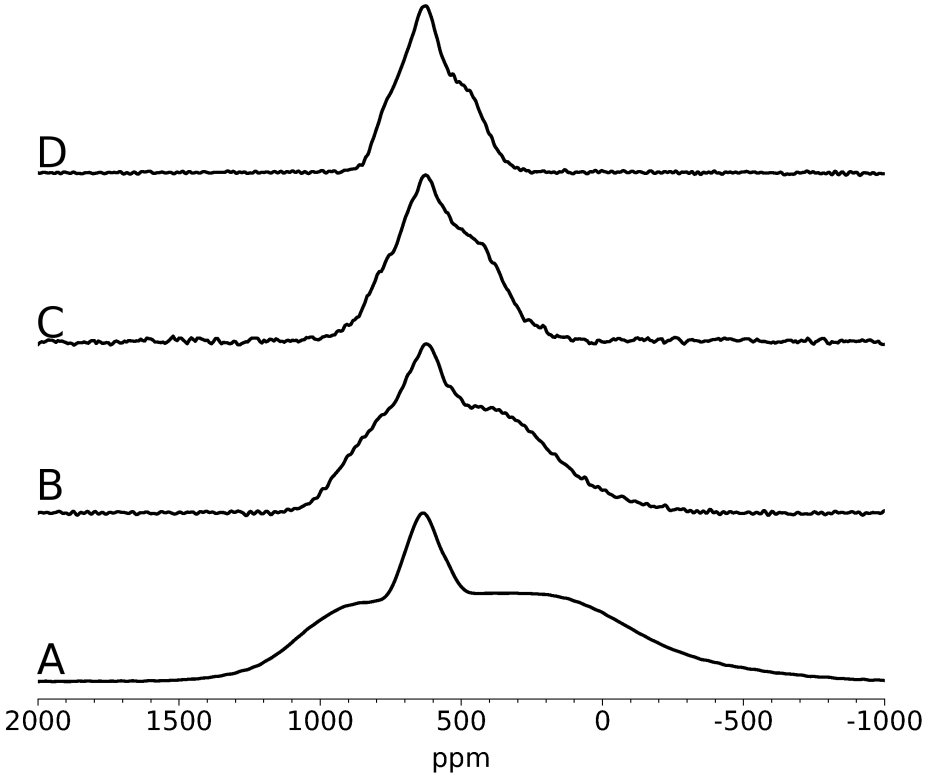

Figure 6.8: ^{65}Cu static NMR spectra of CuInSSe at A:-7.05T, B:-9.40T, C:-14.10T and D:-18.8T

Span	124.7±2.0ppm
Skew	-1±0.1
C_q Centre	0.55±0.05MHz
C_q Width	0.19±0.02MHz
Asymmetry	0±0.1
Shift	-560±2.0ppm
Broadening	300±20Hz/T
α	0±5°
β	90±5°
γ	0±5°

Table 6.2: Fitting parameters for ^{65}Cu NMR spectra of $CuInSe_2$

Indium NMR data is relatively unusual since there are very few examples of this nucleus being studied in the solid state due to ^{115}In having a large quadrupole moment. The ^{115}In solid state static NMR spectra for $CuInSe_2$ are shown in

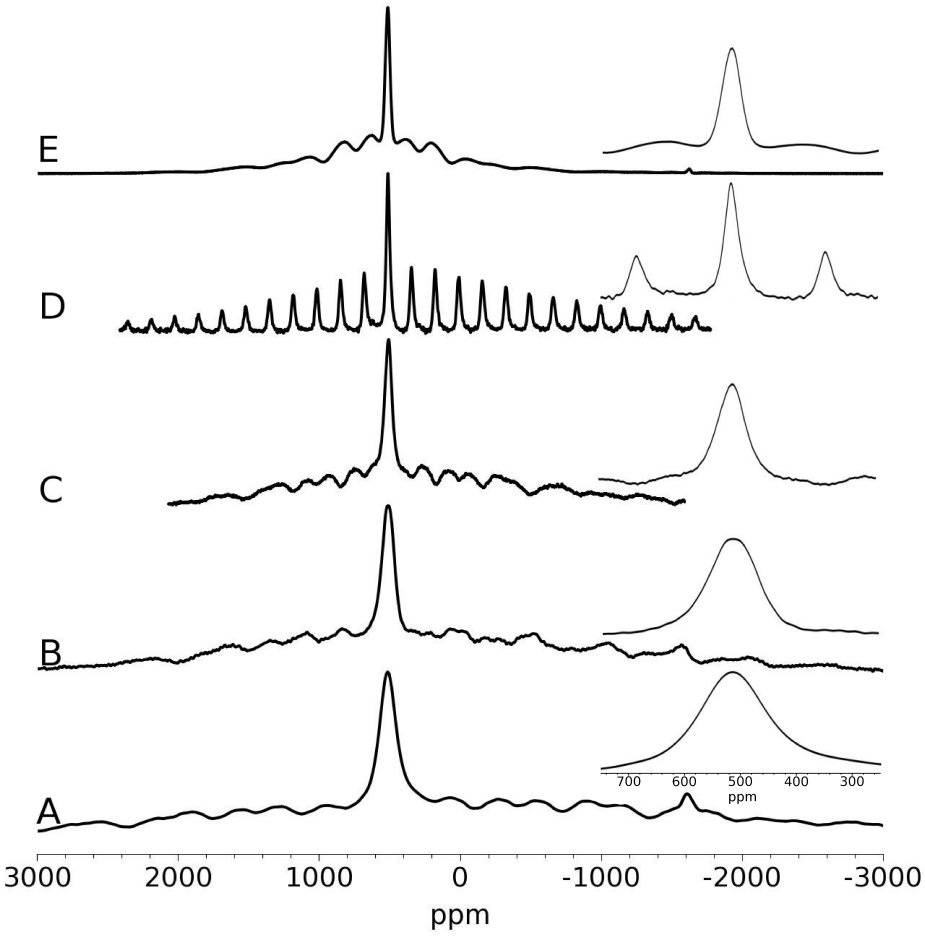

Figure 6.9: ^{115}In static NMR spectra of $CuInSe_2$ at A:-4.8T, B:-8.45T, C:-14.10T, D:-14.10T under MAS and E:-18.80T. The smaller spectra are the central line expanded.

figure 6.9. The set of spectra shows a series of fields including a MAS spectrum at 14.1 T spinning at 30 kHz. The spectra show a narrow line which, in the static case will be a convolution of the quadrupolar interaction and the chemical shielding interaction. The broader lump underneath will be the outer transitions split apart by the quadrupolar interaction. This can be determined as it narrows with increasing field in ppm. As indium has a spin of $\frac{9}{2}$, there are 8 outer transitions which are visible if the conditions are correct. For each of the transitions there

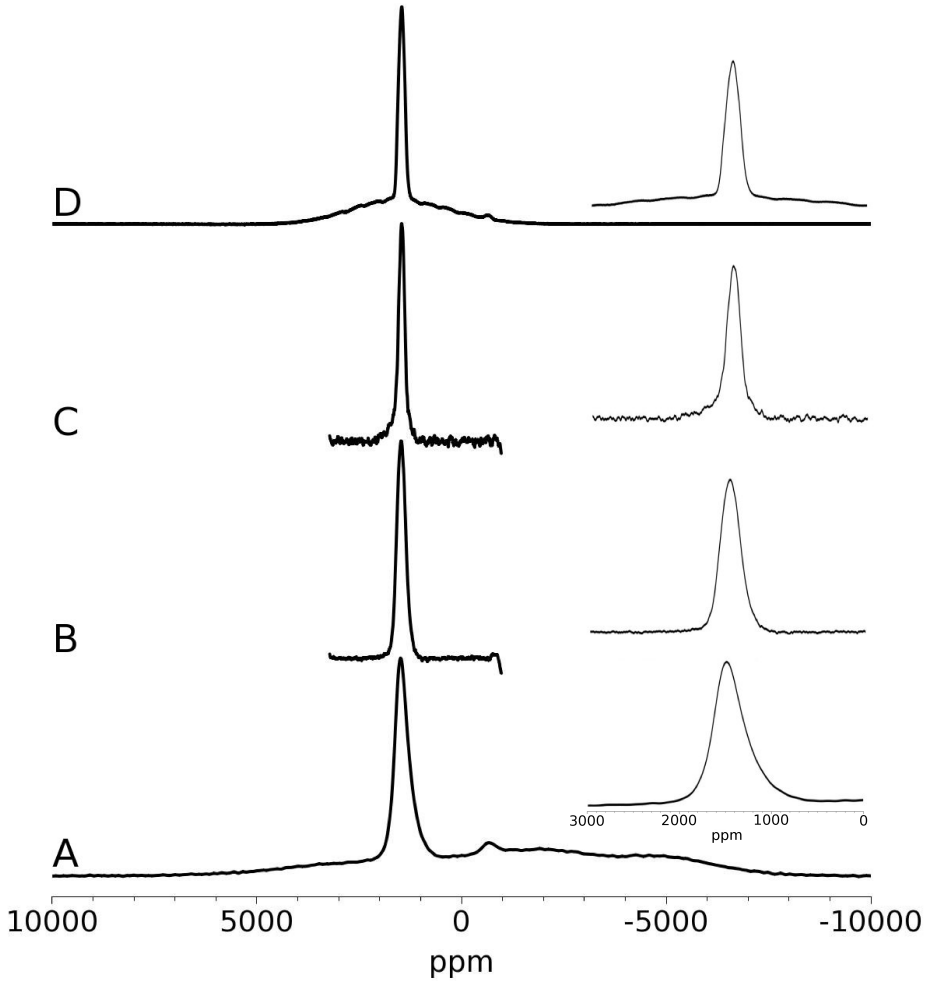

Figure 6.10: ^{115}In static NMR spectra of CuInSSe at A:-4.8T, B:-8.45T, C:-14.10T and D:-18.8T. The inset spectra are the central line expanded.

are two or three features associated with it depending on whether or not the site is axially symmetric. This can lead to the line shape having up to 24 features which will be very difficult to fit. Comparing the width of the central lines against the magnetic field it can be seen that the lines narrow in ppm with increasing magnetic field. The line width in ppm scaling inversely with field implies that the quadrupole interaction is dominant over the CSA interaction. As all of the transitions of the quadrupole interaction are visible, this implies that the magnitude

of the interaction is relatively small. As the quadrupolar interaction is dominant over the CSA interaction in the central line, this implies that the CSA interaction is also very small. There is some distribution in the quadrupolar interactions as the features from the outer transitions are not sharp. These data imply that the material is structurally very ordered with only a slight amount of atomic disorder, with the indium sitting in a very symmetric site. The CuInSSe data shown in figure 6.10, shows the static indium spectra at various fields. There is no MAS data shown, as spinning at 30 kHz at 14.1 T does not fully narrow the central line. At 4.79 T there is a central line and a broad line underneath. As the broader line vanishes at higher field, this can be associated with the CSA interaction of an amorphous secondary phase as it is very broad. The data at 18.8 T also shows a narrow and broad line. The broad line is associated with the outer transitions of the quadrupolar interaction as the broad line is centred on the narrow line and shows features. By looking at the line widths as the field changes it can be seen that the lines narrow slightly as the field increases, however the change is not large enough to say that the quadrupolar interaction is completely dominant. Therefore the quadrupolar and chemical shielding interactions are competing for dominance. Although the interactions are obviously still relatively small the indium is not in a site as symmetric as the copper indium selenide. The broadened outer transitions as shown at 18.8 T and the fact that the resonances are not as narrow as the $CuInSe_2$ show that there is some structural disorder which is probably due to the inclusion of sulphur in the system.

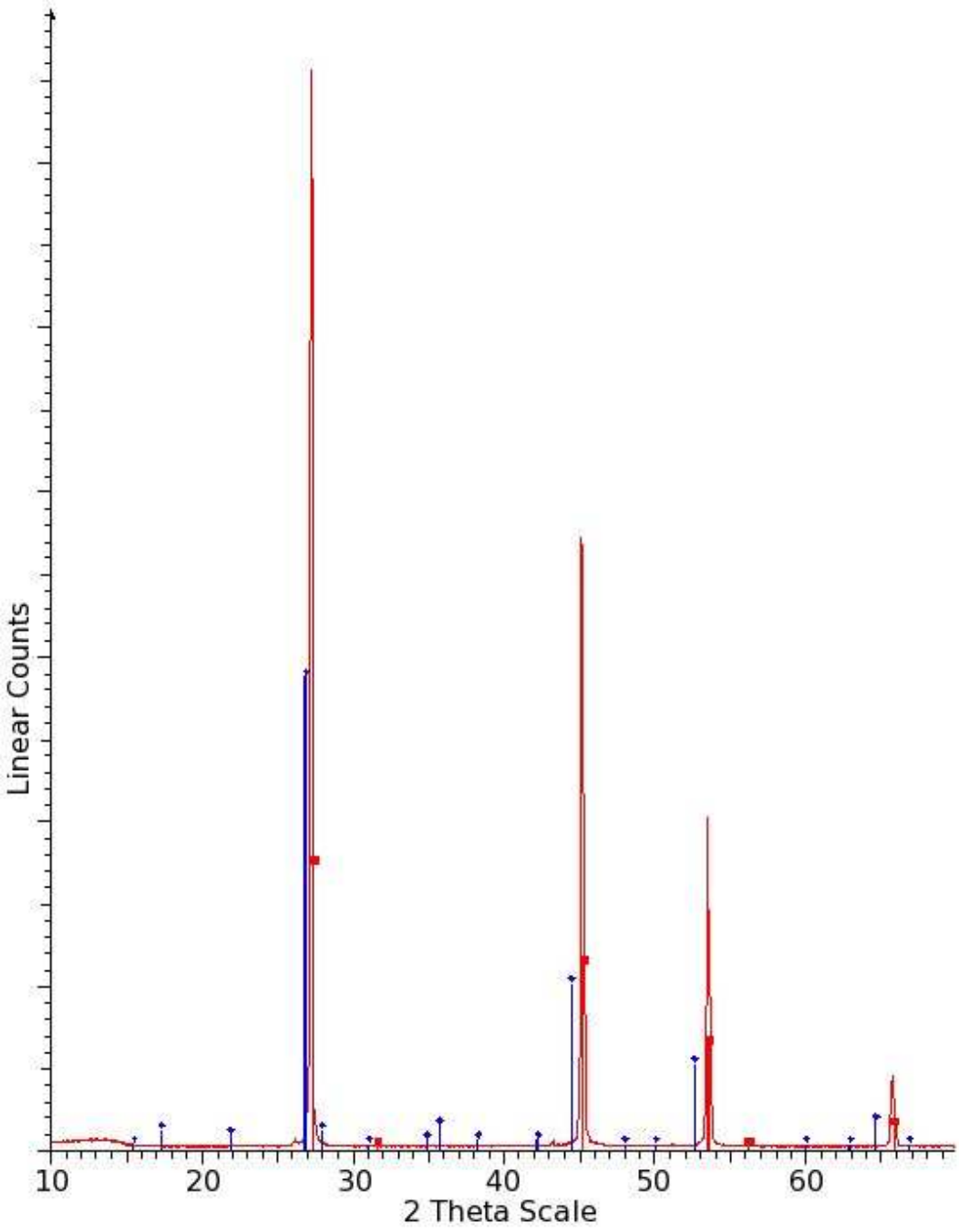

Figure 6.11: XRD data of 2%$CuInSe_2$ in ZnSe supplied by Johnson Matthey. Red vertical lines with red squares are the expected positions of ZnSe, blue vertical lines with blue diamonds are the expected positions of $CuInSe_2$ and the red line is the experimental data.

6.2 Doped Systems

An XRD pattern was obtained from the 2%$CuInSe_2$ in ZnSe sample as shown in figure 6.11. The XRD pattern shows no visible $CuInSe_2$ and all the expected reflections for the ZnSe. The fact that none of the copper indium selenide was observed is not surprising as even a 2% level would appear as a small signal and if only a small proportion of this is left as $CuInSe_2$ it would not be visible. The XRD does however tell us that the zinc selenide has not changed significantly after being doped by $CuInSe_2$.

6.2.1 ^{77}Se MAS NMR

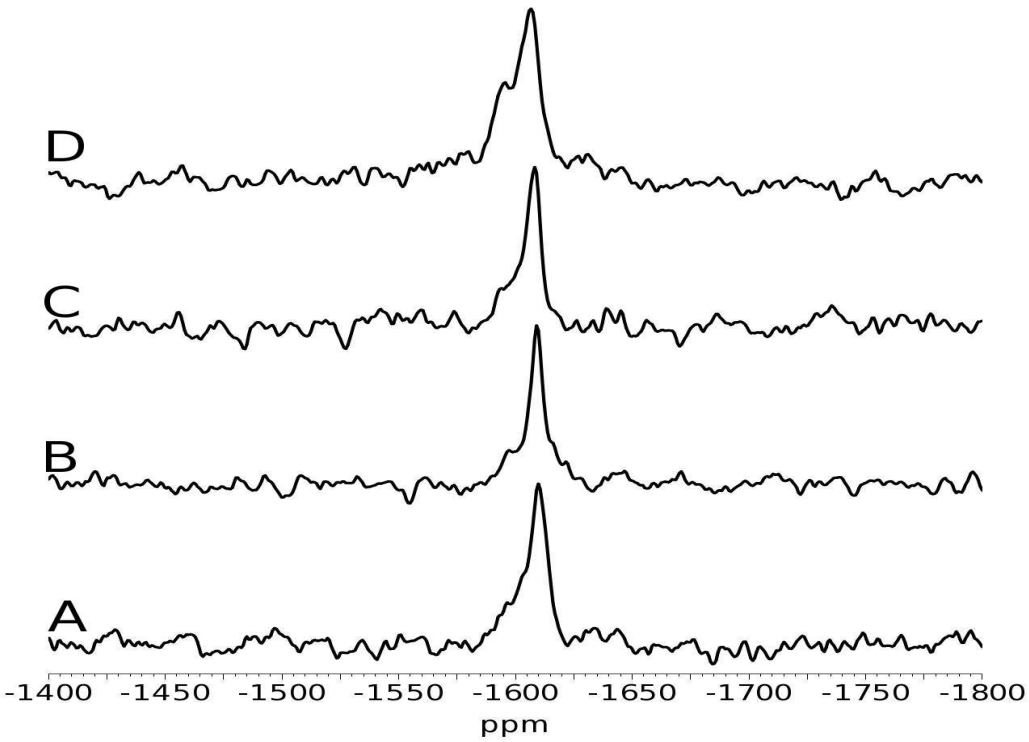

Figure 6.12: ^{77}Se MAS NMR at 4.8 T of A:-2%CuInSSe in ZnSe Fast Fired, B:-2%$CuInSe_2$ in ZnSe, C:-2%$CuInSe_2$ in ZnSe Fast Fired and D:-5%$CuInSe_2$ in ZnSe

Selenium NMR has been carried out on the samples shown in figure 6.12. By comparison with data from the model compounds the signal from the copper indium selenide is not visible and hence only a signal from the zinc selenide is observed. As the signal is being obtained from the ZnSe which is the main material, it makes ^{77}Se NMR an ideal probe of the effect of the dopant on the doped material.

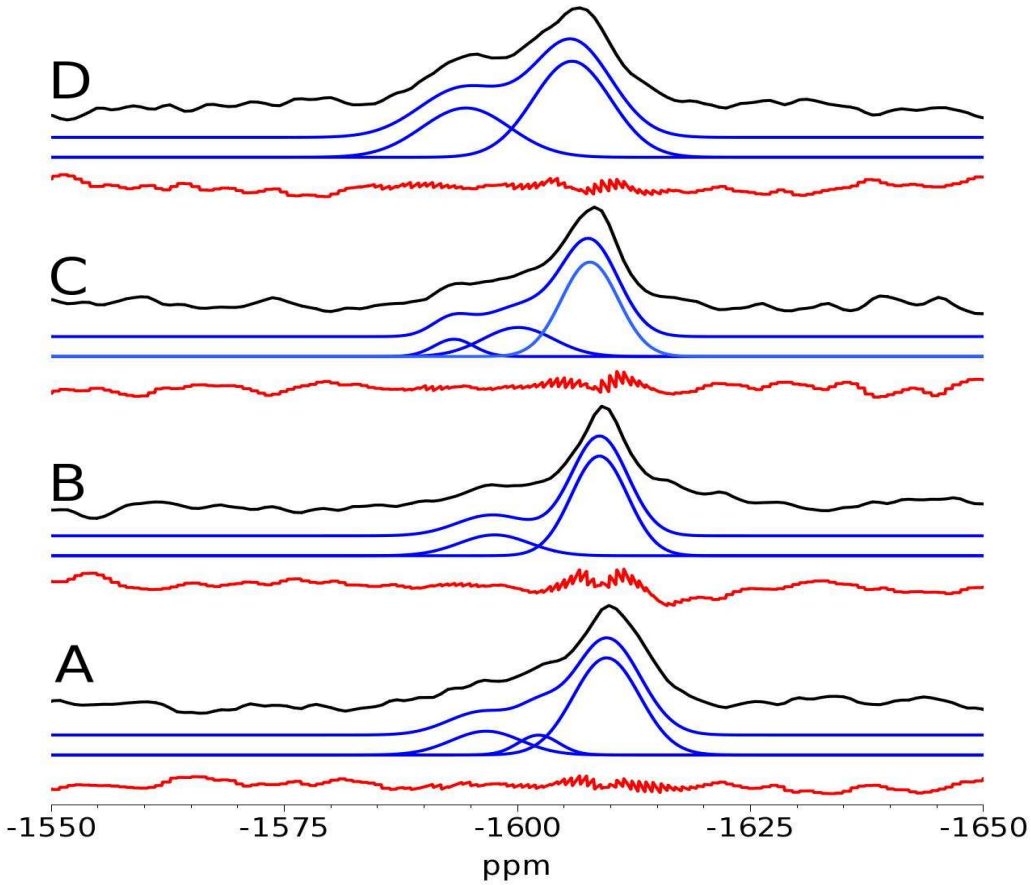

Figure 6.13: Fitted ^{77}Se SS MAS NMR at 4.8 T using Gaussian peaks. Black is the experimental data, blue is the total fit and the lines which make up the total fit and red is the difference between the experimental data and the total fit. A:-2%CuInSSe in ZnSe Fast Fired, B:-2%$CuInSe_2$ in ZnSe, C:-2%$CuInSe_2$ in ZnSe Fast Fired and D:-5%$CuInSe_2$ in ZnSe

As the ^{77}Se MAS NMR spectra differ from each other they were fitted using Gaussian peaks as shown in figure 6.13, with the fitting parameters shown in table

6.3. The 5% $CuInSe_2$ doped sample shows a second site slightly different from the zinc selenides normal shift. This led to the fitting of second and third sites in all of the samples. The errors in the fitting parameters are however relatively large due to the relatively low signal to noise ratio of the spectra. From the data obtained it can be seen that there tends to be a reduction in the line widths for the fast fired samples and the appearance of a possible third site. There is the possibility that if the third site was removed the line width would increase in line with the other samples. However, due to the shape of the outer edges of the line in the spectra and the other data acquired this is not deemed to be likely.

Sample	**Site**	**Width±20 (Hz)**	**Shift±3 (ppm)**	**±5%**
2%$CuInSe_2$	1	200	-1597	20.7
	2	150	-1609	79.3
2%$CuInSe_2$FF	1	100	-1594	8.5
	2	180	-1600	25.2
	3	130	-1608	66.3
2%CuInSSeFF	1	180	-1597	18.6
	2	100	-1603	9.0
	3	170	-1610	72.4
5%$CuInSe_2$	1	220	-1595	36.8
	2	190	-1606	63.2

Table 6.3: Parameters for fitting the ^{77}Se MAS NMR data. FF refers to the Fast Firing method in material preparation.

6.2.2 ^{63}Cu MAS NMR

Copper MAS NMR spectra of the doped zinc selenides have also been obtained as these together with the indium data can be used to determine how the dopant is interacting with the material. The choice between the two different isotopes of copper is relatively difficult. As the levels of dopant are low it was decided that ^{63}Cu would be most appropriate. ^{63}Cu is approximately twice as abundant

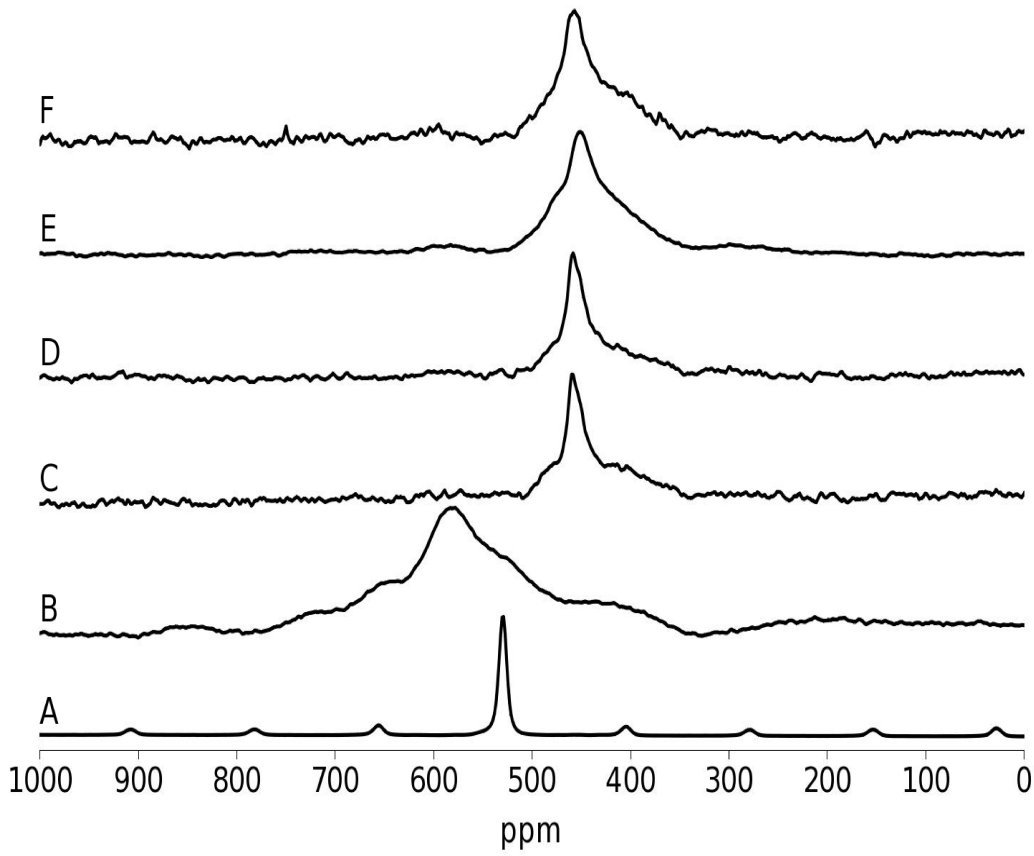

Figure 6.14: ^{63}Cu SS MAS NMR spectra at 14.1 T of A:-$CuInSe_2$, B:-CuInSSe, C:-2%CuInSSe in ZnSe Fast Fired, D:-2%$CuInSe_2$ in ZnSe, E:-2%$CuInSe_2$ in ZnSe Fast Fired and F:-5%$CuInSe_2$ in ZnSe

as ^{65}Cu, however it also has a quadrupole moment which is approximately 10% larger. The increased abundance results in approximately twice as much signal per acquisition, however the increased quadrupole moment results in line widths which are roughly 1.25 times wider than ^{65}Cu line widths. Once a spectrum has been obtained, if it is too wide to narrow fully under MAS then a ^{65}Cu spectrum can be obtained. The spectra in figure 6.14 show a distinct change between the original dopant and the final doped material with very little or no original material left. There are however two sites appearing at approximately 450 ppm. The spectra were then simulated (figure 6.15) using Gaussian peaks as there was no way of

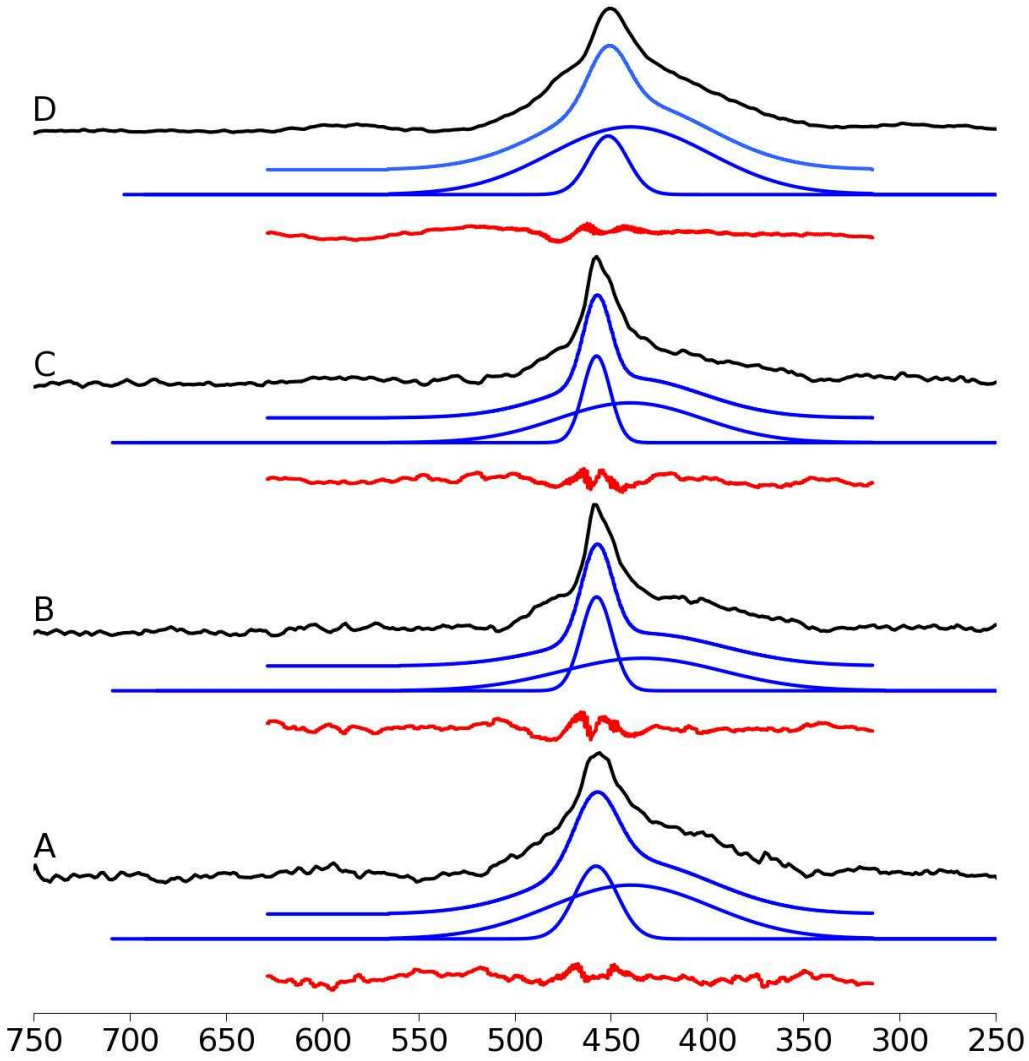

Figure 6.15: Simulated ^{63}Cu SS MAS NMR spectra at 14.1 T using Gaussian peaks. Black is the experimental data, blue is the total fit and the lines which make up the total fit and red is the difference between the experimental data and the total fit. A:-2%CuInSSe in ZnSe Fast Fired, B:-2%$CuInSe_2$ in ZnSe, C:-2%$CuInSe_2$ in ZnSe Fast Fired and D:-5%$CuInSe_2$ in ZnSe

distinguishing a quadrupolar line shape from the line, and the lack of spinning side bands implies that the quadrupolar and CSA interactions are very small as they have been completely spun out. The simulation parameters are shown in table 6.4. The only real conclusion from the data is that the broad site has increased with

increased level of dopant and that there is the possibility of a peak appearing at the same shift as the dopant.

Sample	Site	Width±20 (Hz)	Shift±3 (ppm)	±5%
2%$CuInSe_2$	1	8020	434.3	64
	2	1350	457.6	36
2%$CuInSe_2$FF	1	7220	440.6	71
	2	1350	457.6	29
2%CuInSSeFF	1	8020	440.3	74
	2	2130	457.9	27
5%$CuInSe_2$	1	7340	440.6	82
	2	1950	451.6	18

Table 6.4: Parameters for fitting ^{63}Cu MAS NMR spectra.

6.2.3 ^{115}In NMR

Due to indium's very large quadrupole moment it could be a useful tool in determining the structural and atomic order of a material as it is likely to be very sensitive to changes in the electric field gradient produced from asymmetries in the electric charge distribution in the structure. Indium NMR is used to determine how the indium interacts with the doped materials and spectra have been obtained as shown in figure 6.16. There is a clear difference between the dopants and the doped materials. There is a relatively small amount of the original dopant left and several sites which must be due to the indium interacting with the zinc selenide. To get a better understanding the spectra have been simulated with the simulations shown in figure 6.17 and the simulation parameters shown in table 6.5.

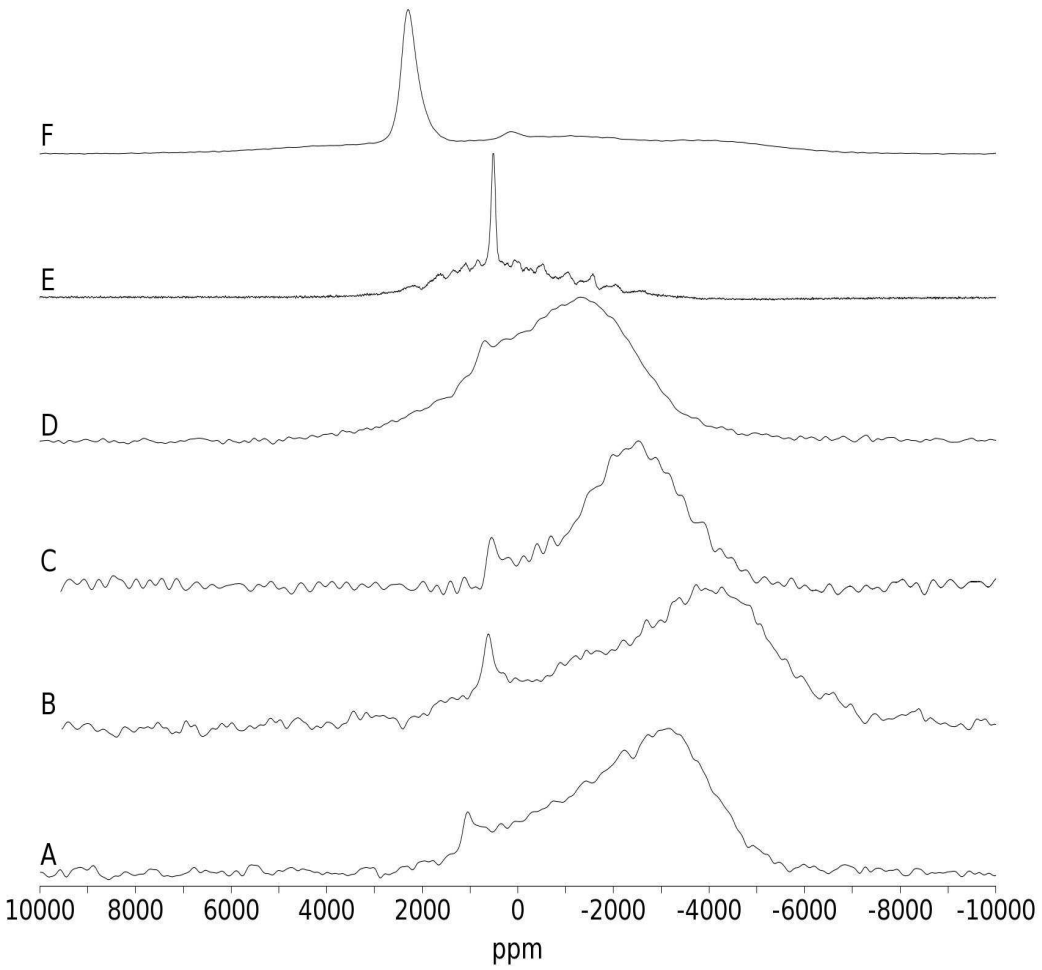

Figure 6.16: ^{115}In NMR at 8.45 T whilst static of A:-2%$CuInSe_2$ in ZnSe Fast Fired, B:-2%$CuInSe_2$ in ZnSe, C:-2%CuInSSe in ZnSe Fast Fired, D:-5%$CuInSe_2$ in ZnSe, E:-$CuInSe_2$ and F:- CuInSSe

The line at approximately 600 ppm is assigned to the copper indium selenide dopant and the broader lines with indium which is interacting with the zinc selenide. The fits show that for the CuInSSe doped ZnSe there is no CuInSSe left in the material. This could be due to the sulphur moving into the zinc selenide preferentially with the copper and the indium, leaving only $CuInSe_2$. The broader lines have been associated with the indium interacting with the zinc selenide due to their large widths and different shifts from the $CuInSe_2$. The only broad line

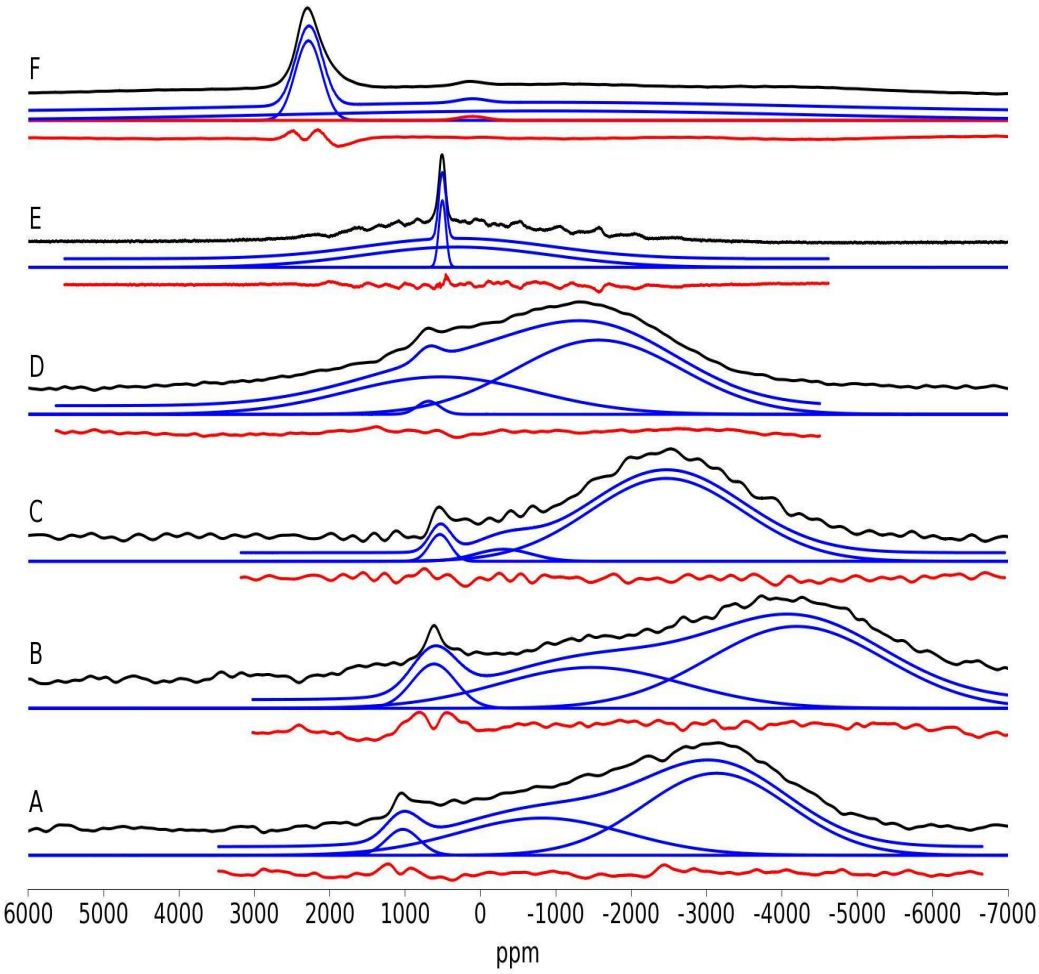

Figure 6.17: Fitted ^{115}In SS NMR at 8.45 T whilst static. Black is the experimental data, blue is the total fit and the individual lines which make up the total fit and red is the difference between the total fit and the spectra. A:-2%$CuInSe_2$ in ZnSe Fast Fired, B:-2%$CuInSe_2$ in ZnSe, C:-2%CuInSSe in ZnSe Fast Fired, D:-5%$CuInSe_2$ in ZnSe, E:-$CuInSe_2$ and F:- CuInSSe

which is difficult to assign is the line in the 5% doped sample at approximately 700 ppm. This line could either be associated with the indium interacting with the zinc selenide or it could be an amorphous phase of copper indium selenide.

As the copper is very similar in size to zinc it can be assumed that the indium is relatively unaffected by how close the copper is. However, as the copper is Cu(I), it will cause defects and distortions in the material which the indium will pick up. A series of different sites would appear depending on the proximity of other copper or indium in the material.

Material	**Site**	**Width (Hz)**	**Shift±3 (ppm)**	%
$CuInSe_2$	1	4460±100	514	11±3
	2	117900±3000	312	89±3
CuInSSe	1	16800±1000	2289	45±2
	2	17700±1000	108	2.3±2
	3	330000±5000	-815	53±2
$2\%CuInSe_2$	1	27700±1000	622	8.2±3
	2	115600±2000	-1477	31±3
	3	111100±2000	-4194	61±3
$2\%CuInSe_2$FF	1	20800±1000	1036	4.5±2
	2	105120±2000	-820	33±2
	3	91800±2000	-3123	63±2
2%CuInSSeFF	1	13200±500	545	4.1±2
	2	35200±500	-306	4.8±2
	3	96500±1000	-2467	91±2
$5\%CuInSe_2$	1	14200±300	696	1.5±2
	2	117900±1000	524	36±2
	3	105000±1000	-1565	63±2

Table 6.5: Parameters for fitting the ^{115}In SS NMR spectra.

As some of the samples have been fast fired, this is likely to affect the structural order of the materials. In figure 6.18 the widths of the fitted peaks are plotted. In figure 6.18 some of the widths have been multiplied up to make a comparison of line widths simpler. For the fast fired samples there is a general trend that their line widths are narrower than those for samples which are fired normally. The reduction in line width can be attributed to less atomic/structural disorder in the materials.

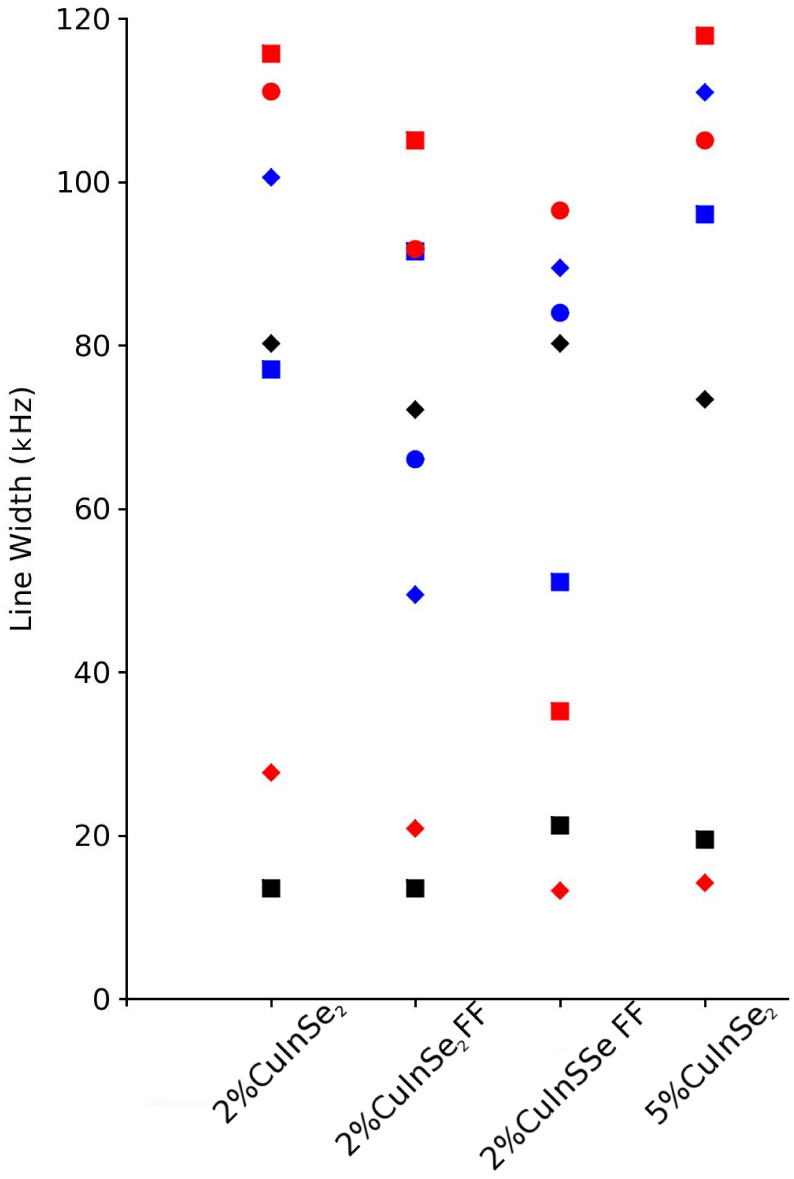

Figure 6.18: Line width analysis of copper indium sulphur selenide doped zinc selenides. Black is 10 times the ^{63}Cu line width, Blue is 500 times the ^{77}Se line width and Red is the ^{115}In line width. The diamonds are site 1, squares site 2 and circles site 3.

6.3 Conclusion

The increase in line widths and the change in shifts between the original materials and the doped materials imply that the copper and indium are moving into the

structure of the zinc selenide. If we assume that the substitution of the copper and indium for the zinc is random we can make some calculations using a binomial distribution as to whether the random model is accurate. For the copper there are two sites, one narrow which can be assumed to be a symmetric site and one broad which is a distorted site. The distorted site must be produced by indium sitting at a given distance from the copper. Given the random model the probability of one indium only being separated by one selenium atom from one or more copper is 45.6% for the 5% sample and 21.5% for the 2% doped samples. As the ratio of the two copper sites does not change significantly we could assume that the effect of the indium is longer range. The probability of there being one indium separated by two selenium atoms from the copper is then 86.5% for the 5% doped samples and 54.5% for the 2% doped samples. Although for the higher level of doping these probabilities are just within error, for the lower doping these probabilities are considerably outside error. As the probabilities do not correspond to each other it can be assumed that the random model is therefore incorrect leading to the conclusion that the position of the copper and indium in the zinc selenide is linked in some way. The fact that with higher doping the level of broader sites increases only slightly corresponds to this conclusion. Furthermore it can be assumed that the broad site is due to the indium being separated from the copper by only one selenium, as if this was not true then the broad site would be much larger in intensity. If a random model for the substitution of the copper indium pairs is assumed there will be 38.4% of copper indium pairs which are within one selenium of another copper indium pair for the 5% doped sample and 29.3% of the 2% doped sample. This calculated 9.1% difference is shown by the jump in the intensity of the broader site in table 6.4.

For the indium data if we initially assume a lone copper indium pair, there are two possibilities, one in which the copper and indium are separated by one selenium and one in which they are separated by more than one selenium. This would lead to two indium sites, which should agree with the ratios seen in the copper data. However this is not the case. The system with the various indium sites is not simple and does not agree with a simple random model of copper-indium pairs in the system. If preferential orientation of the pairs occurred (i.e. along one crystallographic axis) this could go some way to explaining the distribution in indium sites, however the amount of information about this system is not sufficient to make any robust conclusion.

The main conclusion from the selenium data is the effect on the selenium from the indium or copper is relatively short range. If it affected more than the nearest neighbour the proportion of the selenium which would see an indium or copper would be 99.3% for the 5% doping and 46.2% for the 2% doping which is larger than than which was observed.

Chapter 7

Mesoporous Oxides

Mesoporous materials have many uses in industry from catalysts to hydrogen-storage media[91]. Mesoporous materials are defined by regular arrays of pores. The pore sizes are usually highly controllable and along with the large surface area lead to the possibility of highly selective and active catalysts. The large amount of regular pores with highly controllable pore size also lend themselves to molecular sieves.

Sample	**Peak Position** (ppm)	**Line Width** (Hz)	**Other information**
Amor Nb	535±10	3800±100	
Meso Si	33±10*		C_Q=5MHz±0.4, η=0±0.1, broadening = 1200±50Hz
Meso Ti	690±10	2400±50	
Meso Ta	432±5	2220±30	
Meso Nb	518±10	3900±50	

Table 7.1: ^{17}O peak parameters for mesoporous oxides and amorphous niobia. *indicates isotropic chemical shift not peak position

Figure 7.1 shows ^{17}O MAS NMR data for a range of mesoporous oxides and the amorphous niobia. The peak parameters are shown in table 7.1. There is a shift

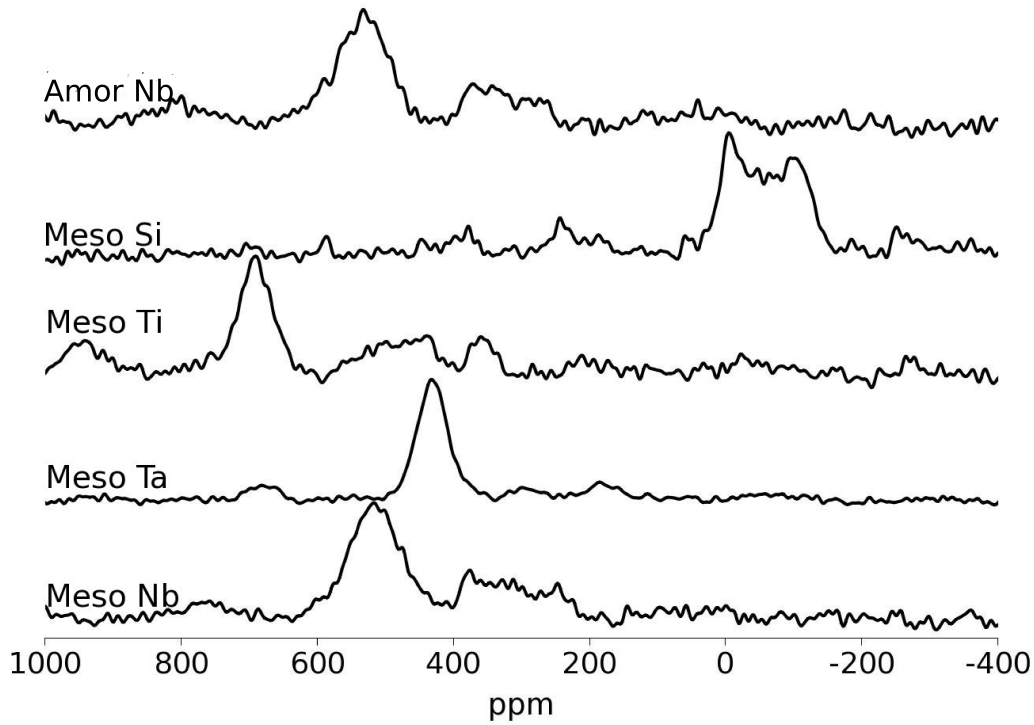

Figure 7.1: ^{17}O Solid State MAS NMR spectra taken at 7.05 T of mesoporous oxides

between the amorphous niobia and the meso niobia of 17 ppm, which implies that there is a change in the oxygen site although it is not significant. The reported shift ranges of oxygen in a niobia system for ONb_2 is in the region of 550 ppm and in the region of 360 ppm for ONb_3[92, 93]. The shift ranges imply that the oxygen is the ONb_2 configuration in both cases with slight differences between the amorphous and mesoporous materials. The line widths of the amorphous and mesoporous samples are the same to within error. The similarity in line widths implies that the symmetry of the site has not changed significantly, as this would induce field gradients which would cause significant second-order quadrupolar broadening. The meso Ta sample shows a single peak at 432 ppm which does not show any second-order broadening and is in the region expected for OTa_3 (OTa_3 is reported at 455

ppm and OTa_2 at 305 ppm[94]). The meso Ti sample also shows a line which has not been significantly broadened by second-order quadrupole broadening implying that the site is relatively symmetric. The shift of the line is 690 ppm which lies outside of the normal shift range of TiO_2 (Anatase 557 ppm[95], Rutile 596.5 ppm[95] and Brookite 552 ppm and 584 ppm[96]). This difference in shifts implies that the oxygen site is significantly different than the normal TiO_2, although it is still relatively symmetric. The mesoporous silicate sample shows significant second-order quadrupolar broadening with a C_Q of 5±0.4 MHz and a η=0±0.1. The parameters for the quadrupolar interaction imply that the site is asymmetric but does have axial symmetry. The shift of 33 ppm is similar to 46 ppm[97] previously reported.

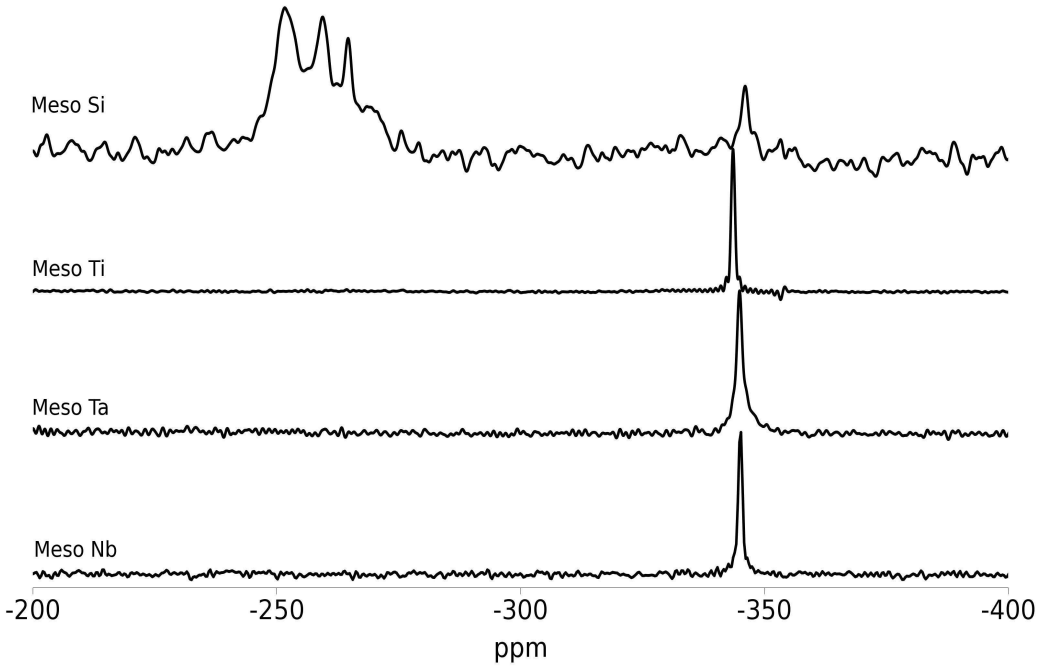

Figure 7.2: ^{15}N Solid State MAS NMR spectra taken at 7.05 T of ^{15}N and ^{17}O enriched mesoporous oxides with the amine template still in place.

Figure 7.2 shows the ^{15}N spectra for various mesoporous oxides which have not had their support removed. The NMR spectra of the mesoporous silica is significantly more complicated than the spectra of the other mesoporous oxides. The NMR spectra of the mesoporous silica has been fitted as shown in figure 7.3. The parameters for the lines and fit are shown in table 7.2.

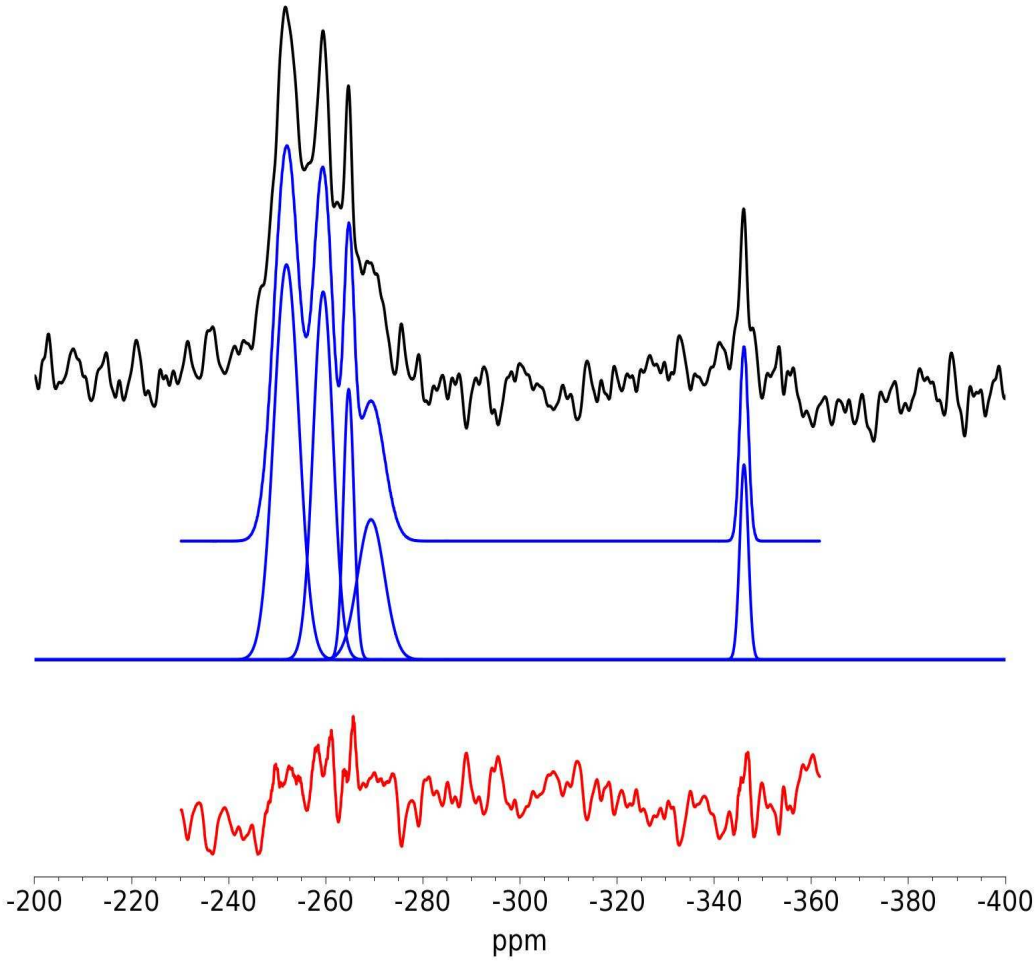

Figure 7.3: ^{15}N Solid State MAS NMR spectra taken at 7.05 T of mesoporous silica (black), fitted using Gaussians(blue) and with the difference between the fit and spectra (red).

Sample	**Peak Position (ppm)**	**Line Width (Hz)**	%
Meso Nb	-345.0±0.5	36±2	
Meso Ta	-344.9±0.5	45±2	
Meso Ti	-343.6±0.5	28±1	
Meso Si	-251.8±0.5	203±5	40±5
	-259.4±1.0	144±5	26±5
	-264.5±1.0	89±5	12±5
	-269.1±1.0	206±5	14±5
	-346.0±1.0	80±5	8±5

Table 7.2: ^{15}N peak parameters for mesoporous oxides

The amine supporting group in the mesoporous oxide is the only substance which contains nitrogen. The ^{15}N NMR spectra shows how the amine is interacting with the oxide. The width of the line gives an insight into the distortion of the amine group. All of the samples have a line at approximately -345 ppm which can be associated with the amine group[43]. The meso Ti spectrum shows baseline distortions at the base of the only peak in the spectrum. These are truncation artifacts, caused by truncation of the FID. The FID was truncated as it was sufficiently long that to acquire the whole signal would result in damaging the probe. The meso Ti sample shows the narrowest line, which implies that the amine group is least distorted so held most loosely. The meso Nb is the next narrowest, then the meso Ta and finally the meso Si which has several sites. The extra sites in the meso Si are in the region where NH[98] groups appear. The existence of various peaks in the NH region implies that during manufacture the amine has split up and NH groups have attached themselves to multiple sites on the surface.

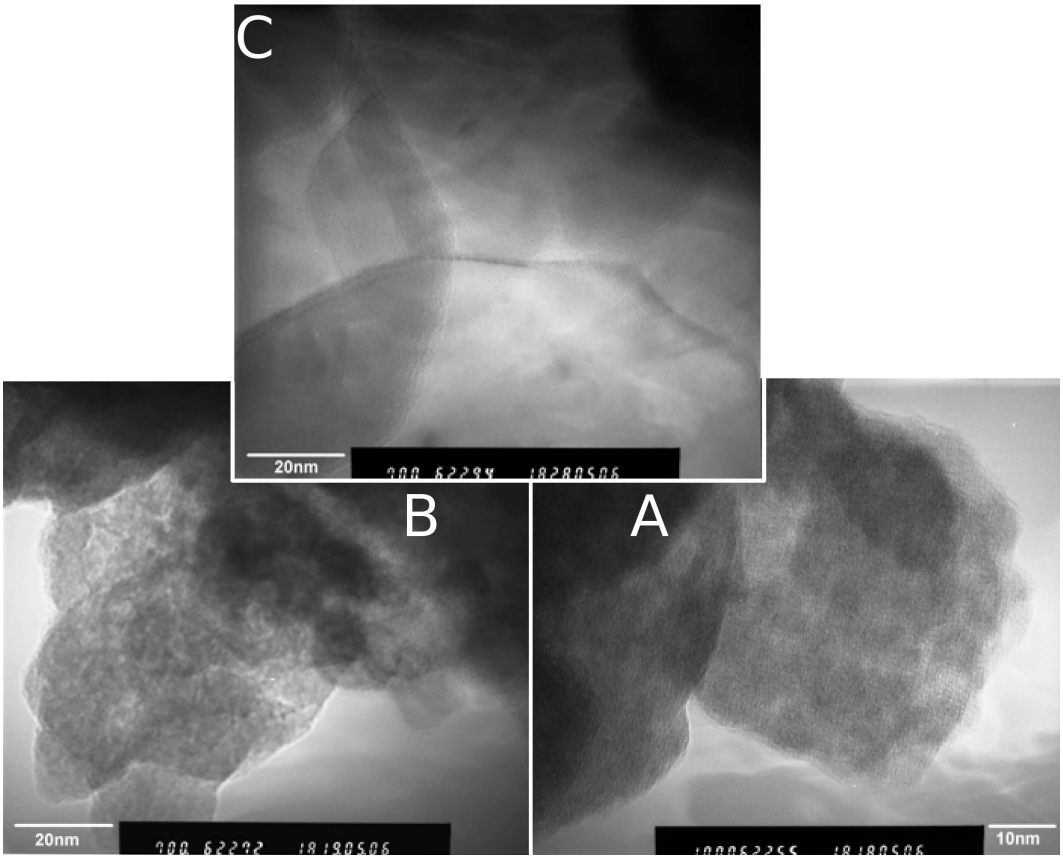

Figure 7.4: TEM images of meso Nb, A:- as prepared, B:- after heating to 500°C and C:- after heating to 750°C

7.1 Effects of Heat Treating

The transmission emission microscopy (TEM) images shown in figure 7.4 are of mesoporous niobia with various heat treatments to show the stability of the material with heating. Image "A" is the as prepared sample and relatively small hexagonal pores can be seen of approximately 30 nm. With heating the sample to 500°C as shown in image "B" the pore size does not change significantly. The material changes significantly however if it is heated to 750°C as shown in image "C" where the pores are now in the region of 100 nm.

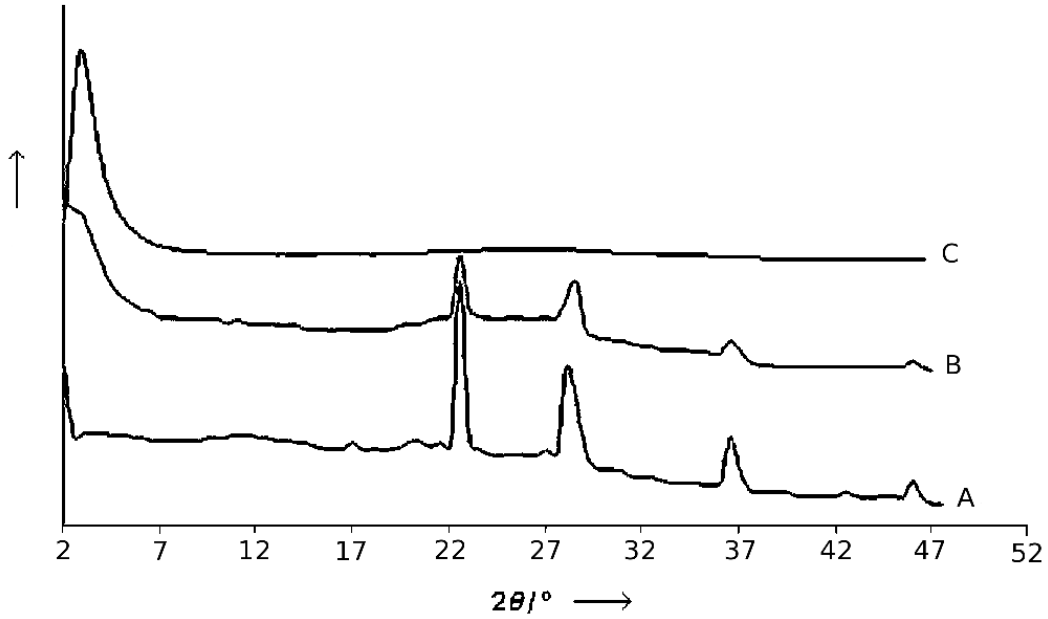

Figure 7.5: XRD of mesoporous niobium oxide after heating at A:-750°C, B:-500°C and C:-Unheated sample.[8]

Figure 7.5 shows XRD results from mesoporous niobia with different heat treatments. The peak at approximately 2.5° is due to the bulk meso structure[99, 100]. As the temperature increases other peaks occur and the peak from the mesoporous structure reduces in intensity. The reduction in the amount of mesoporous structure in the material is also shown by surface area measurements of 700 m^2 g^{-1} in the unheated sample to less than 5 m^2 g^{-1}[8] for the sample heated at 750°C. The extra peaks occur at approximately 22°, 28° and 37°. These can be closely indexed by a orthorhombic phase (JSCPDS 27-1313) of niobia.

Figure 7.6 shows ^{17}O MAS NMR spectra of mesoporous niobia after various heat treatments. The parameters of the lines are shown in table 7.3. From heating the sample to 250°C or 500°C there is very little difference apart from slight variations in line width and shift. Once the sample is heated to 750°C there is a substantial change with a second site appearing. The second site is probably due

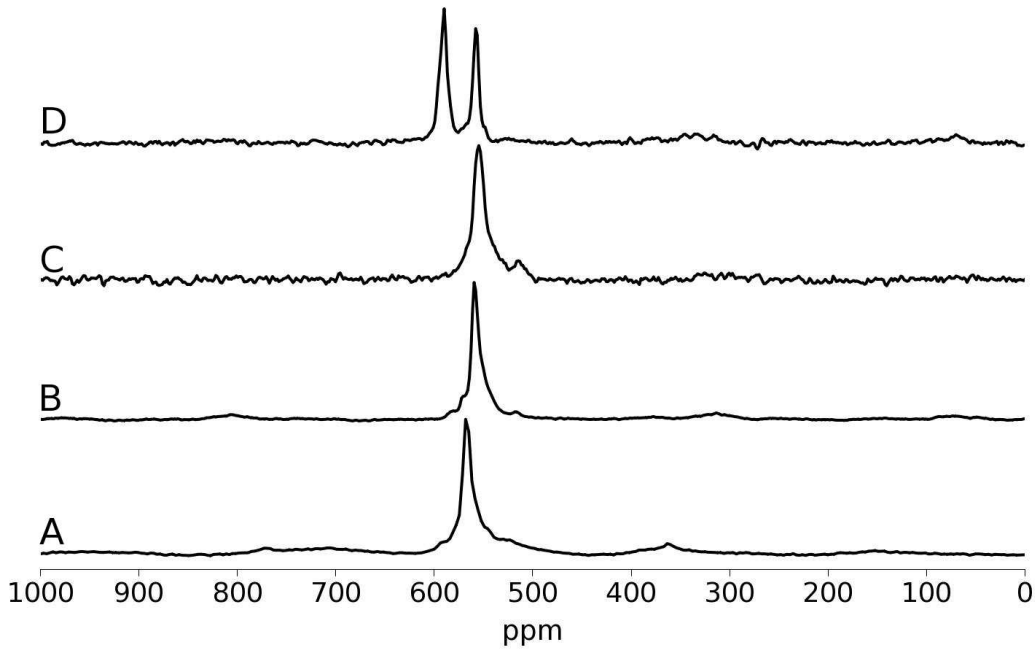

Figure 7.6: ^{17}O NMR spectra of mesoporous niobium oxide after extra heat treatments at A:- No extra heat treatment, B:-250°C, C:-500°C and D:-750°C

to the orthorhombic phase of niobia seen in the XRD[101, 102, 92]. Althought the XRD shows the secondary site in the sample fired at 500^{o}C this does not apear in the NMR results, the reason for this remains unclear. The difference between the shifts of the two lines in figure 7.6D is similar to that shown from table 7.1 for the mesoNb and AmorNb samples. The shifts are different because the shifts shown in table 7.1 are peak positions and not isotropic shifts. For a quadrupolar line the isotropic shift is higher than the peak position.

Temperature (°C)	**Peak Position (ppm)±2.0**	**Line Width (Hz)±10**
un-heated	565.7	290
250	558.3	210
500	554.3	340
750	557.1	200
	590.6	220

Table 7.3: ^{17}O peak parameters for temperature series of mesoporous niobia

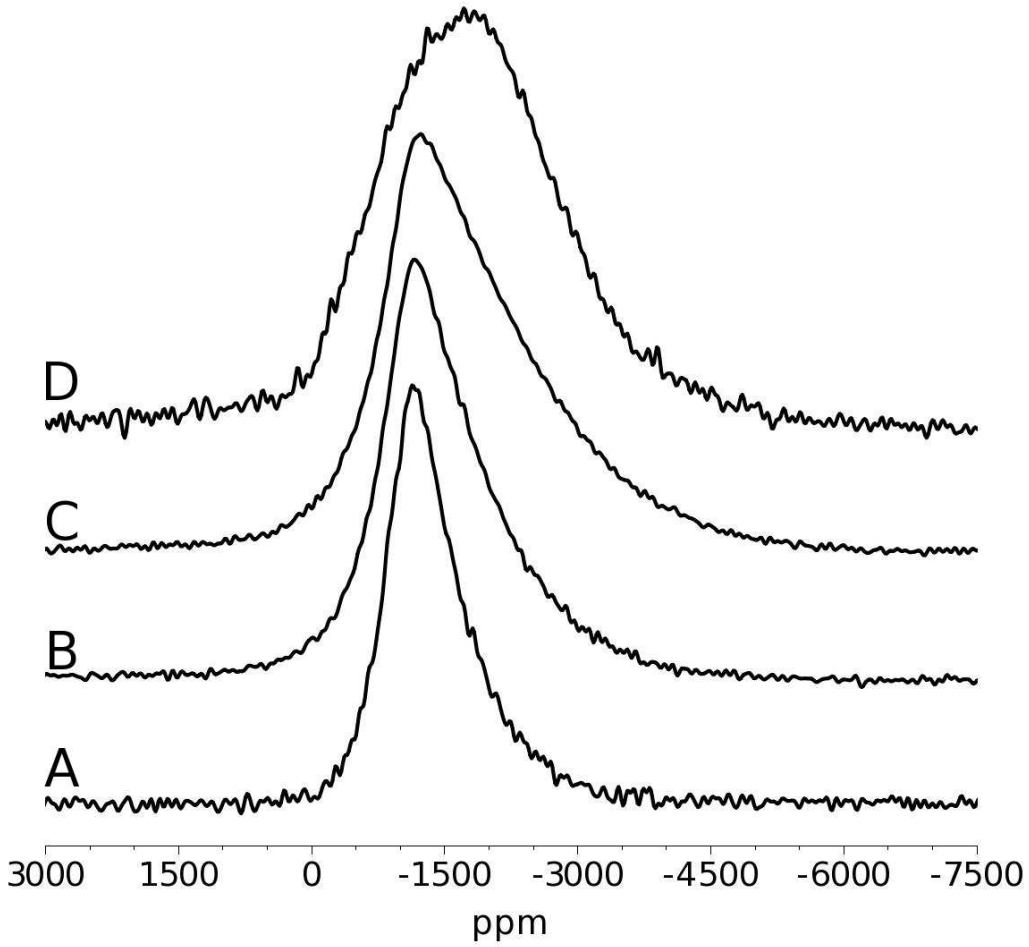

Figure 7.7: ^{93}Nb NMR spectra of mesoporous niobium oxide after extra heat treatments at A:- No extra heat treatment, B:-250°C, C:-500°C and D:-750°C

Figure 7.7 shows ^{93}Nb NMR spectra of the same heat treated series as in figure 7.6. The peak positions of the lines, as shown in table 7.4, show that the line is moving towards more negative shift as the heat treatment is increased. The line widths are also slowly increasing as the temperature increases. The shift of the peak position towards negative shifts and the increase in line width implies that the quadrupole coupling constant for the site is slowly increasing as the heat treatment increases and the shift stays roughly constant. There was however a

significant change in the line shape once the heat treatment reached 750°C. The line shape implies either a substantial change in the axial symmetry of the niobium site or a second niobium site. From the evidence of the XRD and the ^{17}O NMR, the second niobium site is more probable.

Temperature (°C)	**Peak Position (ppm)**	**Line Width (Hz)±1000**
un-heated	-1140±10	134500
250	-1170±10	180700
500	-1230±10	251300
750	-1720±30	332000

Table 7.4: ^{93}Nb peak parameters for temperature series of mesoporous niobia

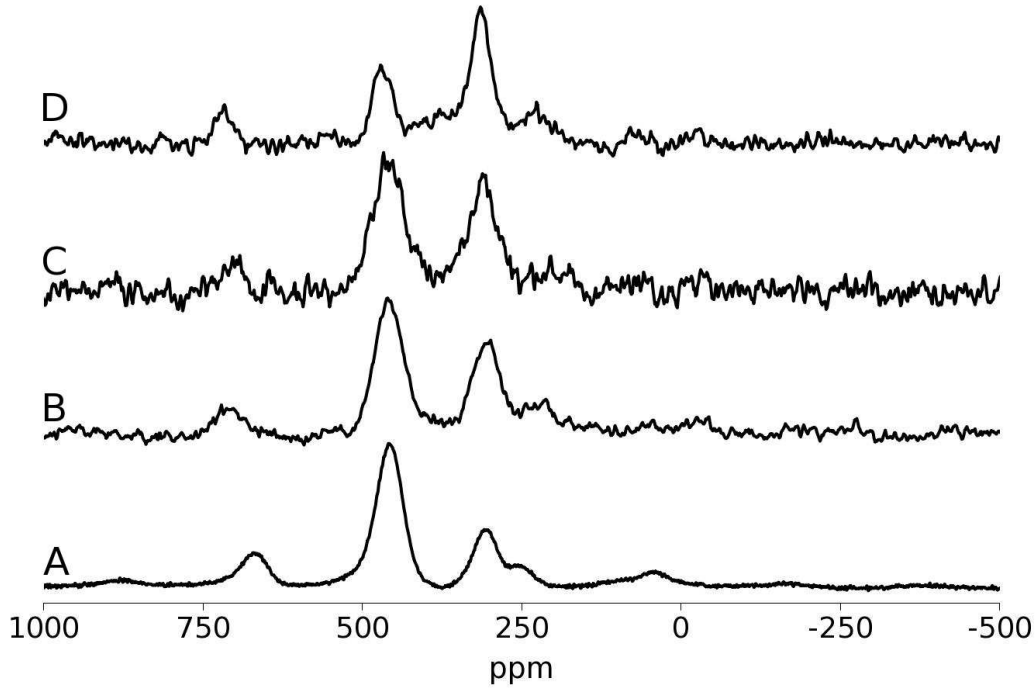

Figure 7.8: ^{17}O NMR spectra of mesoporous tantalum oxide after extra heat treatments at A:- No extra heat treatment, B:-250°C, C:-500°C and D:-750°C

Figure 7.8 shows ^{17}O NMR spectra of mesoporous tantalum oxide which has had various different heat treatments performed on it. There are two sites

throughout the temperature series whose ratio changes with heat treatment (as shown in table 7.5). As the mesoporous structure is lost in mesoporous niobia as the heat treatment is increased it is a reasonable assumption that the mesoporous tantalum oxide is similarly affected. As the peak at approximately 460 ppm reduces in intensity as heat treatment increases, this must be associated with the mesoporous tantalum oxide and the peak at approximately 310 ppm is associated with the amorphous tantalum oxide. This shows that although the mesoporous structure is not completely stable even at 250°C, its breakdown is gradual.

Temperature (°C)	**Peak Position (ppm)±3.0**	**Line Width (Hz)±20**	**% ±5**	**ratio**
un-heated	306.1	1200	28	1
	458.6	1270	72	2.6±0.7
250	306.1	1480	43	1
	459.8	1380	57	1.7±0.3
500	310.4	1330	57	1
	459.8	1520	43	1.3±0.2
750	314.1	970	59	1
	469.0	1110	41	0.7±0.2

Table 7.5: ^{17}O peak parameters for temperature series of mesoporous tantalum oxide

Figure 7.9 shows a heat treatment series on mesoporous titanium oxide. As the mesoporous structure of the niobium oxide has been shown to break down with increasing heat treatment it is reasonable to assume that the same happens with the titanium oxide. Using this assumption it is fair to assume that the peak at approximately 570 ppm is due to the mesoporous phase and that the peak at approximately 380 ppm is due to an amorphous phase. The peak at 570 ppm is also assigned to a OTi_3 unit[103]. This implies that the walls of the mesoporous material are made up of OTi_3 units. The amorphous impurity is also associated with OTi_4[103]. As with the mesoporous tantalum oxide the titanium oxide is not

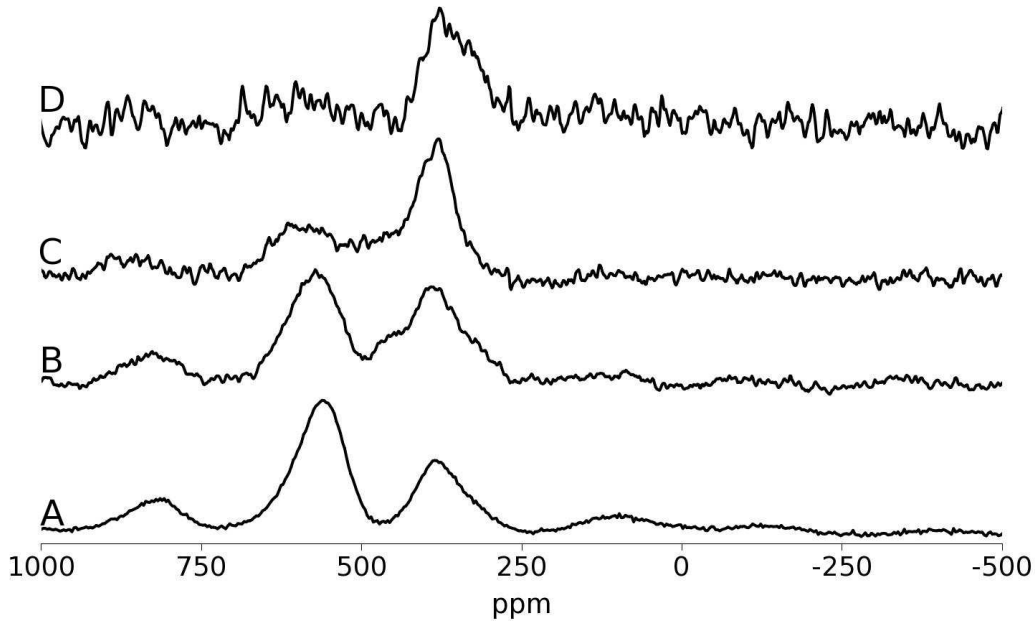

Figure 7.9: ^{17}O NMR spectra of mesoporous titanium oxide after extra heat treatments at A:- No extra heat treatment, B:-250°C, C:-500°C and D:-750°C

stable at 250°C, however the breakdown of the mesoporous structure is gradual. The collapse is almost complete by 750°C.

Temperaute (°C)	**Peak Position (ppm)**	**Line Width (Hz)**	%	**ratio**
un-heated	379.7±2.0	2080±10	41±5	1
	561.6±2.0	2130±10	59±5	1.4±0.3
250	387.1±3.0	2500±20	45±5	1
	573.9±2.0	2705±20	55±5	1.2±0.3
500	387.1±2.0	1640±20	64±5	1
	594.4±5.0	2650±50	36±5	0.6±0.1
750	362.5±5.0	2610±50	71±10	1
	598.5±10.0	4270±100	29±10	0.4±0.2

Table 7.6: ^{17}O peak parameters for temperature series of mesoporous titanium oxide

7.2 Conclusion

The amount and the stability of the mesoporous structure varies between the different metal oxides, with niobium oxide being the most stable and showing the largest proportion of mesoporous structure after having been produced. The tantalum oxide shows the next highest level of stability and proportion of mesoporous structure, and finally the titanium oxide shows approximately $\frac{2}{3}$ of the material as mesoporous structure and has a substantial breakdown by 500°C. The amount of mesoporous structure seen by the ^{17}O MAS NMR is also reflected by the surface areas of the materials as obtained via BET[104]. The niobium oxide has a surface area of 578.6 m^2 g^{-1}, tantalum oxide 556.9 m^2 g^{-1} and titanium oxide 535.0 m^2 g^{-1}. Although these surface areas are large they are less than half that of the mesoporous silica of 1200 m^2 g^{-1}. From the metal oxides, the strength which the amine template is attached to the oxide has little effect on the amount of mesoporous structure or its final stability. However if the mesoporous silica is compared to the other samples, the surface area of the silicate is much larger and the amine has broken down in to NH groups which have attached themselves to various sites in the silicate. The breakdown of the amine groups could be the key to creating mesoporous materials with the maximum surface area. Whether the hydrogen which would come from the broken down amine plays a role in this remains unclear and would require further investigation.

Chapter 8

Tin Tungstates

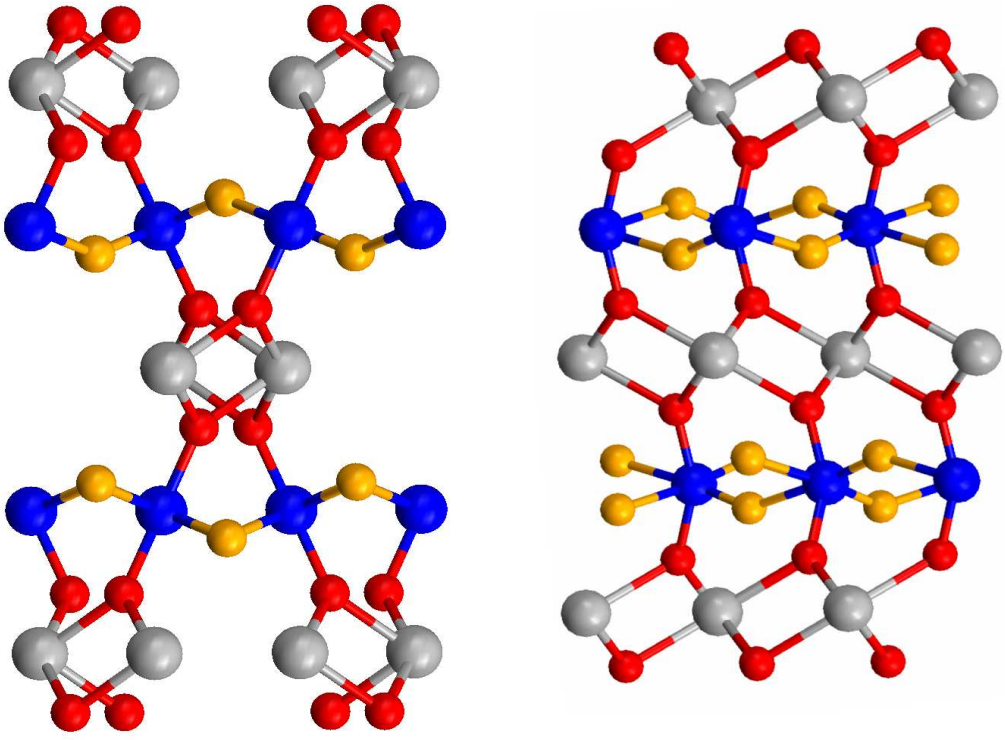

Figure 8.1: Alpha Tin Tungstate structure[9], Grey atoms are tin, Blue are tungsten, Red are oxygen in the O2 position and Orange are oxygen in the O1 position. The two representations of the same structure differ by a 90° rotation.

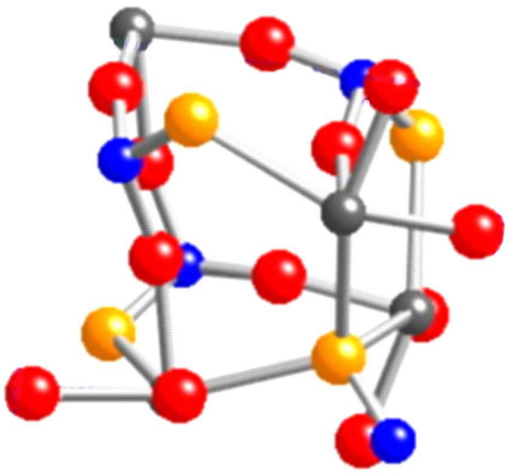

Figure 8.2: Beta Tin Tungstate structure[10], Grey atoms are tin, Blue are tungsten, Red are oxygen in the O2 position and Orange are oxygen in the O1 position.

Tin tungstates were studied due to the strong red crystals that form in the alpha phase of the material. Producing these reliably however proved to be very difficult and it was decided to see if adding sulphur to the system would result in shifting the band gap of the main material of smaller crystals into the red region. Although this failed to have the required result, the information that can be gained from the NMR remains interesting.

The structure of alpha tin tungstate (shown in figure 8.1) is constructed of two different tin units and chains of tungsten linked by two oxygens which interlink the tin units. One tin unit is a pair of tin atoms with four oxygen atoms, each of which have one bond with the tungsten chain. The other tin unit is similar, however instead of all of the oxygen atoms having a bond with each tin in the unit and the tungsten, one of the oxygen atoms has a bond with the unit above it and another oxygen has a bond with the tin unit below it. Beta tin tungstate however has a very different structure (as shown in figure 8.2). The tungsten is tetrahedrally coordinated to oxygen, three of which are connected to tin and one

of which has a partial long range bond of 2.81 Å to three tins. The tin has a very distorted site where three of the oxygens have a oxygen-tin-oxygen bond angle of 113.6° and another oxygen bond which is partial.

8.1 Model Materials

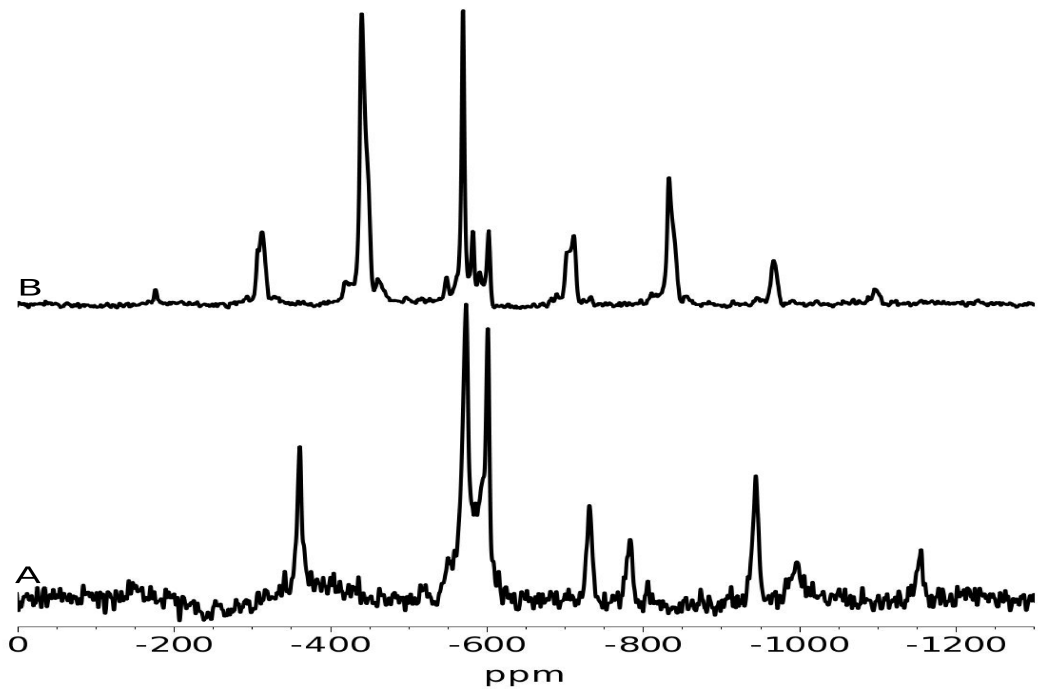

Figure 8.3: ^{119}Sn MAS NMR spectra of A:- Alpha $SnWO_4$ and B:- Beta $SnWO_4$ at 4.79 T

The ^{119}Sn NMR spectra of two model materials are shown in figure 8.3 and have been fitted in figures 8.4 and 8.7. The fitting parameters are shown in tables 8.1 and 8.3. To fit the alpha tin tungstate variable speed MAS was required so that the central line could be determined.

The XRD of the alpha tin tungstate (figure 8.5) shows that the majority of the material is $SnWO_4$, however there is a significant amount of SnO_2 and a

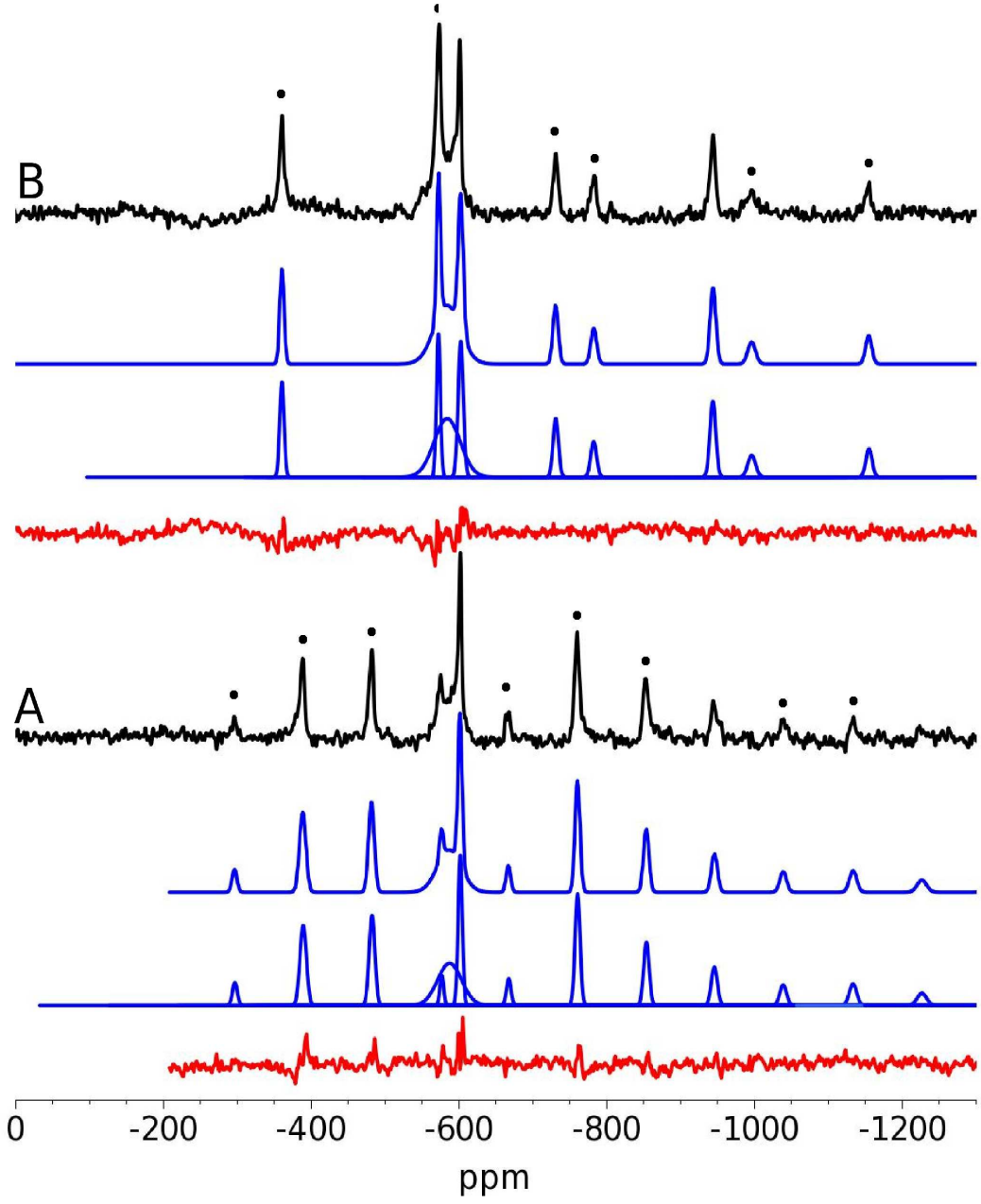

Figure 8.4: ^{119}Sn MAS NMR of Alpha $SnWO_4$ and the fit. Black are the spectra, Blue the total line and individual lines and the Red lines are the difference. Spectrum A was taken spinning at 7.1 kHz and spectrum B was taken at 16 kHz. The lines with a black dot above them are due to spinning side bands, the line at -572.2 ppm in spectra A is only partially due to spinning side bands.

Spinning at 7.1kHz				Spinning at 16kHz			
Site	**%**	**Width(Hz)**	**Shift(ppm)**	**Site**	**%**	**Width(Hz)**	**Shift(ppm)**
	±4.0	**±20**	**±3.0**		**±4.0**	**±20**	**±3.0**
1S	2.3	300	-295.9	1S	9.1	270	-359.6
1S	10.5	400	-389.1	1,3S	12.3	240	-572.2
1S	10.6	360	-482.3	2	15.7	320	-602.4
4	20.6	1490	-587.3	4	33.9	1620	-584.0
1	2.3	230	-576.8	3S	7.0	330	-731.0
2	12.9	260	-601.7	1S	4.6	360	-782.2
1S,3S	2.5	280	-667.3	3	9.8	360	-943.6
1S,3S	11.6	310	-760.5	1S	3.8	470	-996.0
1S,3S	7.2	340	-853.7	3S	3.9	390	-1154.9
3	4.8	380	-945.5				
1S,3S	2.8	420	-1038.7				
1S,3S	3.2	460	-1133.2				
1S,3S	1.4	590	-1226.4				
1S,3S	3.2	580	-1319.6				
1S,3S	3.2	640	-1411.4				

Table 8.1: Line parameters and assignments for fitting of Alpha $SnWO_4$ spinning at 7.1 kHz and 16 kHz

small amount of SnW_3O_9. The XRD of the beta tin tungstate shows that most of the material is beta $SnWO_4$. There is also an impurity which has been assigned as Sn_2TiWO_7, although this in unlikely as the material should not contain any Ti. There are small signs of some alpha $SnWO_4$ and a small amount of SnO_2.

All of the NMR spectra were fitted using Gaussian peaks as ^{119}Sn is spin $\frac{1}{2}$. The fitted peaks were then assigned to either a main site, a spinning side band of a main site or a splitting of the peak due to J-coupled nuclei. The main peaks were first assigned to the alpha and beta tin tungstate either from a single spectrum or using spectra obtained from samples spinning at different rates. After the main peaks were assigned to the other materials, the spinning side bands were marked, along with peaks due to J-coupling. Any other peaks that remained that were of significant intensity could be assigned as a new site or spinning side bands of that site.

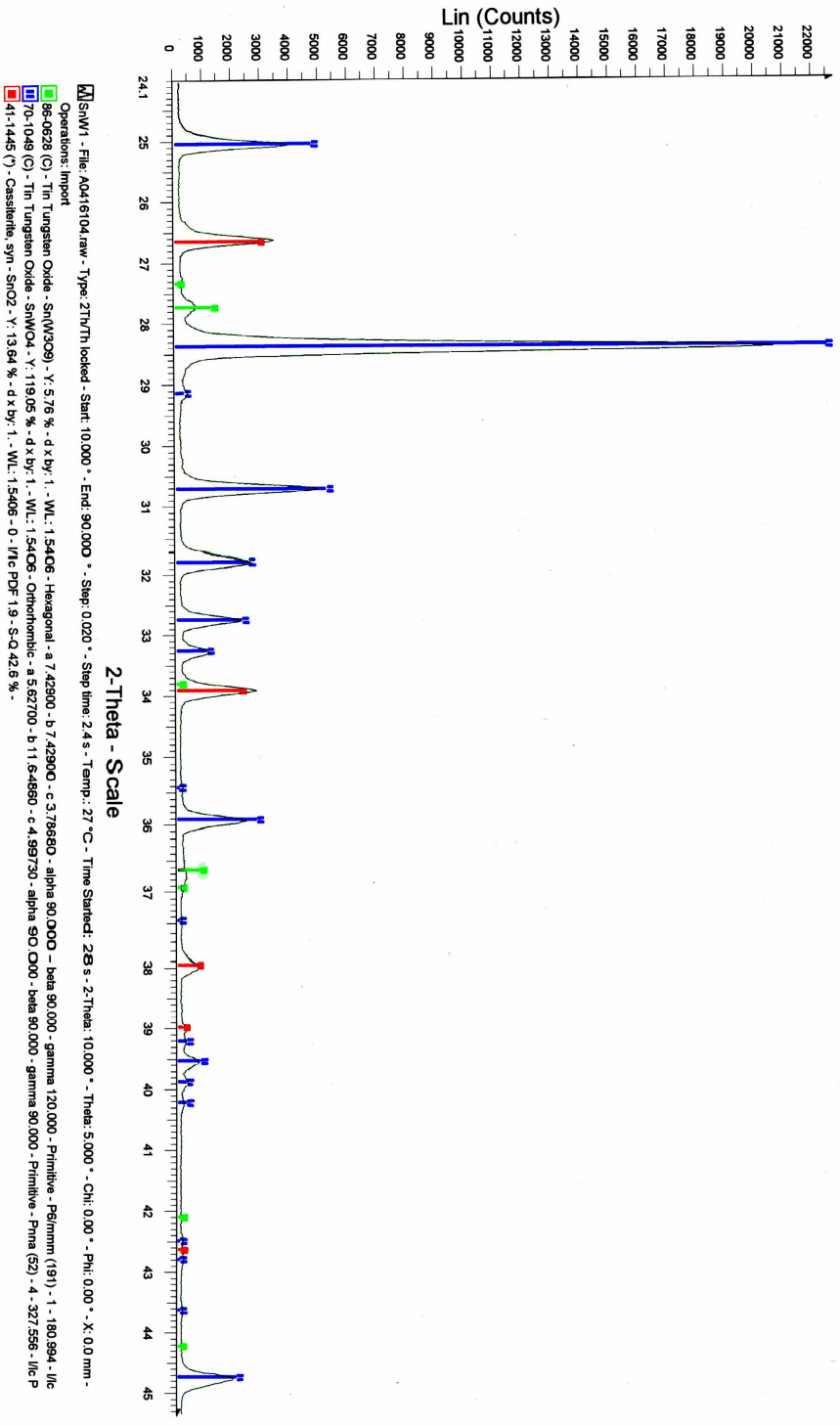

Figure 8.5: XRD of alpha tin tungstate.

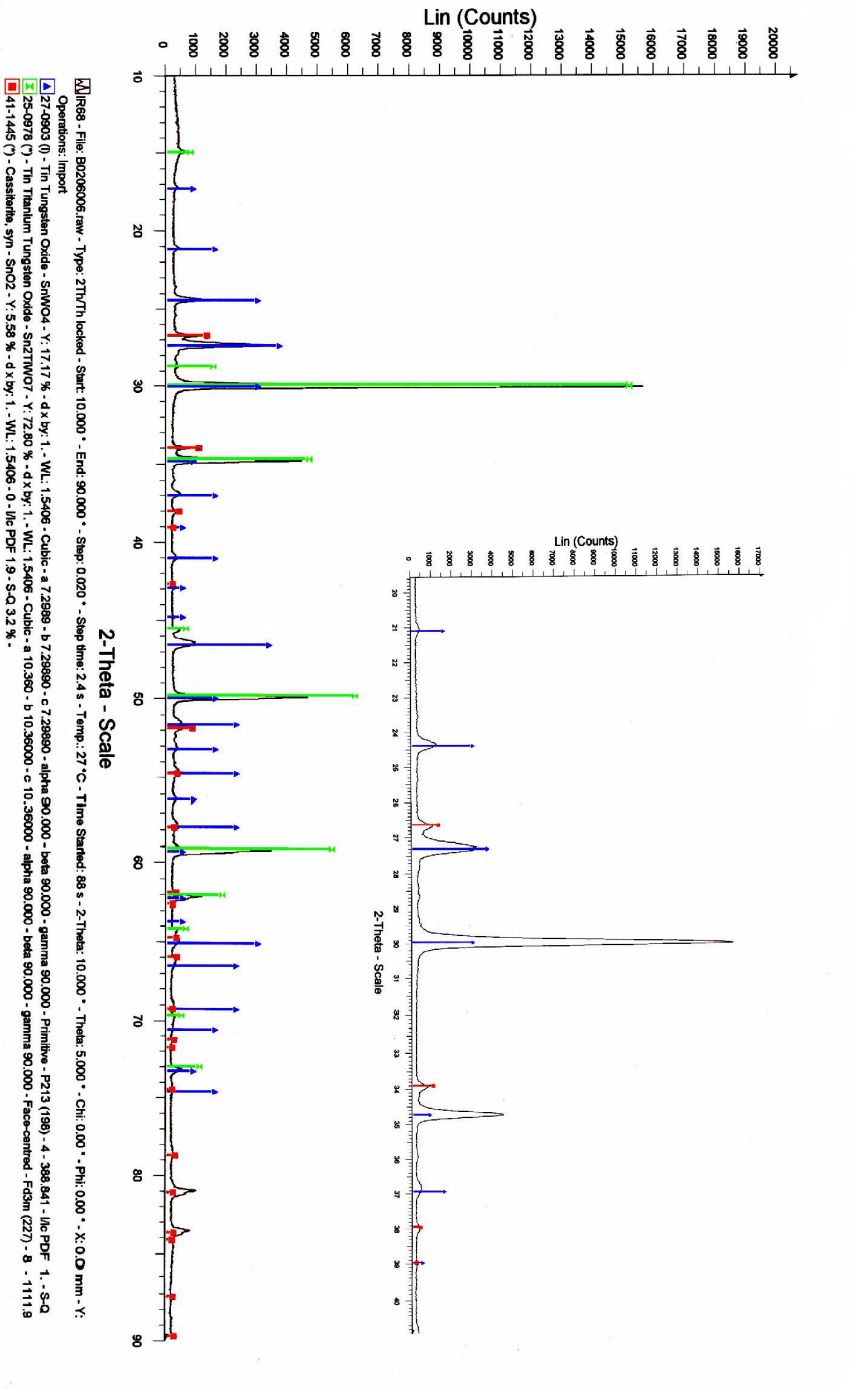

Figure 8.6: XRD of beta tin tungstate. Inset XRD pattern is of the central region of the main XRD pattern expanded with the Sn_2TiWO_7 markers removed.

In the ^{119}Sn NMR spectra for the alpha tin tungstate there are several resonances which are not spinning side bands. The line at -602 ppm is most likely to be due to the SnO_2 impurity in the material and does not appear to have any spinning side bands. The peak at -587 ppm is much broader than any of the other resonances so is likely to be from a separate amorphous impurity, possibly the SnW_3O_9. If it was amorphous it would not be distinct in the XRD pattern as the peaks would be heavily broadened. The resonance at -944 ppm is relatively narrow, however it is outside the normal range of shifts for ^{119}Sn so the origin of this resonance is difficult to determine. It could possibly be due to the alpha tin tungstate, however this is unlikely as the tin should only have one site. The resonance at -574 ppm is therefore due to the alpha tin tungstate. The narrow line implies that is highly ordered and the spinning side bands show that the bonding is asymmetric, which agrees with the structure. From the spinning side band pattern the interaction parameters for the chemical shift anisotropy can be estimated, and are displayed in table 8.2. These parameters could be more accurately obtained from a static spectrum of the sample. Due to the width of the line the amount of time required to obtain a spectrum would be prohibitive.

Site	**Isotropic Shift$\pm$100 (ppm)**	**Span$\pm$100 (ppm)**	**Skew$\pm$0.3**
1	-573	700	0.7
3	-944	760	-0.1

Table 8.2: Estimated interaction parameters for different sites of Alpha $SnWO_4$ as derived from spinning side band pattern from the spectra shown in figure 8.4.

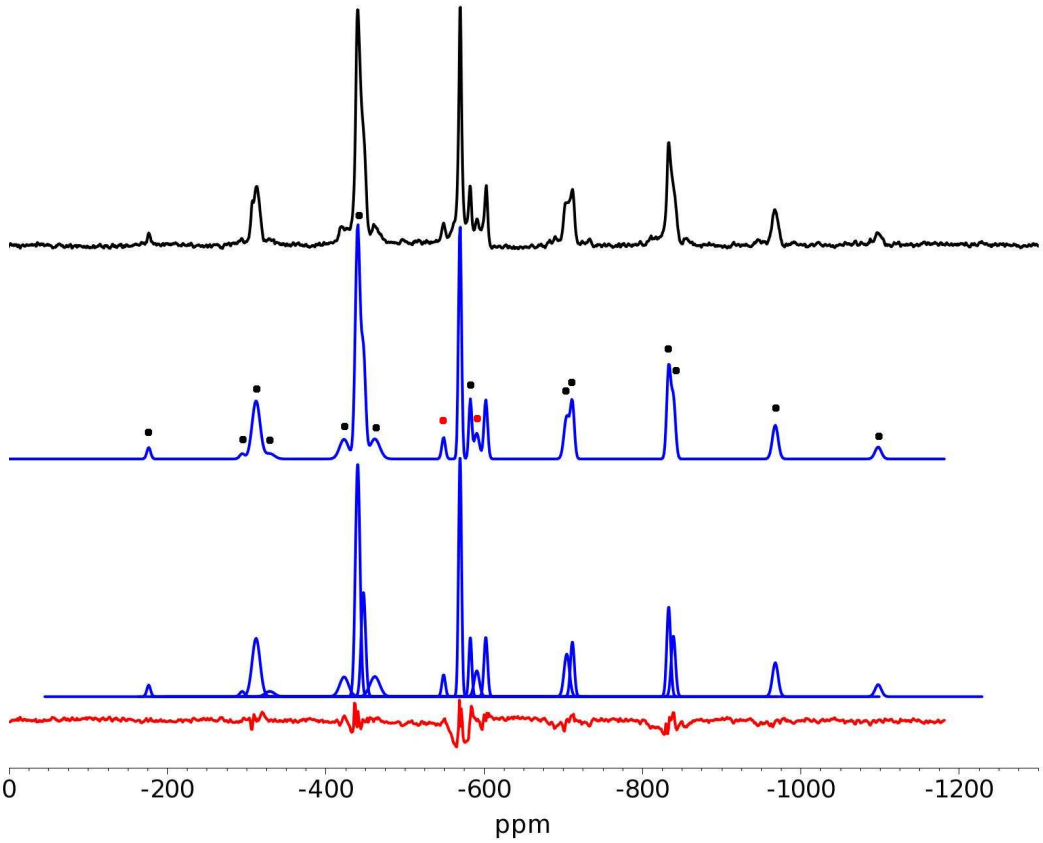

Figure 8.7: ^{119}Sn MAS NMR of Beta $SnWO_4$ and the fit. Black are the spectrum, Blue the total line and individual lines and the Red lines are the difference. The lines with black dots above them are spinning side bands and the lines with red dots above them are due to J-Coupling.

The ^{119}Sn MAS NMR spectrum for the beta $SnWO_4$ is relatively complicated, however the peaks are easily assigned (table 8.3). The peak at -602 ppm is due to a SnO_2 impurity, which shows up in the XRD (figure 8.6). There is no sign of a peak at -587 ppm or -944 ppm which are associated with the alpha tin tungstate. However, these could lie under spinning side bands, or lines associated with J-Coupling. If this is the case the intensity of the peak is very low. From the structure (figure 8.2), there appears to be a single site which is highly distorted. The single distorted site implies there would be a large CSA interaction,

Line Assignment	**Shift (ppm)**	**Width (Hz)**	%
	±3.0	**±10**	**±3.0**
1S,2S	-176.1	218	0.8
1JS	-294.2	283	0.5
1S,2S	-311.8	461	9.0
1JS	-329.2	533	1.0
1JS	-423.0	514	3.4
1S	-440.2	268	21.0
2	-447.4	255	8.9
1JS	-461.8	571	3.9
1J	-548.7	206	1.5
1	-569.4	173	13.9
2S	-582.4	171	3.4
1J	-590.6	305	2.6
3	-602.0	211	4.2
1S	-704.2	314	4.5
2S	-711.3	229	4.2
1S	-832.9	227	6.8
2S	-838.9	250	5.1
1S,2S	-968	332.1	3.8
1S,2S	-1098	365.3	1.5

Table 8.3: Line parameters and assignments for figure 8.7. The "S" in the line assignment stands for the spinning sideband of the main peak and the "J" stands for a peak caused by splitting of the main peak due to J-Coupling.

which matches with a large spinning side band manifold. As with the alpha tin tungstate, despite the predicted single site there are two resonances which can not be explained with normal impurities. The two beta tin tungstate resonances show several interesting features. Both the lines are narrow implying that the beta tin tungstate is highly ordered. The site at -569 ppm is split into three peaks due to J-Coupling.

The J-coupling that is occurring in the tin spectra can be between ^{119}Sn and ^{117}Sn or between ^{119}Sn and ^{183}W. The strength of the J-coupling is unusually strong at 3200±300Hz. Looking at the probabilities of this occurring by the number of bonds and the natural abundance of the isotope, the probability of

the tin-tin J-coupling is approximately 21.2% and the tin-tungsten J-coupling is approximately 14.3%. The J-coupled peaks are approximately 26% of that of the main peak which implies that the tin-tin coupling is the cause of the J-coupled peaks. However the error on the proportion of the J-coupled peaks of the main peak is particularly large due to their small intensity. We therefore can not be certain as to the source of the J-coupling. There is however an additional experiment which could be carried out. If a spin echo is used and the τ time is incremented as for a T_2 measurement, the decay in the signal would be modulated by a cosine wave if homonuclear decoupling is occurring and not modulated if it is not[105].

8.2 Sulphur-Doped Tin Tungstates

The spectra from the model materials and the sulphur doped tin tungstates are shown in figure 8.8. Sample C887-28 (figure 8.8C) shows two sites, the first at -572.9 ppm which shows spinning side bands, J-coupling and is narrow at only 140 Hz wide. The second site, at -299.5 ppm, shows some spinning side bands and is relatively broad at 510 Hz. The site at -299.5 ppm occurs at the same place as SnS and SnO. As C887-28 is a sulphur doped tin tungstate and the peaks do not appear in the model materials it is safe to assume that the peak at -299.5 ppm is SnS. The single narrow line associated with the sulphur doped tin tungstate implies the material has a single site and is highly ordered. As the single site is only 3.5 ppm different from the main site in the beta tin tungstate and also shows J-Coupling it is safe to assume that the C887-28 sample is a beta tin tungstate modified slightly by sulphur.

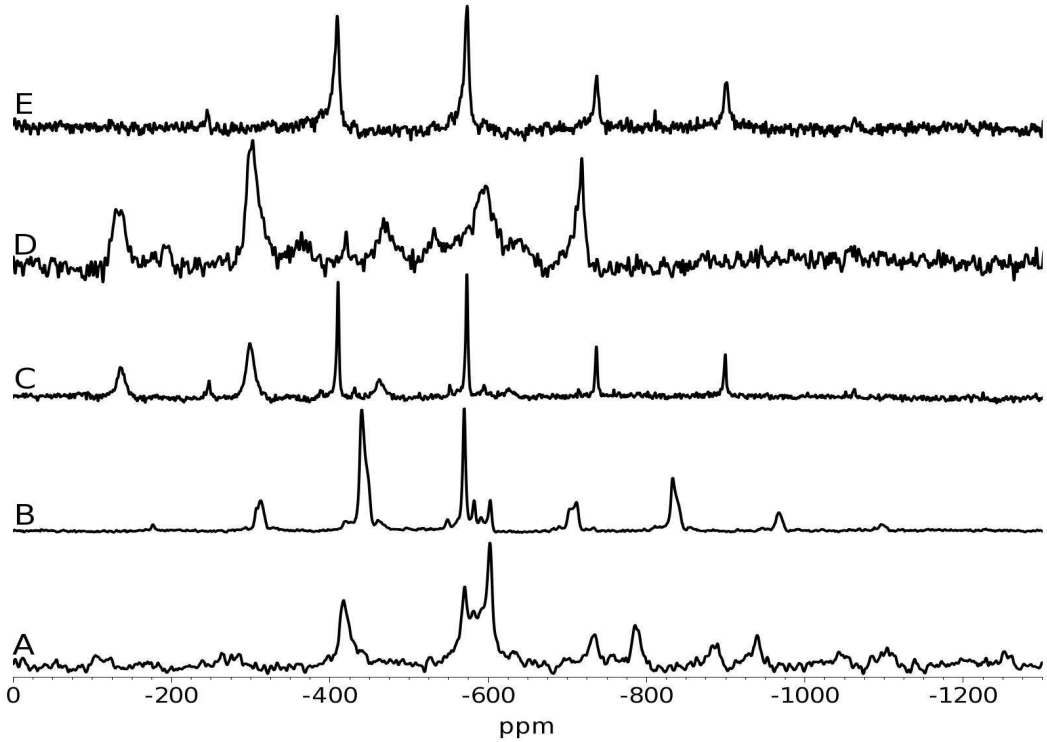

Figure 8.8: ^{119}Sn MAS NMR at 4.79T of A:- Alpha $SnWO_4$, B:- Beta $SnWO_4$, C:-C887-28, D:- C887-29, D:-C887-32B

The solid state ^{119}Sn MAS NMR spectrum obtained from the C887-29 (figure 8.8D) samples shows a series of broad lines. The line at -300.9 ppm can easily be associated with SnS as the shift is correct and the sample is a heavily doped sulphur. The line at -717.3 ppm is similar to the shift seen in SnS_2. The line at -594.2 ppm is significantly broadened so assigning it to either beta or alpha tin tungstate would be difficult, but assigning it as a tin tungstate is likely to be a safe assumption. There is a possible extra site at -312.6 ppm which could be a slightly different phase of SnS. Due to its large shift from the peaks found in the alpha or beta tin tungstate it is relatively safe to assume it is an impurity rather than from the main material. The peak from the tin tungstate is very broad in this material at 1280 Hz which is approximately 7.5 times broader than the model

material. The broad resonance and extra lines imply that high levels of sulphur doping hinder the formation of an ordered tin tungstate.

The solid state ^{119}Sn MAS NMR spectrum for C887-32 (figure 8.8E) shows a relatively simple spectrum with one main peak at -572.7 ppm which can be associated with the beta tin tungstate. The other lines are all spinning sidebands of the central peak. Tin sulphide does not show up in this sample as it has been acid washed to remove any SnS formed during manufacture.

8.3 Conclusion and Further Work

There are a few relatively simple conclusions which can be taken from the results. None of the C886 series of samples appears to form the prefered alpha tin tungstate. The reduced amount of secondary sites in the samples which have had small amounts of sulphur added (C887-28 and C887-32) compared to model material implies that the addition of sulphur helps to form the beta phase of the tin tungstate. The similar line widths between the samples with a small amount of sulphur added and the beta tin tungstate imply that the addition of sulphur does not have any adverse effects such as distortions on the structure. The addition of selenium to the system together with the study of the other NMR active nuclei (^{33}S and ^{183}W) may lead to a better understanding of how the sulphur interacts with the system and allow the design of an alpha phase promoting additive.

Chapter 9

Conclusions and Possible Further Work

QuadFit has already proved a great utility being used by various people in fitting their data. It has had many extensions of its capabilities, necessitating a code which is approximately 7000 lines long. Several extensions and modifications are still required such as an improved iteration algorithm and the ability to fit multiple fields in parallel to get the best single fit.

In an open atmosphere the tin niobate system seems to form the foordite structure at lower firing temperatures and convert to the pyrochlore at higher firing temperatures. The addition of selenium into the system allowed the determination of the site which the sulphur sits, which had not been reported before. The levels of tin metal and tin sulphide linked together to show that during the conversion from foordite to pyrochlore sulphur moves out of the structure and combines with the tin metal, reducing the levels of tin metal, but increasing the levels of tin sulphide. A study of the saturation levels of sulphur in the system would be interesting,

to allow optimisation of the sulphur levels. The study of the firing temperatures and firing times might also allow optimisation of the conversion from foordite to pyrochlore and removal of any tin impurities in the system.

The inclusion of copper and indium into the zinc selenide structure is more complicated than originally thought. The copper and indium remain relatively close to each other. Even the way in which the copper and indium pairs are distributed in the material is not simple. Most of the NMR done in this system is relatively unusual with few papers reporting ^{115}In, ^{63,65}Cu and ^{77}Se NMR in solid state inorganic systems. The techniques and information gained from this system can be used on other similar systems. High resolution multiple quantum techniques could be used on these systems to determine whether there are subtle changes which have not been detected due to the second-order quadrupolar broadening.

The mesoporous oxides presented here show much interesting information. The stability of the mesoporous oxide changes very strongly depending on the cation used in the material. The surface area also seems to be linked to the stability of the oxide. Although various cations will produce mesoporous materials with different stabilities, the ultimate surface areas should be similar and the way the template interacts with the material is at the heart of determining the surface area. The NMR experiments on the nitrogen show that the material with the largest surface area also has the most tightly bound amine and the amine has also broken up into various NH groups. The location of the lost hydrogen of the amine groups is of interest, and a proton spectrum might show whether or not it is still in the system. If the hydrogen is no longer in the system, finding when the hydrogen leaves the system may allow a better design of template for the other systems.

Sulphur appears to act as a promoter of the beta form of tin tungstate

over the alpha phase. The sulphur also does not seem to adversely affect the tin site in the material, although the location of the sulphur in the structure remains unknown. The addition of selenium to the system along with the study of the other NMR active nuclei (^{33}S and ^{183}W) may lead to a better understanding of how sulphur interacts with the system and allow the design of an alpha phase promoting additive.

This thesis clearly demonstrates that multinuclear solid state NMR is an important component technique in characterising inorganic materials.

Appendix A

Other Materials Studied

A.1 Doped Ni-Al Hydroxycarbonates

Doped Ni-Al Hydroxycarbonates are catalysts for hydrogenation of edible oils. During the hydrogenation of oils two forms of fatty acids are produced. The first form, known as the cis form, is wanted while the second, trans, form is not wanted. The study of the systems was hoped to shed some light on how doping the system changes the levels of trans fatty acids (TFAs) in the system and thus how to improve the catalyst to reduce these levels. A study of the current catalysts used along with doped varieties and a precursor was conducted. However the usual period of a ^{27}Al MAS NMR experiment is up to a couple of hours and these experiments took approximately 24 hours each. As the experiments were taking excessive amounts of time a quantitative study was conducted of one of the materials which showed that we were seeing approximately 0.01% of the aluminium

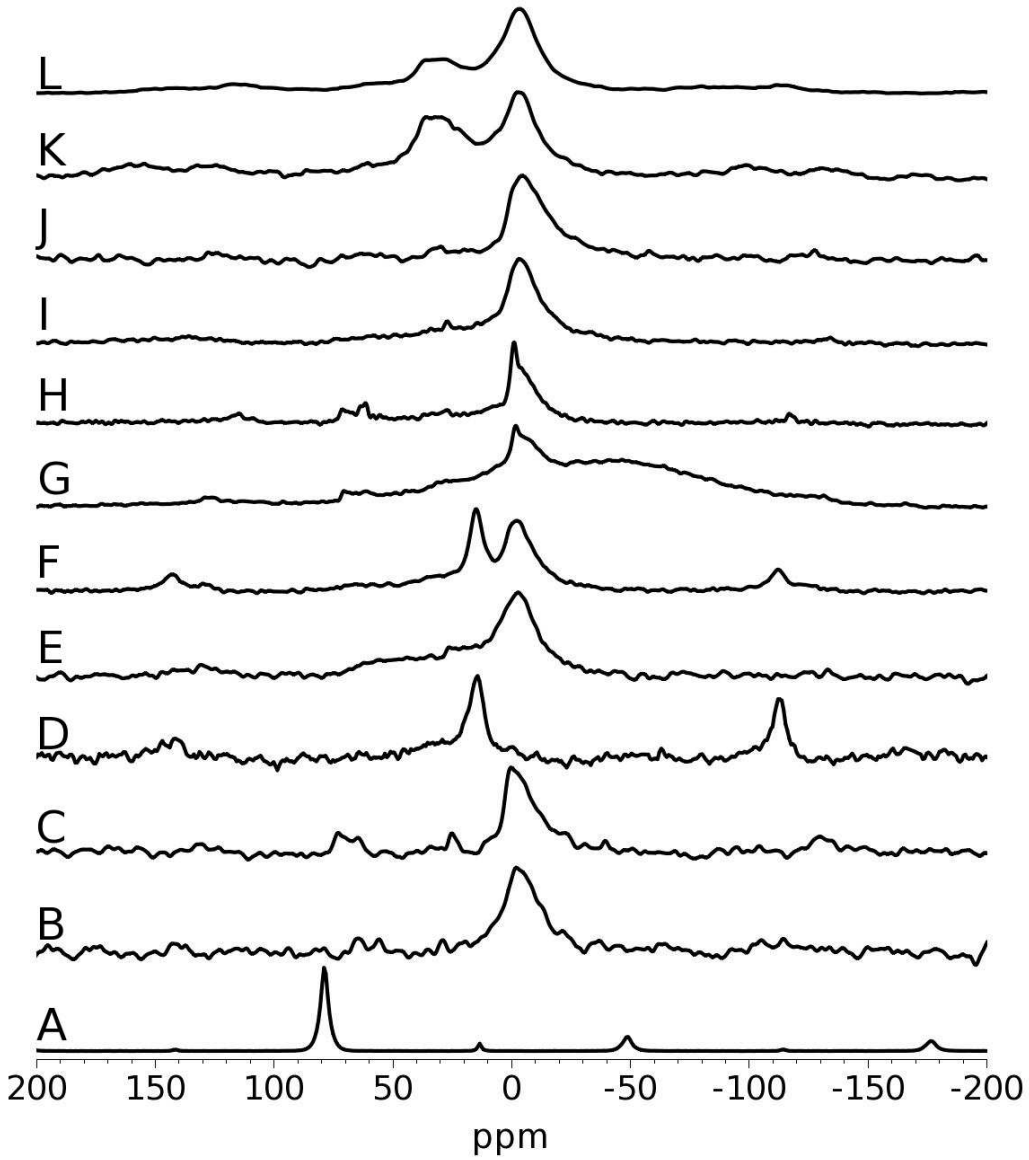

Figure A.1: ^{27}Al MAS NMR at 14.1T of A:-Sodium Aluminate, B:-Pricat 9920, C:-Pricat 9925, D:-Pricat 9925 Reduced at 600°C, E:-ZrR430, F:- ZrR600, G:-ZrF430, H:-ZrF600, I:-CeR430, J:-CeR600, K:-CeF430 and L:-CeF600.

expected. With a more careful look at the system it was realised that the nickel which is sitting on the alumina backbone has been reduced and is thus paramagnetic. The paramagnetic nickel interacts with the aluminium making the signal too broad to observe, hence why only 0.01% of the aluminium was detectable. The

information gained from this part of the experiment is that approximately 99.99% of the alumina backbone is closely associated with reduced nickel.

Figure A.1 shows a stack plot of all of the samples run. It can be seen that none of the sodium aluminate precursor is visible in the final material and that most of the aluminium which is still visible is AlO_6 with a small amount of AlO_5 and only possible traces of AlO_4.

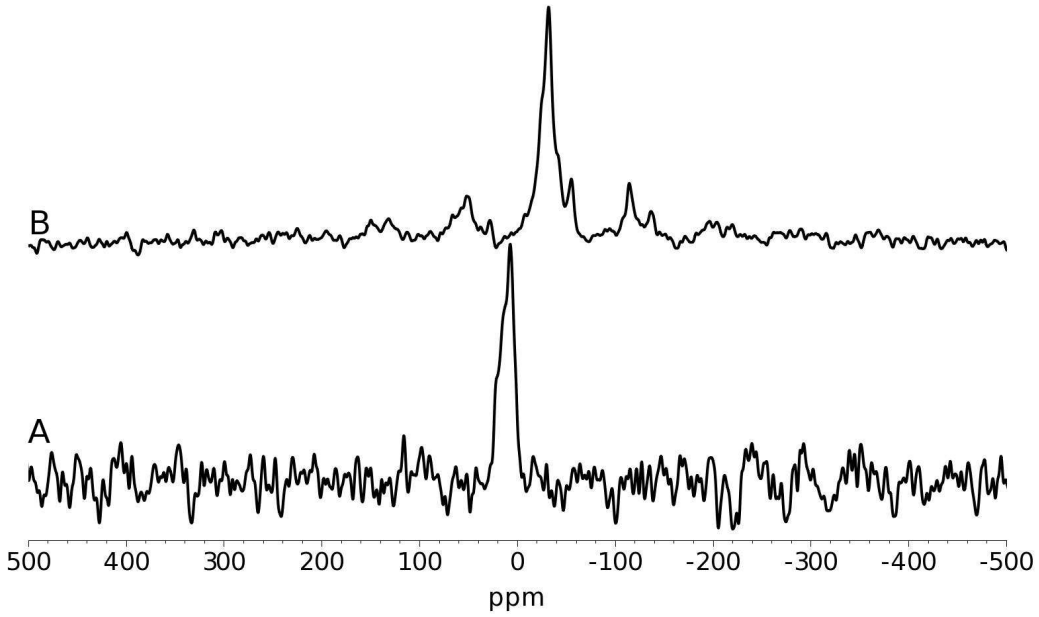

Figure A.2: ^{31}P MAS NMR at 8.46T of A:-CP325 + P Modifier Fresh and B:-CP325 + P Modifier Used

Another method of changing the catalyst is to treat the catalyst with a phospholipid. ^{31}P MAS NMR was performed on the catalyst both before and after it had been used to see if any differences were observable. There is a change to lower shifts, distinct sites and narrower lines. The changes imply that after use the phosphorus in the system has formed in a new more ordered phase. As a qualitative measure the signal from the phosphorus has also increased after the catalyst is used. This implies that some of the phosphorus has moved away from

active nickel sites.

A.1.1 Conclusion and Further Work

The amount of information that can be gained from the systems using conventional NMR is limited due to the paramagnetic interaction from the nickel. Any information gained from the lack of a signal needs to be interpreted carefully as there are many effects which can cause this. Although the study for this catalyst produced limited results the techniques can be used on other catalysts where the active metal is not paramagnetic. A further possibility to gain information is to get a signal from the nickel directly[106], using the internal field of the metal. This could give an interesting insight as the signal would be directly from the active site in the catalyst.

A.2 Enamels

Traditional purple and red enamels are difficult to produce with any reproducibility of colour. New enamels are being researched with Johnson Matthey which rely on colloidal gold and silver to produce a pink colour. These enamels can reliably produce colours, however their colour range is relatively small. A study into how the colour being produced by the pigment is being undertaken and with the ultimate aim to produce an enamel with a larger colour range.

Figure A.3 shows ^{119}Sn MAS NMR of the RU3386 series of samples. None of these samples have been through the ink preparation. However, apart from that they have been through the whole manufacture process. The RU3386-III-400 sample is a working enamel, where as RU3386-III-340, which has had a reduced

intermediate firing temperature, and RU3386-I-400, which has had a reduced mixing period, do not produce the desired colour. The spectrum clearly shows that the tin is in the form of SnO_2 and further studies did not show any tin metal in the materials. There is broadening of the RU3386-III-340 peak which is indicative of more disorder in the material, however the RU3386-I-400 peak is narrower than the RU3386-III-400 peak. So no conclusion can be drawn regarding the order of the material from the tin point of view and its ability to produce the desired colour.

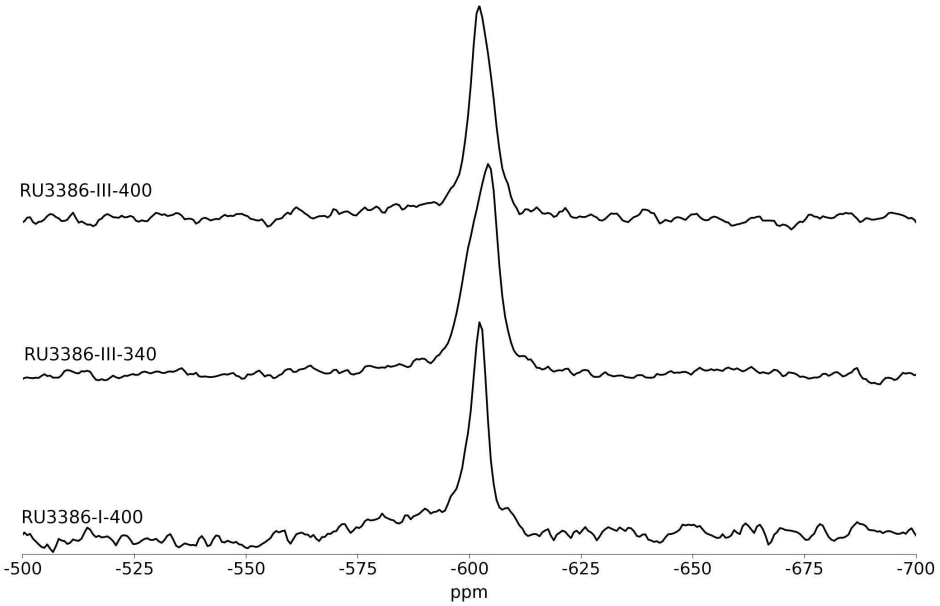

Figure A.3: ^{119}Sn MAS NMR spectra of RU3386 series of samples

Figure A.4 shows ^{119}Sn MAS NMR spectra of the RU3389 series of enamels, all of which produce the desired colour. RU3389-700,900 have both been through the whole manufacture process. The only difference between the two is the firing temperature onto the ceramic, where 700°C and 900°C are the limits between which the enamel produces the desired colour. The sample RU3389-9f has been fired but without going through the ink preparation and ff is the enamel after the

mixing process. Again the spectrum shows that the tin is in the SnO_2 form and again further work showed no tin metal in the enamel. The RU3389-9f,ff and 700 samples all show very similar shifts and line widths, so from the tins perspective view the system has changed very little. The RU3389-900 sample on the other hand shows a significant broadening which could be due to a splitting in the line. The resulting conclusion is that either there is a reduction in the order in the material or the gold or silver is closely associating with some of the tin causing a slight change in the shift.

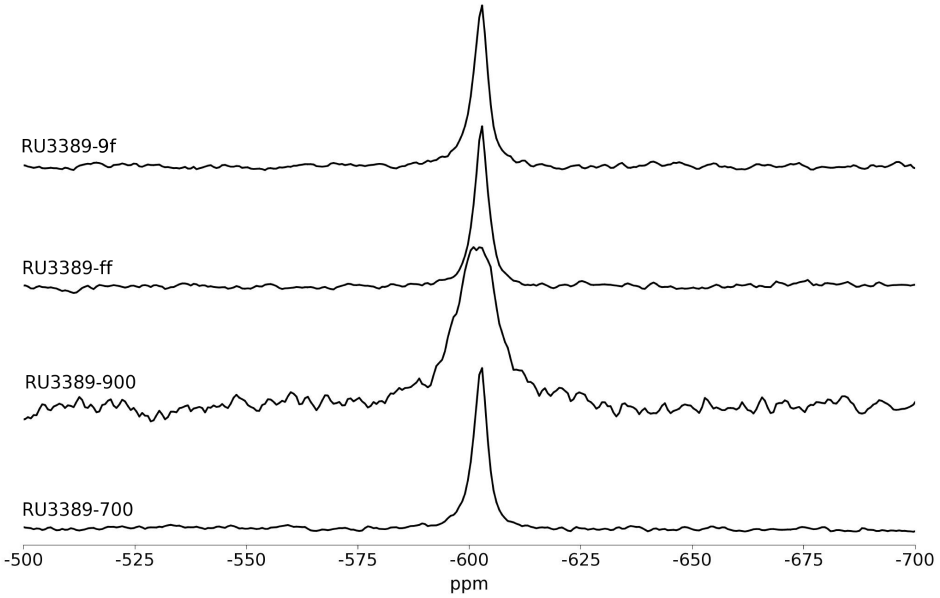

Figure A.4: ^{119}Sn MAS NMR spectra of RU3389 series of samples

Figure A.5 shows STEM images of sample RU3389-710. The images are the amount of signal received from different elements in the material. The STEM images show that the tin, oxygen and silver are associated with each other. The gold seems to be associated with various regions around the outside where the amount of signal from the tin decreases slightly and the signal from the silver increases slightly. The signal from the silicon seems to fill the gaps between the

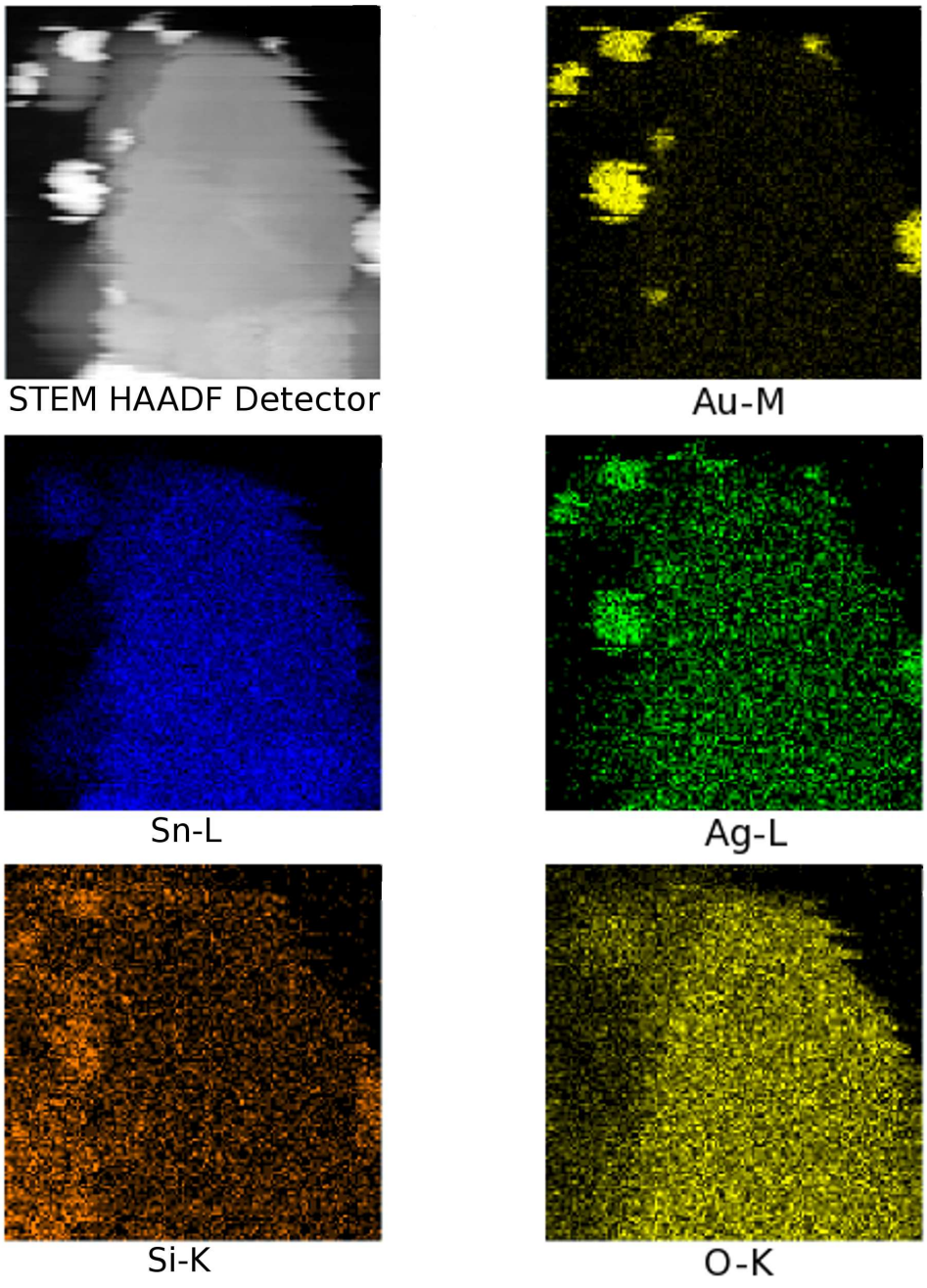

Figure A.5: STEM images of RU3389-710 of various elements

particles and is therefore likely to be the glass frit which holds the pigment particles together.

Figures A.6 and A.7 show X-ray Photoelectron Spectroscopy (XPS) data

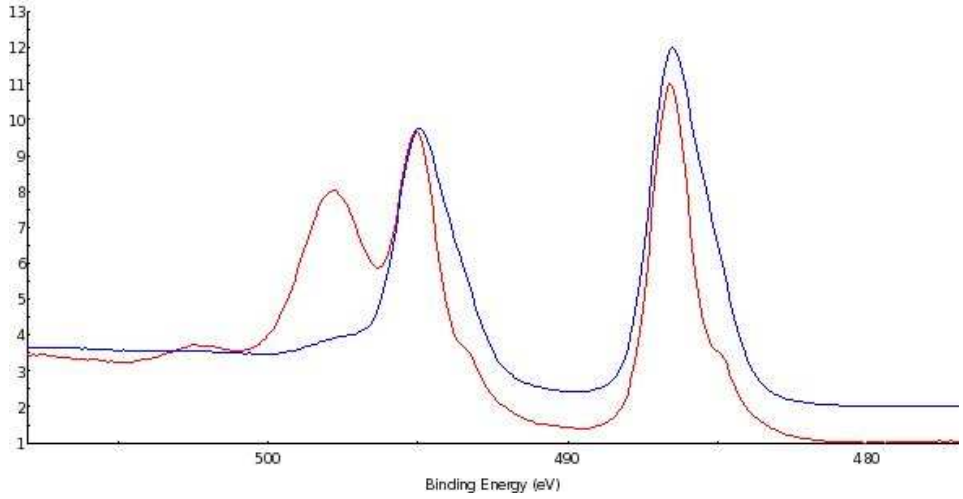

Figure A.6: Tin XPS of tin 3d region. Red line is sample RU3389-900 and Black line is sample RU3389-710

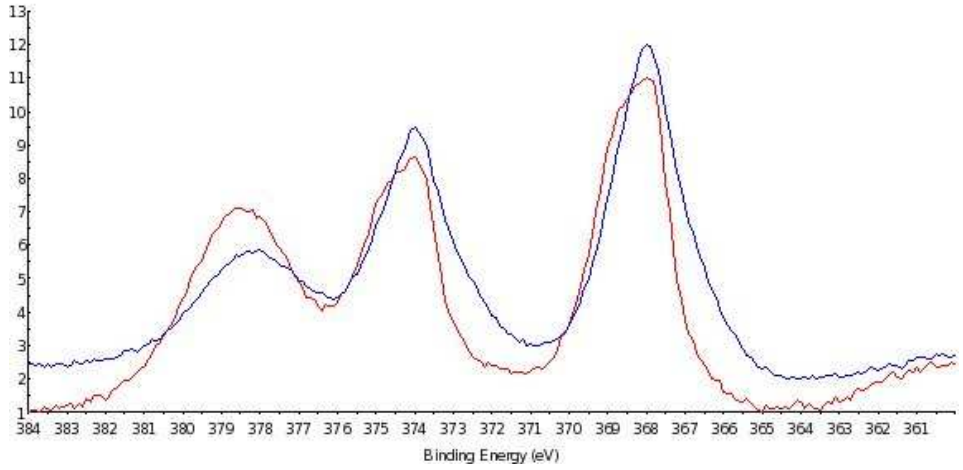

Figure A.7: Silver XPS of silver 3d region. Red line is sample RU3389-900 and Black line is sample RU3389-710

from tin and silver containing regions respectively. The silver XPS data shows three different peaks, which implies that the silver is in three different oxidation states, most probably in the form of silver metal, AgO and AgO_2. There is little difference between the two lines apart from slight changes in the width and intensity of the peaks. This implies that the silver environment does not change significantly

over the range of firing temperatures which result in the desired colour. The tin XPS data also shows three peaks. The NMR only shows SnO_2, so the three peaks in the XPS must be due to different next nearest neighbours of the tin. There is a significant change between the two samples, with one of the peaks vanishing at lower temperature. The addition of another peak in the tin XPS data is accompanied by an increase in the line width in the ^{119}Sn NMR spectrum. This implies that they are linked, and the site associated with the peak at 498eV in the XPS data is sufficiently chemically different that it is showing up in the NMR data. As there is obviously a change in the tin site though the firing range, this shows that the tin sites are not critical to the colour of the enamel.

A.2.1 Conclusion and Further Work

The NMR results show that there is little change in the tin site depending on whether the enamel produces the desired colour. The NMR results also show that there is little or no tin metal in the system. The features in the tin spectra where the line starts to split can be seen in the XPS data, showing that there is definitely some change. This change does not seem to affect the final result. The most information is provided by the STEM images which show how the different elements are associated with each other. This gives an insight that it may be the way in which the silver and gold interact on the surface of the material which defines the final colour. To get a full picture of the materials, a full set of STEM and XPS information would be required. Spectra from ^{109}Ag and ^{197}Au, although difficult to acquire, would allow the way that gold and silver interact to be examined.

Appendix B

Experimental Parameters

Figure	Nucleus	Sample	Field (T)	Probe	Spinning Rate (kHz)	Larmor Frequency (MHz)	Number Acquisitions	Pulse Delay (s)	Pulse Sequence	Pulse Lengths / Delays (μs)
5.3A	^{93}Nb	$Sn_2Nb_2O_7$	14.1	5mm Bruker Static	-	146.7	432	1	echo	0.5-25-0.5-20
5.3B	^{93}Nb	$Sn_2Nb_2O_7$	14.1	1.8mm Samoson	40	146.7	1488	3	echo	0.6-25-0.6-20
5.3C	^{93}Nb	$Sn_2Nb_2O_7$	18.8	4mm Varian	-	195.7	880	3	echo	0.6-40-0.6-35
5.4A	^{93}Nb	$SnNb_2O_6$	14.1	5mm Bruker Static	-	146.7	752	3	echo	0.6-25-0.6-20
5.4B	^{93}Nb	$SnNb_2O_6$	18.8	4mm Varian	-	195.7	896	3	echo	0.6-40-0.6-35
5.4C	^{93}Nb	$SnNb_2O_6$	14.1	1.8mm Samoson	40	146.7	18832	3	echo	0.6-25-0.6-20
5.4D	^{93}Nb	$SnNb_2O_6$	18.8	2.5mm Varian	27.5	195.4	1800	1	1 Pulse	1
5.5A	^{119}Sn	$SnNb_2O_6$	4.8	4mm Doty	14	76.1	34140	10	1 Pulse	4
5.5B	^{119}Sn	$Sn_2Nb_2O_7$	4.8	4mm Doty	12	76.1	11056	20	1 Pulse	4
5.5C	^{119}Sn	SnO_2	4.8	4mm Doty	12	76.1	1200	20	1 Pulse	4
5.5D	^{119}Sn	SnO	4.8	4mm Doty	12	76.1	1000	20	1 Pulse	4
5.5E	^{119}Sn	SnSe	4.8	4mm Doty	12	76.1	8140	20	1 Pulse	4
5.5F	^{119}Sn	SnS	4.8	4mm Doty	15	76.1	3304	20	1 Pulse	4
5.5G	^{119}Sn	SnS_2	4.8	4mm Doty	15	76.1	133	20	1 Pulse	4
5.6A	^{93}Nb	T600	14.1	3.2mm Varian	20	146.7	9200	0.2	echo	1.5-50-3.0-18
5.6B	^{93}Nb	T700	14.1	3.2mm Varian	20	146.7	9200	0.2	echo	1.5-50-3.0-18
5.6C	^{93}Nb	T800	14.1	3.2mm Varian	20	146.7	9200	0.2	echo	1.5-50-3.0-18
5.6D	^{93}Nb	T900	14.1	3.2mm Varian	20	146.7	9200	0.2	echo	1.5-50-3.0-18
5.6E	^{93}Nb	HCl900Se	14.1	3.2mm Varian	20	146.7	9200	0.2	echo	1.5-50-3.0-18
5.6F	^{93}Nb	Amm900Se	14.1	3.2mm Varian	20	146.7	9200	0.2	echo	1.5-50-3.0-18
5.7A	^{119}Sn	F600	4.8	4mm Doty	12	76.1	11000	7	1 Pulse	4
5.7B	^{119}Sn	M600	4.8	4mm Doty	12	76.1	15000	7	1 Pulse	4
5.7C	^{119}Sn	T600	4.8	4mm Doty	12	76.1	10000	7	1 Pulse	4

Table B.1: Experimental parameters for spectra shown in Chapter 5. The sample names are explained in section 3.1.1

Figure	Nucleus	Sample	Field (T)	Probe	Spinning Rate (kHz)	Larmor Frequency (MHz)	Number Acquisitions	Pulse Delay (s)	Pulse Sequence	Pulse Lengths / Delays (μs)
5.8A	^{93}Nb	F600	14.1	3.2mm Varian	20	146.7	1840	0.2	echo	1.5-50-3.0-18
5.8B	^{93}Nb	M600	14.1	3.2mm Varian	20	146.7	5280	0.2	echo	1.5-50-3.0-18
5.8C	^{93}Nb	T600	14.1	3.2mm Varian	20	146.7	9200	0.2	echo	1.5-50-3.0-18
5.9 600	^{93}Nb	F600	14.1	3.2mm Varian	20	146.7	9200	0.2	echo	1.5-50-3.0-18
5.9 700	^{93}Nb	F700	14.1	3.2mm Varian	20	146.7	4512	0.2	echo	1.5-50-3.0-18
5.9 800	^{93}Nb	F800	14.1	3.2mm Varian	20	146.7	4512	0.2	echo	1.5-50-3.0-18
5.9 900	^{93}Nb	F900	14.1	3.2mm Varian	20	146.7	4672	0.2	echo	1.5-50-3.0-18
5.9 900Se	^{93}Nb	F900Se	14.1	3.2mm Varian	20	146.7	4938	0.2	echo	1.5-50-3.0-18
5.10 600	^{93}Nb	M600	14.1	3.2mm Varian	20	146.7	5320	0.2	echo	1.5-50-3.0-18
5.10 700	^{93}Nb	M700	14.1	3.2mm Varian	20	146.7	3372	0.2	echo	1.5-50-3.0-18
5.10 800	^{93}Nb	M800	14.1	3.2mm Varian	20	146.7	8190	0.2	echo	1.5-50-3.0-18
5.10 900	^{93}Nb	M900	14.1	3.2mm Varian	20	146.7	9352	0.2	echo	1.5-50-3.0-18
5.10 900Se	^{93}Nb	M900Se	14.1	3.2mm Varian	20	146.7	9200	0.2	echo	1.5-50-3.0-18
5.11 F600	^{119}Sn	F600	4.8	4mm Doty	12	76.1	11212	7	1 Pulse	4
5.11 F700	^{119}Sn	F700	4.8	4mm Doty	12	76.1	29120	7	1 Pulse	4
5.11 F800	^{119}Sn	F800	4.8	4mm Doty	12	76.1	36240	7	1 Pulse	4
5.11 F900	^{119}Sn	F900	4.8	4mm Doty	12	76.1	23187	7	1 Pulse	4
5.11 F900Se	^{119}Sn	F900Se	4.8	4mm Doty	12	76.1	42134	7	1 Pulse	4
5.13	^{119}Sn	F700 (metal)	4.8	4mm Doty	12	76.8	6000	0.1	echo	2-83.3-4-23.3

Table B.2: Experimental parameters for spectra shown in chapter 5. The entry with "metal" in brackets under the name is for the metal part of the spectra and the parameters for the rest of the spectra are shown elsewhere in the table. The sample names are explained in section 3.1.1

Figure	Nucleus	Sample	Field (T)	Probe	Spinning Rate (kHz)	Larmor Frequency (MHz)	Number Acquisitions	Pulse Delay (s)	Pulse Sequence	Pulse Lengths / Delays (μs)
6.3 A	^{77}Se	SeO_2	8.45	4mm Bruker	12	68.7	3762	5	echo	3-83.3-6-43.3
6.3 B	^{77}Se	Na_2SeO_4	8.45	4mm Varian	12	68.7	2000	1	1 Pulse	3
6.3 C	^{77}Se	K_2SeO_4	8.45	4mm Varian	12	68.7	96	600	1 Pulse	3
6.4 A	^{77}Se	ZnSe	8.45	4mm Doty	12	68.6	103	600	1 Pulse	2
6.4 B	^{77}Se	CdSe	8.45	4mm Doty	12	68.6	8	600	1 Pulse	2
6.5	^{77}Se	$NbSe_2$	8.45	4mm Doty	12	68.9	33568	0.1	echo	3-83.3-6-43.3
6.6,6.7 A	^{65}Cu	$CuInSe_2$	7.05	5mm Bruker Static	-	85.2	30000	0.5	echo	0.6-25-0.6-20
6.6,6.7 B	^{65}Cu	$CuInSe_2$	9.4	5mm Bruker Static	-	113.6	30000	0.5	echo	0.6-25-0.6-20
6.6,6.7 C	^{65}Cu	$CuInSe_2$	14.1	5mm Bruker Static	-	170.5	8304	0.5	echo	0.6-25-0.6-20
6.6,6.7 D	^{65}Cu	$CuInSe_2$	18.8	4mm Varian	-	227.0	18116	0.5	echo	0.6-25-0.6-20
6.8 A	^{65}Cu	CuInSSe	7.05	5mm Static Bruker	-	85.2	30000	0.5	echo	0.6-25-0.6-20
6.8 B	^{65}Cu	CuInSSe	9.4	5mm Static Bruker	-	113.6	30000	0.5	echo	0.6-25-0.6-20
6.8 C	^{65}Cu	CuInSSe	14.1	5mm Static Bruker	-	170.5	19536	0.5	echo	0.6-25-0.6-20
6.8 D	^{65}Cu	CuInSSe	18.8	4mm Varian	-	227.5	30000	0.5	echo	0.6-25-0.6-20
6.9 A	^{115}In	$CuInSe_2$	4.8	4mm Doty	-	44.7	45008	0.1	echo	2-71.4-4-21.4
6.9 B	^{115}In	$CuInSe_2$	8.45	4mm Doty	-	78.8	2006	0.1	echo	1-50-2-45
6.9 C	^{115}In	$CuInSe_2$	14.1	2.5mm Bruker	-	131.5	1759	0.1	echo	0.5-33.3-1-23.3
6.9 D	^{115}In	$CuInSe_2$	14.1	2.5mm Bruker	30	131.5	451	0.1	echo	0.5-33.3-1-23.3
6.9 E	^{115}In	$CuInSe_2$	18.8	4mm Varian	-	175.2	5152	0.1	echo	0.9-25-0.9-20

Table B.3: Experimental parameters for spectra shown in chapter 6. The sample names are explained in section 3.1.3

Figure	Nucleus	Sample	Field (T)	Probe	Spinning Rate (kHz)	Larmor Frequency (MHz)	Number Acquisitions	Pulse Delay (s)	Pulse Sequence	Pulse Lengths / Delays (μs)
6.10 A	^{115}In	CuInSSe	4.8	4mm Doty	-	44.7	2836	0.1	echo	2-71.4-4-21.4
6.10 B	^{115}In	CuInSSe	8.45	4mm Doty	-	78.8	2000	0.1	echo	1-50-2-45
6.10 C	^{115}In	CuInSSe	14.1	2.5mm Bruker	-	131.5	143	0.1	echo	0.5-33.3-1-23.3
6.10 D	^{115}In	CuInSSe	18.8	4mm Varian	-	175.2	10560	0.1	echo	0.9-25-0.9-20
6.12,6.13 A	^{77}Se	2%CuInSSeFF	4.8	4mm Doty	12	39.0	280	600	1 Pulse	4
6.12,6.13 B	^{77}Se	2%$CuInSe_2$	4.8	4mm Doty	12	39.0	264	600	1 Pulse	4
6.12,6.13 C	^{77}Se	2%$CuInSe_2$FF	4.8	4mm Doty	12	39.0	560	600	1 Pulse	4
6.12,6.13 D	^{77}Se	5%$CuInSe_2$	4.8	4mm Doty	12	39.0	850	600	1 Pulse	4
6.14 A	^{63}Cu	$CuInSe_2$	14.1	3.2mm Varian	20	159.2	1804	0.2	1 Pulse	1
6.14 B	^{63}Cu	CuInSSe	14.1	3.2mm Varian	20	159.2	1948	0.2	1 Pulse	1
6.14 C,6.15 A	^{63}Cu	2%CuInSSeFF	14.1	3.2mm Varian	20	159.2	7376	0.2	1 Pulse	1
6.14 D,6.15 B	^{63}Cu	2%$CuInSe_2$	14.1	3.2mm Varian	20	159.2	11912	0.2	1 Pulse	1
6.14 E,6.15 C	^{63}Cu	2%$CuInSe_2$FF	14.1	3.2mm Varian	20	159.2	3908	0.2	1 Pulse	1
6.14 F,6.15 D	^{63}Cu	5%$CuInSe_2$	14.1	3.2mm Varian	20	159.2	18224	0.2	1 Pulse	1
6.16,6.17 A	^{115}In	2%$CuInSe_2$FF	8.45	4mm Doty	-	78.6	400000	0.2	echo	1-50-2-45
6.16,6.17 B	^{115}In	2%$CuInSe_2$	8.45	4mm Doty	-	78.6	309056	0.2	echo	1-50-2-45
6.16,6.17 C	^{115}In	2%CuInSSeFF	8.45	4mm Doty	-	78.6	403760	0.2	echo	1-50-2-45
6.16,6.17 D	^{115}In	5%$CuInSe_2$	8.45	4mm Doty	-	78.8	423872	0.2	echo	1-50-2-45
6.16,6.17 E	^{115}In	$CuInSe_2$	8.45	4mm Doty	-	78.8	7760	0.2	echo	1-50-2-45
6.16,6.17 F	^{115}In	CuInSSe	8.45	4mm Doty	-	78.8	2000	0.2	echo	1-50-2-45

Table B.4: Experimental parameters for spectra shown in chapter 6. The sample names are explained in section 3.1.3

Figure	Nucleus	Sample	Field (T)	Probe	Spinning Rate (kHz)	Larmor Frequency (MHz)	Number Acquisitions	Pulse Delay (s)	Pulse Sequence	Pulse Lengths / Delays (μs)
7.1 Meso Nb	^{17}O	Meso Nb 15N	7.05	4mm Bruker	10	40.603639	23232	3	RAPT Echo	$(1.5\text{-}98.5\text{-}1.5\text{-}98.5)_{17}$
7.1 Meso Ta	^{17}O	Meso Ta 15N	7.05	4mm Bruker	10	40.6	27008	3	RAPT Echo	-25-2-100-4-50
7.1 Meso Ti	^{17}O	Meso Ti 15N	7.05	4mm Bruker	10	40.6	26378	3	RAPT Echo	
7.1 Meso Si	^{17}O	Meso Si 15N	7.05	4mm Bruker	10	40.6	28928	3	RAPT Echo	
7.1 Amor Nb	^{17}O	Amor Nb	7.05	4mm Bruker	10	40.6	31226	3	RAPT Echo	
7.2 Meso Nb	^{15}N	Meso Nb 15N	7.05	4mm Doty	10	30.4	2024	3	CP-TPPM	1ms Swept CP
7.2 Meso Ta	^{15}N	Meso Ta 15N	7.05	4mm Doty	10	30.4	4600	3	CP-TPPM	$(5_{+15}\text{-}5_{-15})_N$
7.2 Meso Ti	^{15}N	Meso Ti 15N	7.05	4mm Doty	10	30.4	17456	3	CP-TPPM	
7.2 Meso Si, 7.3	^{15}N	Meso Si 15N	7.05	4mm Doty	10	30.4	22704	3	CP-TPPM	
7.6 A	^{17}O	Meso Nb II	8.45	4mm Bruker	10	48.8	73216	1	echo	1.5-100-3.0-25
7.6 B	^{17}O	Meso Nb II 250	8.45	4mm Varian	10	48.8	48272	1	echo	1.5-83.3-3.0-28.0
7.6 C	^{17}O	Meso Nb II 500	8.45	4mm Varian	10	48.8	13376	1	echo	1.5-83.3-3.0-28.0
7.6 D	^{17}O	Meso Nb II 750	8.45	4mm Varian	10	48.8	63536	1	echo	1.5-83.3-3.0-28.0
7.7 A	^{93}Nb	Meso Nb II	14.1	5mm Bruker Static	-	146.7	2080	3	echo	0.6-25-0.6-20
7.7 B	^{93}Nb	Meso Nb II 250	14.1	5mm Bruker Static	-	146.7	1168	3	echo	0.6-25-0.6-20
7.7 C	^{93}Nb	Meso Nb II 500	14.1	5mm Bruker Static	-	146.7	1376	3	echo	0.6-25-0.6-20
7.7 D	^{93}Nb	Meso Nb II 750	14.1	5mm Bruker Static	-	146.7	1184	3	echo	0.6-25-0.6-20
7.8 A	^{17}O	Meso Ta II	8.45	4mm Bruker	10	48.820000	83488	1	echo	1.5-100-3.0-25
7.8 B	^{17}O	Meso Ta II 250	8.45	4mm Varian	12	48.8	6192	1	echo	1.5-83.3-3.0-28
7.8 C	^{17}O	Meso Ta II 500	8.45	4mm Varian	12	48.8	8608	1	echo	1.5-83.3-3.0-28
7.8 D	^{17}O	Meso Ta II 750	8.45	4mm Varian	12	48.8	174041	1	echo	1.5-83.3-3.0-28
7.9 A	^{17}O	Meso Ti	8.45	4mm Bruker	10	48.8	81328	1	echo	1.5-100-3.0-25
7.9 B	^{17}O	Meso Ti 250	8.45	4mm Varian	12	48.8	15936	1	echo	1.5-83.3-3.0-28
7.9 C	^{17}O	Meso Ti 500	8.45	4mm Varian	12	48.8	195532	1	echo	1.5-83.3-3.0-28
7.9 D	^{17}O	Meso Ti 750	8.45	4mm Varian	12	48.8	145092	1	echo	1.5-83.3-3.0-28

Table B.5: Experimental parameters for spectra shown in chapter 7. The sample names are explained in section 3.1.5

Figure	Nucleus	Sample	Field (T)	Probe	Spinning Rate (kHz)	Larmor Frequency (MHz)	Number Acquisitions	Pulse Delay (s)	Pulse Sequence	Pulse Lengths / Delays (μs)
8.3 A, 8.8 A	^{119}Sn	Alpha $SnWO_4$	4.79	4mm Doty	12	76.138244	8516	10	1 Pulse	4
8.3 B, 8.7, 8.8 B	^{119}Sn	Beta $SnWO_4$	4.79	4mm Doty	10	76.138244	24720	10	1 Pulse	4
8.4 A	^{119}Sn	Alpha $SnWO_4$	4.8	4mm Doty	16	76.1	18335	10	1 Pulse	4
8.4 B	^{119}Sn	Alpha $SnWO_4$	4.8	4mm Doty	7.1	76.1	47762	10	1 Pulse	4
8.8 C	C887-28	4.8	4mm Doty	12	76.1	8581	10	1 Pulse	4	
8.8 D	^{119}Sn	C887-29	4.8	4mm Doty	12	76.1	7122	10	1 Pulse	4
8.8 E	^{119}Sn	C887-32B	4.8	4mm Doty	12	76.1	8064	10	1 Pulse	4
A.1 A	^{27}Al	Sodium Aluminate	14.1	3.2mm Varian	20	156.4	1432	2	1 Pulse	0.5
A.1 B	^{27}Al	Pricat 9920	14.1	3.2mm Varian	20	156.4	1672	2	1 Pulse	0.5
A.1 C	^{27}Al	Pricat 9925	14.1	3.2mm Varian	20	156.4	1864	2	1 Pulse	0.5
A.1 D	^{27}Al	Pricat 9925 R600	14.1	3.2mm Varian	20	156.4	6372	1	1 Pulse	0.5
A.1 E	^{27}Al	ZrR430	14.1	3.2mm Varian	20	156.4	63372	1	1 Pulse	0.5
A.1 F	^{27}Al	ZrR600	14.1	3.2mm Varian	20	156.4	68476	1	1 Pulse	0.5
A.1 G	^{27}Al	ZrF430	14.1	3.2mm Varian	20	156.4	16328	1	1 Pulse	0.5
A.1 H	^{27}Al	ZrF600	14.1	3.2mm Varian	20	156.4	13676	1	1 Pulse	0.5
A.1 I	^{27}Al	CeR430	14.1	3.2mm Varian	20	156.4	80136	1	1 Pulse	0.5
A.1 J	^{27}Al	CeR600	14.1	3.2mm Varian	20	156.4	77476	1	1 Pulse	0.5
A.1 K	^{27}Al	CeF430	14.1	3.2mm Varian	20	156.4	14460	1	1 Pulse	0.5
A.1 L	^{27}Al	CeF600	14.1	3.2mm Varian	20	156.4	48168	1	1 Pulse	0.5
A.2 A	^{31}P	CP325 + P Mod. Fresh	8.45	4mm Varian	12	145.8	5213	15	1 Pulse Dec.	4
A.2 B	^{31}P	CP325 + P Mod. Used	8.45	4mm Varian	12	145.8	5575	15	1 Pulse Dec.	4
A.3	^{119}Sn	RU3386-I-400	4.8	4mm Doty	12	76.1	8691	20	1 Pulse	4
A.3	^{119}Sn	RU3386-III-340	4.8	4mm Doty	12	76.1	11848	20	1 Pulse	4
A.3	^{119}Sn	RU3386-III-400	4.8	4mm Doty	12	76.1	5020	20	1 Pulse	4
A.4	^{119}Sn	RU3389-700	4.8	4mm Doty	12	76.1	18313	10	1 Pulse	4
A.4	^{119}Sn	RU3389-900	4.8	4mm Doty	12	76.1	20000	10	1 Pulse	4
A.4	^{119}Sn	RU3389-ff	4.8	4mm Doty	12	76.1	10776	10	1 Pulse	4
A.4	^{119}Sn	RU3389-9f	4.8	4mm Doty	12	76.1	14876	10	1 Pulse	4

Table B.6: Experimental parameters for spectra shown in chapter 8. The sample names are explained in sections 3.1.2, 3.1.4 and 3.1.6. 1 Pulse Dec. stands for 1 pulse decoupled.

Bibliography

[1] K.J.D.MacKenzie and M.E.Smith, *Multinuclear Solid-State NMR of Inorganic Materials* (Pergamon, Oxford, UK, 2002).

[2] D.Massiot, C.Bessada, J.P.Coutures, and F.Taulelle, Journal of Magnetic Resonance **90**, 231 (1990).

[3] H.T.Kwak, S.Prasad, T.Clark, and P.J.Grandinetti, Solid State Nuclear Magnetic Resonance **24**, 71 (2003).

[4] A.E.Bennett, C.M.Rienstra, M.Auger, and K.V.Lakshmi, Journal of Chemical Physics **103**, 6951 (1995).

[5] L.P.Cruz, J.M.Savariault, J.Rocha, J.C.Jumas, and J. D. P. de Jesus, Journal of Solid State Chemistry **156**, 349 (2001).

[6] P.D.Lao, Y. Guo, G.G.Siu, and S.C.Shen, Physical Review B **48**, 11701 (1993).

[7] K.S.Knight, Materials Research Bulletin **27**, 161 (1992).

[8] B.O.Skadtchenko, Y.Rao, T.F.Kemp, P.Bhattacharya, P.A.Thomas, M.Trudeau, M.E.Smith, and D.M.Antonelli, Angewandte Chemie International Edition **46**, 2635 (2007).

[9] W. Jeitschko and A. W. Sleight, Acta Crystallographica Section B **30**, 2088 (1974).

[10] W.Keitschko and A.W.Sleight, Acta Crystallographica **B28**, 3174 (1972).

[11] L.P.Cruz, J.M.Savariault, C.M.Morais, C.Fernandez, J. de Jesus, and J.Rocha, Journal of Solid State Chemistry **177**, 1549 (2004).

[12] L.P.Cruz, J.M.Savariault, and J.Rocha, Acta Crystallographica Section C **57**, 1001 (2001).

[13] W.G.Huckle, G.F.Swigert, and S.E.Wiberley, I&EC Product Research and Development **5**, 362 (1966).

[14] J.Carbert, Gold Bulletin **13**, 144 (1980).

[15] D.H.Everett, IUPAC, Pure and Applied Chemistry **31**, 577 (1972).

[16] C.T.Kresge, M.E.Leonowicz, W.J.Roth, J.C.Vartuli, and J.S.Beck, Letters to Nature **359**, 710 (1992).

[17] D.M.Antonelli and J.Y.Ying, Angewandte Chemie International Edition **34**, 2014 (1995).

[18] D.M.Antonelli and J.Y.Ying, Angewandte Chemie International Edition **35**, 426 (1996).

[19] L.P.Ingman, J.L.Solis, J.Vaara, and V.Lantto, Extended Abstracts of the Joint 29th AMPERE-13th ISMAR International Conference **1**, 339 (1998).

[20] M.W.Balakos and E.E.Hernandez, Catalysts Today **35**, 415 (1997).

[21] The EFSA Journal **81**, 1 (2004).

[22] R.K.Harris and B.E.Mann, *NMR and the Periodic Table* (Academic Press inc. London Ltd., , 1978).

[23] S.R.Hartmann and E.L.Hahn, Physical Review **128**, 2042 (1962).

[24] M.Potrzebowski, R.Katarzynski, and W.Ciesielski, Magnetic Resonance in Chemistry **37**, 173 (1999).

[25] M.J.Collins, C.I.Ratcliffe, and J.A.Ripmeester, Journal of Magnetic Resonance **68**, 172 (1986).

[26] R.H.P.Francisco and H.Eckert, Journal of Solid State Chemistry **112**, 270 (1994).

[27] T.Pietrass, R.Seydoux, R.E.Roth, H.Eckert, and A.Pines, Solid State Nuclear Magnetic Resonance **8**, 265 (1997).

[28] R.Dupree, W.W.Warren, and F.J.DiSalvo, Physical Review B **16**, 1001 (1977).

[29] H.Duddeck, Progress in NMR Spectroscopy **27**, 1 (1995).

[30] W.Koch, O.Lutz, and A.Nolle, Zeitschrift Fur Physik A **289**, 17 (1978).

[31] T.J.Bastow, P.J.Dirken, M.E.Smith, and H.J.Whitfield, Journal of Physical Chemistry **100**, 18539 (1996).

[32] S.Schramm, R.J.Kirkpatrick, and E.Oldfield, Journal of the American Chemical Society **105**, 2483 (1983).

[33] T.J.Bastow and S.N.Stuart, Journal of Chemical Physics **143**, 459 (1990).

[34] S.E.Ashbrook and M.E.Smith, Chemical Society Reviews **35**, 718 (2006).

[35] G.L.Turner, S.E.Chung, and E.Oldfield, Journal of Magnetic Resonance **64**, 316 (1985).

[36] L.Peng, H.Huo, Z.Gan, and C.P.Grey, Microporous and Mesoporous Materials **109**, 156 (2008).

[37] B.Julian, C.Gervais, M-N.Rager, J.Maquet, E.Cordoncillo, P.Escribano, F.Babonneau, and C.Sanchez, Chemistry of Materials **16**, 521 (2004).

[38] M.R.Hampson, S.Allen, I.J.King, C.J.Crossland, P.Hodgkinson, R.K.Harris, F.Fayon, and J.S.O.Evans, Solid State Sciences **7**, 819 (2005).

[39] O.B.Lapina, D.F.Khabibulin, K.V.Romanenko, Z.Gan, M.G.Zuev, V.N.Krasil'nikov, and V.E.Fedorov, Solid State Nuclear Magnetic Resonance **28**, 204 (2005).

[40] P.Pyykko, Molecular Physics **99**, 1617 (2001).

[41] T.Vosegaard, P.Florian, D.Massiot, and P.J.Grandinetti, Journal of Chemical Physics **114**, 4618 (2001).

[42] M.E.Smith and E.H.R.vanEck, Progress in NMR Spectroscopy **34**, 159 (1999).

[43] J.S.Clawson, K.L.Anderson, R.J.Pugmire, and D.M.Grant, Journal of Physical Chemistry **108A**, 2638 (2004).

[44] S.P.Brown, M.Perez-Torralba, D.Sanz, R.M.Claramunt, and L.Emsley, Journal of the American Chemical Society **124**, 1152 (2002).

[45] N.J.Clayden, C.Dobson, and A.Fern, Journal of Chemical Society Dalton Transcript 843 (1989).

[46] C.Cossement, J.Darville, J.M.Gilles, J.B.Nagy, C.Fernandez, and J.P.Amoureux, Magnetic Resonance in Chemistry **30**, 263 (1992).

[47] C. Mundus, G. Taillades, A. Pradel, and M. Ribes, Solid State Nuclear Magnetic Resonance **7**, 141 (1996).

[48] M.Cruz, J.Morales, J.P.Espinos, and J.Sanz, Journal of Solid State Chemistry **175**, 359 (2003).

[49] O.H.Han, H.K.C.Timken, and E.Oldfield, Journal of Chemical Physics **89**, 6046 (1988).

[50] W-S.Jung, O.H.Han, and S-A.Chae, Materials Letters **61**, 3413 (2007).

[51] A.Fratiello, D.D.Davis, S.Peak, and R.E.Schuster, Inorganic Chemistry **10**, 1627 (1971).

[52] S.Hayashi and K.Hayamizu, Journal of Chemical Physics **92**, 2818 (1989).

[53] F.Haarmann, M.Armbruster, and Y.Grin, Chemistry of Materials **19**, 1147 (2007).

[54] J.Herzfeld, D.J.Olbris, E.Furman, and V.Benderskiy, Journal of Chemical Physics **113**, 5162 (2000).

[55] M. J. Duer, *Introduction to Solid-State NMR Spectroscopy* (Blackwell Publishing, Oxford, UK, 2004).

[56] A.Abragam, in *The Principles of Nuclear Magnetism*, *The International Series of Monographs on Physics*, edited by N.F.Mott, E.C.Bullard, and D.H.Wilkinson (Oxford, Clarendon Press, 1961).

[57] C. Jager, G. Kunath, P. Losso, and G. Scheler, Solid State Nuclear Magnetic Resonance **2**, 75 (1995).

[58] A.Samoson, E.Lippmaa, and A.Pines, Molecular Physics **65**, 1013 (1988).

[59] S. E. Ashbrook and M. J. Duer, Concepts in Magnetic Resonance Part A **28A**, 183 (2006).

[60] R. Siegel, T. T. Nakashima, and R. E. Wasylishen, Concepts in Magnetic Resonance Part A **26A**, 47 (2005).

[61] Z. Yao, H. T. Kwak, D. Sakellariou, L. Emsley, and P. Grandinetti, Chemical Physics Letters **327**, 85 (2000).

[62] R.W.Martin, E.K.Paulson, and K.W.Zilm, Review of Scientific Instruments **74**, 3045 (2003).

[63] D.L.Bryce, G.M.Bernard, M.Gee, M.D.Lumsden, K.Eichele, and R.E.Wasylishen, Canadian Journal of Analytical Sciences and Spectroscopy **46**, 46 (2001).

[64] D.Freude and J.Haase, NMR Basic Principles and Progress **29**, 1 (1993).

[65] G.Engelhardt and D.Michel, *High-Resolution Solid-State NMR of Silicates and Zeolites* (John Wiley and Sons Ltd., Chichester, 1987).

[66] K. Schmidt-Rohr and H. W. Spiess, *Multidimensional Solid-State NMR and Polymers* (Academic Press Limited, 24-28 Oval Road, London, NW1 7DX, 1994).

[67] G.Metz, X.Wu, and S.O.Smith, Journal of Magnetic Resonance. Series A **110**, 219 (1994).

[68] F.Bloch, Physical Review **111**, 841 (1958).

[69] L.R.Sarles and R.M.Cotts, Physical Review **111**, 853 (1958).

[70] J.T.Cheng and P.D.Ellis, Journal of Physical Chemistry **93**, 2549 (1989).

[71] F.H.Larsen, H.J.Jakobsen, P.D.Ellis, and N.C.Nielsen, Journal Of Magnetic Resonance **131**, 144 (1998).

[72] T. F. Kemp, Master's thesis, University of Warwick, Coventry, CV4 7AL, England, 2004.

[73] M.Bak, T.Rasmussen, and N.C.Nielsen, Journal of Magnetic Resonance **147**, 296 (2000).

[74] M.Eden, Concepts in Magnetic Resonance Part A **17A**, 117 (2003).

[75] M.Eden, Concepts in Magnetic Resonance Part A **18A**, 24 (2003).

[76] J.Hexem, M.Frey, and S.Opella, Journal of Chemical Physics **77**, 3847 (1982).

[77] D.W.Alderman, M. S. Solum, and D. M. Grant, Journal of Chemical Physics **84**, 3717 (1986).

[78] G.L.Hoatson, D.H.Zhou, F.Fayon, D.Massiot, and R.L.Vold, Physical Review B **66**, (2002).

[79] G.Czjzek, J.Fink, F.Gotz, and H.Schmidt, Physical Review B **23**, 2513 (1981).

[80] G.Czjzek, Physical Review B **25**, 4908 (1982).

[81] G.E.Jellison, L.W.Panek, P.J.Bray, and G.B.Rouse, Journal of Chemical Physics **66**, 802 (1977).

[82] D.Holland, S.A.Feller, T.F.Kemp, M.E.Smith, A.P.Howes, D.Winslow, and M.Kodama, Physics and Chemistry of Glasses: European Journal of Glass Science and Technology **48B**, 1 (2007).

[83] P.J.Chu and B.C.Gerstein, Journal of Chemical Physics **91**, 2081 (1989).

[84] M. H. Cohen, J. P. Jan, C. C. Klick, W. Kohn, G. F. Koster, F. Reif, and J. H. Schulman, in *Solid State Physics Advances in Research and Applications*, Vol. 5 of *Solid State Physics*, edited by F. Seitz and D. Turnbull (Academic Press inc. New York, , 1957).

[85] J. G. E. Jellison, S. A. Feller, and P. J. Bray, Journal of Magnetic Resonance **27**, 121 (1977).

[86] J. Herzfeld and A. E. Berger, Journal of Chemical Physics **73**, 6021 (1980).

[87] C.J.Jameson, Solid State Nuclear Magnetic Resonance **11**, 265 (1998).

[88] K.Eichele, Private Communication.

[89] H.Hahn, G.Frank, W.Klingler, A.D.Meyer, and G.Stoerger, Zeitschrift fuer Anorganische und Allgemeine Chemie **271**, 153 (1953).

[90] E.R.Andrew, J.L.Carolan, and P.J.Randall, Physics Letters **35A**, 435 (1971).

[91] X.Hu, B.O.Skadtchenko, M.Trudeau, and D.M.Antonelli, Journal of the American Chemical Society **128**, 11740 (2006).

[92] B.Julian, C.Gervais, E.Cordoncillo, P.Escribano, F.Babonneau, and C.Sanchez, Chemistry of Materials **15**, 3026 (2003).

[93] B.Julian, C.Gervais, M-N.Rager, J.Maquet, E.Cordoncillo, P.Escribano, F.Babonneau, and C.Sanchez, Chemistry of Materials **16**, 521 (2004).

[94] D.M.Pickup, G.Mountjoy, M.A.Holland, G.W.Wallidge, R.J.Newport, and M.E.Smith, Journal of Materials Chemistry **10**, 1887 (2000).

[95] T.J.Bastow, A.F.Moodie, M.E.Smith, and H.J.Whitfield, Journal of Materials Chemistry **3**, 697 (1993).

[96] T.J.Bastow, G.Doran, and H.J.Whitfield, Chemistry of Materials **12**, 436 (2000).

[97] E.Oldfield, C.Coretsopoulos, S.Yang, L.Reven, H.C.Lee, J.Shore, O.H.Han, and E.Ramli, Physical Review B **40**, 6832 (1989).

[98] T.N.Pham, J.M.Griffin, S.Masiero, S.Lena, G.Gottarelli, P.Hodgkinson, C.Filip, and S.P.Brown, Physical Chemistry Chemical Physics **9**, 3416 (2007).

[99] H.Yoshitake, T.Sugihara, and T.Tatsumi, Chemistry of Materials **14**, 1023 (2002).

[100] M.Mamak, N.Coombs, and G.Ozin, Journal of the American Chemical Society **122**, 8932 (2000).

[101] K.O.Drake, D.Carta, L.J.Skipper, F.E.Sowrey, R.J.Newport, and M.E.Smith, Solid State Nuclear Magnetic Resonance **27**, 26 (2005).

[102] A.Flambard, L.Montagne, L.Delevoye, and S.Steuernagel, Solid State Nuclear Magnetic Resonance **32**, 34 (2007).

[103] C.Gervais, F.Babonneau, and M.E.Smith, Journal of Physical Chemistry **105B**, 1971 (2001).

[104] S.Brunauer, P.H.Emmett, and E.Teller, Journal of the American Chemical Society **60**, 309 (1938).

[105] L.Duma, W.C.Lai, M.Carravetta, L.Emsley, S.P.Brown, and M.H.Levitt, ChemPhysChem **5**, 815 (2004).

[106] P.C.Riedi, Physical Review B **15**, 5197 (1977).